The Planetary Science Journal, 6:299 (34pp), 2025 December https://doi.org/10.3847/PSJ/ae1968

The Geology of a Small Main-belt S-class Binary Asteroid System: Dinkinesh and Its Contact Binary Satellite Selam as Observed by the Lucy Mission

E. B. Bierhaus[1], S. Marchi[2], S. J. Robbins[2], S. Mottola[3], W. F. Bottke[2], K. Noll[4], J. F. Bell III[5], J. M. Sunshine[6], J. Spencer[2], D. Britt[7], H. Levison[2], F. Preusker[3], C. Howett[8,9], and M. Hirabayshi[10]
[1] Lockheed Martin Space, Littleton, CO, USA; edward.b.bierhaus@lmco.com
[2] Southwest Research Institute, Boulder, CO, USA
[3] Deutsches Zentrum für Luft- und Raumfahrt, Cologne, Germany
[4] NASA Goddard Spaceflight Center, Greenbelt, MD, USA
[5] Arizona State University, Tempe, AZ, USA
[6] University of Maryland, College Park, MD, USA
[7] University of Central Florida, Orlando, FL, USA
[8] University of Oxford, Oxford, UK
[9] Planetary Science Institute, Tucson, AZ, USA
[10] Georgia Institute of Technology, Atlanta, GA, USA
Received 2025 April 22; revised 2025 September 26; accepted 2025 October 22; published 2025 December 22

Abstract

The Lucy spacecraft flew past the ∼738 m diameter, S-class main-belt asteroid (152830) Dinkinesh on 2023 November 1, revealing a satellite named Selam. We used images acquired during the flyby to evaluate surface features on both Dinkinesh and Selam. We find a shallow crater size–frequency distribution (SFD) for Dinkinesh, consistent with crater SFDs observed on other subkilometer asteroids. We derive crater depth-to-diameter ratios near 0.1, also consistent with typical values seen on other asteroids. We calculate a cumulative boulder SFD for Dinkinesh with power-law index 3.93 ± 0.15 slightly steeper though in the range of other S-class asteroids. We find growing evidence that boulder SFDs are, on average, steeper for S-class than C-complex asteroids. Two major surface features on Dinkinesh, Sumak Fossa (a large trough) and Fab Dorsum (an equatorial ridge), are likely an outcome of YORP spinning up Dinkinesh fast enough to produce failure. A self-consistent structure for Dinkinesh that complies with the global shape, feature morphologies, and the estimated 10–20 Myr YORP spin-up timescale is a rubble-pile object with a nearly strengthless surface and an interior strength that is less than tens of Pa. Selam could have formed via YORP-driven mass shedding from Dinkinesh, though other formation mechanisms are possible. Combining a low-strength surface with the crater population and an impact model, we estimate a ∼1 Myr surface age for Dinkinesh. The presence of mass wasting and young troughs indicates that stress accumulation and release continue on Dinkinesh to the present day.

Unified Astronomy Thesaurus concepts: Asteroids (72); Planetary geology (2288); Craters (2282)

1. Introduction

NASA's Lucy mission launched on 2021 October 16 and currently is en route to encounter multiple objects in the Jupiter Trojan population (H. Levison et al. 2021). The spacecraft trajectory from Earth to the Trojan asteroids (C. Olkin et al. 2024) involves passage through the main asteroid belt, and the trajectory includes flyby targets to test mission capabilities that will be used for the Trojan encounters. In addition, the practice flybys offer an opportunity to evaluate instrument performance on a small irregular body, i.e., objects consistent with the main Lucy science targets, complementing instrument calibrations conducted using observations of Earth's Moon (an approximately spherical body) during the first Earth-gravity assist on 2022 October 16 (S. J. Robbins et al. 2023; J. R. Spencer et al. 2024).

After launch, the mission added the S-class main-belt asteroid (MBA) (152830) Dinkinesh to the encounter list (H. F. Levison et al. 2024) to evaluate the tracking system (P. G. Good et al. 2022). The Dinkinesh encounter phase-angle profile was similar to that of the Trojan encounters, and targeting the body required only a small amount of propellant. On 2023 November 1, the Lucy spacecraft flew by Dinkinesh at 4.5 km s^{-1} and a closest-approach distance of 430.6 km (H. F. Levison et al. 2024). Images from the encounter revealed that Dinkinesh has a satellite, subsequently named Selam, which itself is a contact binary, the first resolved observations of such a body (H. F. Levison et al. 2024).

Multiple asteroids have been visited by spacecraft, both MBAs and near-Earth asteroids (NEAs), and across a variety of size scales (Table 1). To date the sub-1 km NEAs seen by spacecraft all appear to be rubble piles (Itokawa, H. Miyamoto et al. 2007; Bennu, O. S. Barnouin et al. 2019; Ryugu, S. Watanabe et al. 2019; Didymos and Dimorphos, O. S. Barnouin et al. 2024), i.e., they are composed of numerous smaller objects held together by self-gravity. The Dinkinesh–Selam system is the first spacecraft encounter with a subkilometer MBA and thus offers the first opportunity to compare similarly sized bodies in the NEA and MBA populations. Asteroid body shape and surface morphology are expressions of structure and strength, and ultimately of the histories of these objects. Spectrally, Dinkinesh is consistent with S-type asteroids (B. T. Bolin et al. 2023) and thus should be compositionally most similar to (in decreasing size scale) Ida, Gaspra, Eros, Annefrank, Toutatis, Didymos, and Itokawa. In addition, two S-type satellites have been observed by spacecraft: Dactyl, a

Table 1
Asteroids Visited by Spacecraft as of the Publication of This Paper

Asteroid	NEA or MBA	Mission	Spectral Class	Dimensions	References
(25143) Itokawa	NEA	Hayabusa	S	535 × 294 × 209 m	A. Fujiwara et al. (2006)
(162173) Ryugu	NEA	Hayabusa2	C	∼900 m diameter	T. Yuichi et al. (2020)
(101955) Bennu	NEA	OSIRIS-REx	B	504 × 492 × 456 m diameter	M. G. Daly et al. (2020)
(433) Eros	NEA	NEAR	S	∼34 × 11 × 11 km	J. Veverka et al. (2000)
(4179) Toutatis	NEA	Chang'e 2	S	4.3 × 2.0 × 1.7 km	R. S. Hudson et al. (2003); J. Huang et al. (2013)
(65803) Didymos	NEA	DART	S	∼851 × 849 × 620 m	S. P. Naidu et al. (2020); O. S. Barnouin et al. (2024)
Dimorphos	NEA	DART	S	177 × 174 × 116 m	Moon of Didymos; O. S. Barnouin et al. (2024)
(243) Ida	MBA	Galileo	S	60 × 25 × 19 km	M. J. S. Belton et al. (1996)
Dactyl	MBA	Galileo	S	∼1.2 × 1.4 × 1.6 km	Moon of Ida; J. Veverka et al. (1996)
(951) Gaspra	MBA	Galileo	S	18 × 11 × 9 km	M. J. S. Belton et al. (1992)
(253) Mathilde	MBA	NEAR	C	66 × 48 × 46 km	J. Veverka et al. (1999)
(2867) Steins	MBA	Rosetta	E	5.9 × 4 km	L. Jorda et al. 2012.
(5535) Annefrank	MBA	Stardust	S	6.6 × 5.0 × 3.4 km	T. C. Duxbury et al. (2004)
(21) Lutetia	MBA	Rosetta	M	121 × 1010 × 75 km	H. Sierks et al. (2011)
(152830) Dinkinesh	MBA	Lucy	S	∼738 m diameter	This paper and H. F. Levison et al. (2024)
Selam	MBA	Lucy	S	240 × 200 × 200 m 280 × 220 × 210 m	H. F. Levison et al. (2024)

satellite of Ida (J. Veverka et al. 1996), and Dimorphos, a satellite of Didymos (S. P. Naidu et al. 2020; R. T. Daly et al. 2023). Though still a relatively small set, these objects provide valuable context in which to evaluate Dinkinesh and Selam. Collectively, the ensemble of these objects provides an increasingly expansive catalog to assess effects of physical size and collisional, thermal, and radiation environments on asteroids. These bodies span over two orders of magnitude in size, two different collisional environments (MBA vs. NEA), potentially different interior structures, and single versus binary objects. The existence of a binary system in which the satellite itself is a contact binary (two volumes that contact each other at a location with a small cross-sectional area) motivates a search for morphological characteristics that can inform the formation and evolution of such a system.

There is increasing appreciation that the evolution of asteroids has a complexity that belies the small number of external forces acting on these objects. For example, even though the surface acceleration of all asteroids is tiny compared with terrestrial planets (of order $<0.001G$ for asteroids <100 km, where $G = 9.8\ \mathrm{m\ s^{-2}}$ surface acceleration on Earth), the surface gravity variation between, e.g., a 10 km asteroid and a 500 m diameter asteroid is almost four orders of magnitude. This difference results in significant variation in the balance of gravity, rotation, and cohesion at the surface, with potential consequences for surface properties and regolith evolution (e.g., D. J. Scheeres et al. 2010; E. B. Bierhaus et al. 2023). The superposition of the Yarkovsky effect (an asymmetric absorption and reradiation of solar energy that creates a small thrust, slowly changing the object's orbital semimajor axis) and YORP effect (torques on the rotation axis, caused by an irregular shape and/or surface topography, which can change the rotation state; e.g., D. P. Rubincam 2000) can create a feedback loop between an object's orbit and rotation state (see, e.g., reviews in W. F. Bottke et al. 2006; D. Vokrouhlický et al. 2015). Given that orbital parameters (semimajor axis, eccentricity, and inclination) determine the collisional environment, there is an additional feedback loop with impacts potentially changing the rotation state and shape of the body, thereby in turn modifying the magnitude and direction of the YORP torques.

Here we provide the observed crater and boulder populations, describe and quantify major surface features on both Dinkinesh and Selam, and provide an assessment of the YORP spin-up of Dinkinesh. Collectively these enable us to derive a history of the system that spans the estimated age of the observed surface. In addition, we introduce International Astronomical Union (IAU)−approved names for several prominent features observed in the Lucy data.

2. Datasets

Most of the information on Dinkinesh's geology comes from the Lucy Long-Range Reconnaissance Imager (L'LORRI; H. A. Weaver et al. 2023). L'LORRI is the highest-resolution imager on the Lucy spacecraft, with a pixel scale of $4.93\ \mu\mathrm{rad\ pixel^{-1}}$. Because the Dinkinesh encounter was not a formal mission science campaign, the imaging sequence used for the encounter was a subset of planned observations for the Trojan encounters, optimized to support the engineering priorities of the encounter. Nonetheless, the planned sequence and successful flyby generated hundreds of scientifically useful images and enabled the development of a shape model.

2.1. Imaging Data

From 10 minutes before close approach until 9 minutes afterward, L'LORRI took alternating 2 ms, 10 ms, and 100 ms images every 15 s. The 2 ms images were exposed for the sunlit surface at low phase angles (α), though some saturation occurred in the lowest-phase images ($\alpha < 5°$). The longer exposures were taken primarily for characterization of image stability, and many were saturated as expected, though the 10 ms images were well exposed at higher phase angles (Figure 1). Additional images were taken at a less frequent cadence outside the ±10-minute period. For all images in this paper we orient Dinkinesh with spin north approximately up, i.e., when we use north, we mean spin north. Because Dinkinesh is a retrograde rotator with relatively low orbital inclination ($2\overset{\circ}{.}09$), the spin north direction is approximately toward ecliptic south.

The resulting collection of L'LORRI images span a range of pixel scale and phase-angle combinations (Figure 2). Because

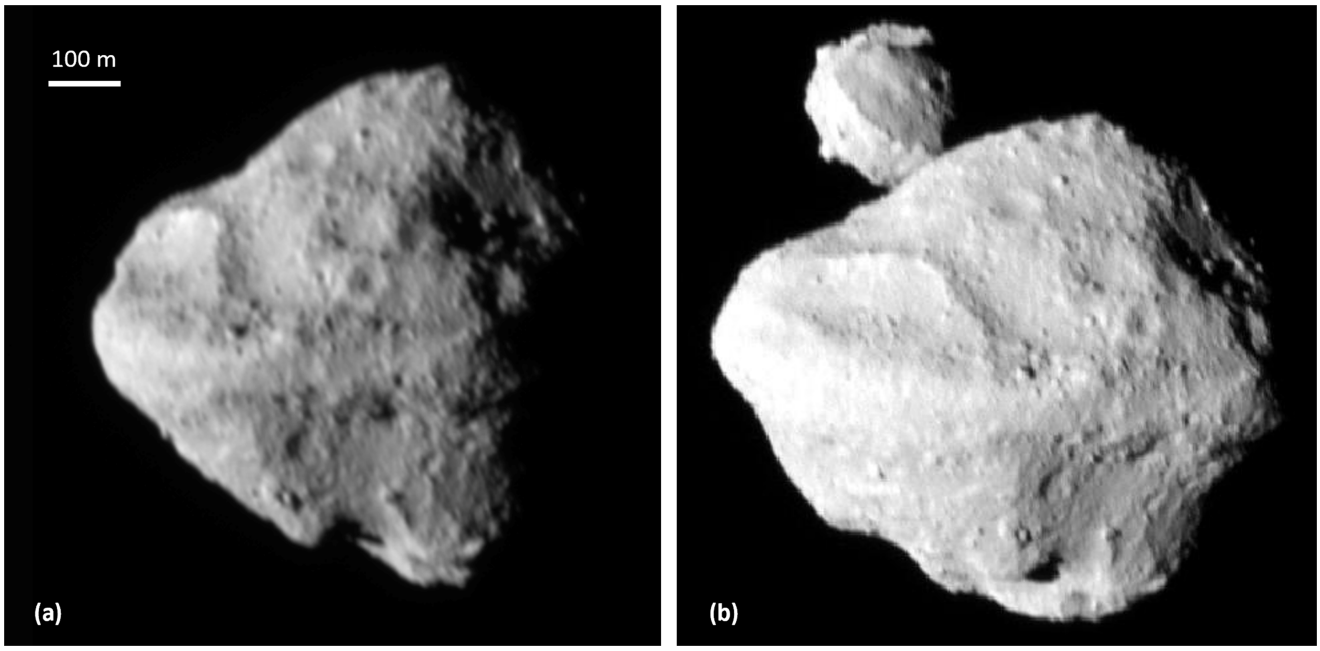

Figure 1. Representative L'LORRI images of Dinkinesh and Selam. North is approximately up in both images. (a) L'LORRI image lor_0752129545_03599, taken 1.2 minutes before closest approach. Range is 528 km, pixel scale is 2.6 m pixel^{-1}, and phase is 66°. The scale bar indicates approximately 100 m. (b) L'LORRI image lor_0752129617_03613, taken within a few seconds of closest approach. Range is 425 km, pixel scale is 2.1 m pixel^{-1}, and phase is 29°. Dinkinesh is in the foreground, and Selam is in the background. The view of Selam is nearly parallel to the long axis of the bilobed body, meaning that Selam's Dinkinesh-facing lobe almost entirely obscures the anti-Dinkinesh lobe.

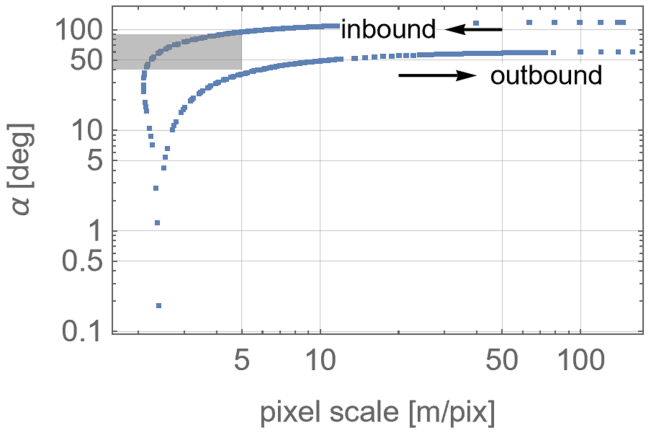

Figure 2. The phase angle α vs. pixel scale for L'LORRI images acquired from −1.83 hr through +1.99 hr relative to closest approach. Data are derived from the predicted trajectory. Arrows indicate the direction of the spacecraft relative to closest approach. The light-gray box identifies the parameter space for pixel scale $\leqslant$5 m pixel^{-1}, and $40° \leqslant \alpha \leqslant 90°$, which is the preferred range for making measurements of surface features.

the incidence and emission angles depend on the body shape, which we do not know in detail a priori for the Lucy targets (including Dinkinesh), we established observing criteria based on the phase angle and pixel scale, which we can estimate a priori. Our preferred phase-angle range for surface geomorphology is $40° \leqslant \alpha \leqslant 90°$, which provides shadowing that enables measurement and assessment of surface topography. The approach asymptote to Dinkinesh resulted in a closest approach with α near 0°; thus, the highest-resolution images have low phase and little shadowing, placing them outside our preferred α values for geomorphology. However, low-phase images improve the sensitivity to albedo variations (e.g., M. K. Shepard 2017) and so are important for deriving photometric properties (S. Mottola et al. 2024). The "best" images for identifying, measuring, and characterizing surface features—based on shadowing (i.e., higher α) and relatively high resolution—dominantly occur during the inbound trajectory (Figure 2).

2.2. Digital Shape Model

The L'LORRI imaging data provide the basis for the generation of a digital shape model of Dinkinesh. Such a shape model is the prerequisite for a quantitative geological interpretation of the body. H. F. Levison et al. (2024) reported the first version of the shape model of Dinkinesh, based entirely on stereophotogrammetry. This technique leverages the measurement of homologue surface points (control points) observed under different viewing geometries, to triangulate their position in space while simultaneously solving for the shape, spacecraft trajectory, and rotation state of the object. In H. F. Levison et al. (2024), the side of the body not covered by stereo images, which corresponded to about 55% of the total surface, was modeled by using an analytical solid figure (a rotationally symmetric superellipsoid; B. Ni et al. 2016) that best fit the visible hemisphere of the body. For the geologic analysis presented in this paper, we used a newer version of the Dinkinesh shape model (Figure 3), which improves on several aspects of the model presented in H. F. Levison et al. (2024). A full description of the Dinkinesh shape model will be presented in F. Preusker et al. (2026, in preparation); see F. Preusker et al. (2024) for a description of the Lucy mission process for shape model development. In addition to stereo imaging, the new model makes use of limb profiles, thereby extending its coverage to the whole illuminated hemisphere. Furthermore, the new model refines the description of the unseen hemisphere by applying additional physical constraints. In particular, the original superellipsoidal shape was iteratively modified by applying smooth, low-order

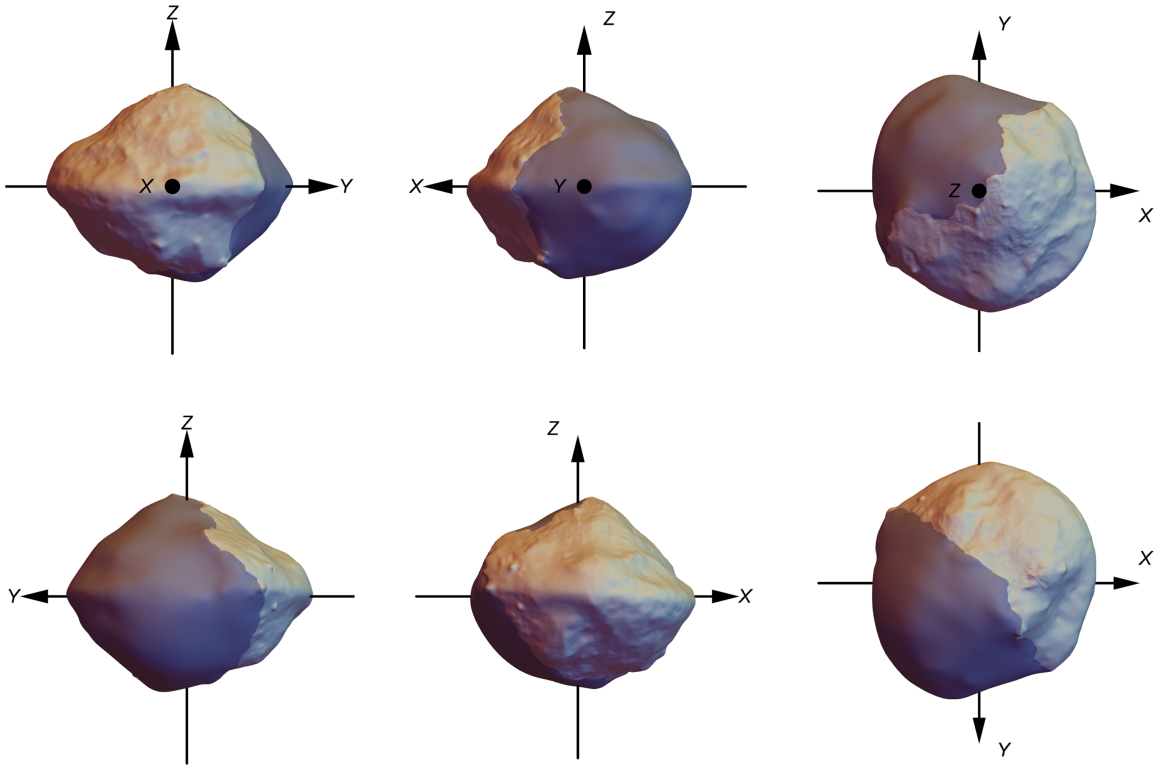

Figure 3. The Dinkinesh shape model used in this paper. The lighter-gray region is the shape derived from Lucy images when the object was resolved, and the darker shade is the shape derived from other techniques (see text). The top row, from left to right, shows views from the $+x$-, $+y$-, and $+z$-directions. The bottom row, from left to right, shows views from the $-x$-, $-y$-, and $-z$-directions.

perturbations aiming to minimize (1) the tilt of the principal axis of inertia (computed by assuming a constant mass density) with respect to the spin axis, (2) the distance of the center of mass with respect to the origin, and (3) the deviation of the synthetic photometric light curves generated with the model, with respect to the ones observed by L'LORRI during the departure phase (H. F. Levison et al. 2024). For the resolved surfaces seen by Lucy, the shape model has a ground sample distance of 2.1 m pixel^{-1}. The radial errors are the average of the stereo ray-intersection errors for all the points in the original point cloud that fall within each facet. The median of these errors is 1.7 m, with smaller or larger errors depending on the pixel scale and available emission angles of images that overlap a given facet. We include the per-facet error in all the profiles used for our analysis, reflected in figures of profiles extracted from the shape model.

The maximum body dimensions are 910 × 870 × 716 m, and the diameter of a volume-equivalent sphere is 738 m. The resulting new shape model has a volume of $(2.1 \pm 0.2) \times 10^8$ m^3, slightly larger than the one for the model in H. F. Levison et al. (2024), but still within the quoted uncertainties. The revised system bulk density is, accordingly, $(2.22 \pm 0.35) \times 10^3$ kg m^{-3}.

3. Crater Populations and Surface Ages

Impact craters (hereafter simply "craters") are a common surface feature on asteroids. Crater abundances are correlated with surface age, while crater morphology is in part related to target properties. Here we focus on measuring the crater population and using those data to derive a surface age. In addition, we limit our morphological assessment to the depth-to-diameter ratio for the largest craters because the shape model resolutions do not support such measurements for smaller sizes.

Table 2
L'LORRI Images Used for Phase 1 Crater Measurements

L'LORRI Image	Pixel Scale (m pixel^{-1})	Resolution (m) (3× pixel scale)	Phase Angle (deg)
lor_0752129590_03608	2.2	6.6	45
lor_0752129617_03613	2.1	6.3	33

Note. The values listed are from the predicted trajectory.

3.1. Description of Measurement and Crater SFDs

Our measurements of craters on Dinkinesh occurred in two phases. The first phase occurred shortly after the 2023 November 1 flyby, when the image data first were available on Earth. We used unprojected L'LORRI Level 1 calibrated images (H. A. Weaver et al. 2023). Two authors (E.B.B. and S. J.R.) made measurements on two images (Table 2) near closest approach—which thus provided some of the highest-resolution views—yet with large enough phase angles that surface shadowing aided the identification of craters (Figure 2). The 33° phase angle for one image is less than our nominal 40° minimum, a compromise for this engineering-focused encounter. Although these images provided the best available combination of resolution and phase angle, the measurements were aided by examining images throughout the flyby to evaluate the appearance of a feature from multiple viewing angles. S. J. Robbins et al. (2025) found a weak dependence on

crater detection as a function of emission angle and a stronger dependence as a function of incidence angle (detection increasing as incidence angle increases). In the case of the Lucy flyby, the encounter geometry resulted in some limitations to control both emission and incidence angles to preferred values for measuring craters. However, the approximately spherical shape of Dinkinesh and the nearly equatorial flyby mean that (1) most of the surface was observed at low emission angle (most of the surface area of a sphere occurs in low and mid-latitudes, corresponding to low to medium emission angles) and (2) the only area observed exclusively at low incidence angle is the region containing the subsolar point. We expect that there are observational biases that reduced our ability to detect craters, which we address when discussing the derived size–frequency distribution (SFD).

The second phase of measurement occurred several months later when the shape model (Section 2.2) was available, with co-registered images projected onto the shape model. One researcher (S.R.J.) repeated the crater measurement task using the Dinkinesh shape model in the Small Body Mapping Tool (SBMT; see C. M. Ernst et al. 2018) superimposed with images from the flyby.

In both phases each researcher assigned a confidence category to a feature, where 1 represented the highest confidence that the feature is a crater and 3 represented the lowest confidence. For the crater population reported here we merged the measurements as follows:

1. Merged category 1 craters = craters that both researchers identified as category 1 in their individual measurements.
2. Merged category 2 craters = craters that only one researcher identified as a category 1 crater in their individual measurements.
3. Merged category 3 craters = craters that an individual researcher identified as category 2.

All category 3 craters from individual measurements were removed from the merged dataset. The resulting merged dataset has 9 category 1 craters, 10 category 2 craters, and 10 category 3 craters (Figures 4(a)–(f)).

We used SBMT to measure a surface area needed to calculate the crater SFDs (Figure 4). The corresponding surface area over which we measured the crater population is 0.71 km^2. We fit a power law to the differential form of the data, $dN = kD^{-b}$, where dN is the number of craters between diameters D and $D + dD$, normalized by the measurement area A and the diameter range dD, and k and b are constants derived from an empirical fit. The resulting SFD for the entire dataset (categories 1–3) is shallow (Figure 4(b)), with $k = 1.54 \pm 1.98$ and $b = 1.66 \pm 0.39$. The error bar on k implies the possibility of negative values, which is clearly nonphysical. The nonlinear fit is purely a numerical routine and is not constrained by the physical reality to keep $k > 0$. The physical interpretation of this error bar is that the fit cannot constrain the minimum nonzero value of k. The power-law fit to the cumulative form of the data, $N = cD^{-a}$, where N is the number of craters with diameter D and larger and c and a are constants derived from the fit, results in $c = 0.60 \pm 0.11$ and $a = 1.09 \pm 0.05$.

If we restrict our measurements to the craters with the highest confidence (category 1), the binned, differential version of the data has only three points (Figure 4(b)). The smallest-diameter data point has a lower differential value than the next largest bin, which typically is symptomatic of the finite resolution of the images causing incomplete identification of smaller crater sizes; this crater spatial density decrease due to finite resolution commonly is called the "completeness limit." S. J. Robbins et al. (2014) found that, at least for LROC images of the Moon, the completeness limit is close to 10 resolution elements. The peak crater spatial density occurs at ~60 m diameter (bin diameter range spans from 52 to 73 m), which is roughly 10 times the resolution (not pixel scale) of the images (Table 2). Alternatively, real reductions in small-crater spatial densities were observed on Bennu (E. B. Bierhaus et al. 2023), and our Dinkinesh boulder measurements (Section 4) show a peak spatial density at smaller diameter. In any case, with only two data points we cannot provide a robust SFD fit to the differential form of the data. The fit to the cumulative form of the category 1 data, for diameters $\geqslant$60 m, results in $c = 0.10 \pm 0.05$ and $a = 1.60 \pm 0.17$.

Because Selam does not have a shape model, our measurements utilized an unprojected L'LORRI image lor_0752129590_03608 (one of the two in Table 2; Figure 4(g)). As with Dinkinesh, our merged category 1 measurements include only the craters identified by both researchers. The merged dataset includes three category 1 craters and no category 2 or 3 craters. We do not report a crater SFD fit for Selam because three craters are insufficient for a meaningful fit.

3.2. Crater-based Surface-age Estimates

The observed crater SFDs enable us to estimate the crater-retention ages of Dinkinesh and Selam. For this, we derive a crater-model production function for Dinkinesh and Selam that estimates the expected crater SFD per unit time (S. Marchi et al. 2009). This is obtained by coupling an impactor SFD to a crater scaling law. We use the impactor SFD derived from main-belt collisional models from W. F. Bottke et al. (2020) and the approach by D. R. Davis & P. Farinella (1997) to compute an intrinsic collisional probability of 2.6×10^{-18} km^{-2}. The crater scaling law is from K. A. Holsapple & K. R. Housen (2007), and here we select the general scaling law formulation for cohesive soils (see S. Marchi et al. 2015 for more detailed information about the methods). We do not consider impact armoring (e.g., E. Tatsumi & S. Sugita 2018; E. B. Bierhaus et al. 2022)—a process that can reduce crater size, or even prevent craters from forming—because the observed crater and boulder SFDs are insufficient to derive a data-informed model for crater production on Dinkinesh. However, armoring may play a role in the crater SFD (Section 7.1).

The crater scaling law we used depends on, among other things, a target strength value to convert an impactor diameter to a crater diameter: the greater the strength, the smaller the resulting crater. We do not have direct measurements of a strength for Dinkinesh or Selam, though we do have indirect evidence (see subsequent discussion) for relatively low strength. The other small, S-class asteroids observed by spacecraft—Itokawa, Didymos, and Dimorphos—all appear to be rubble piles and weakly bound bodies. Even the larger S-class asteroid Eros may have an interior consistent with a rubble-pile asteroid (R. L. Ballouz et al. 2025). O. S. Barnouin et al. (2024) use a maximum strength of 10^5 Pa in their assessment of surface ages derived from the crater populations on Didymos and Dimorphos, which we adopt here as a

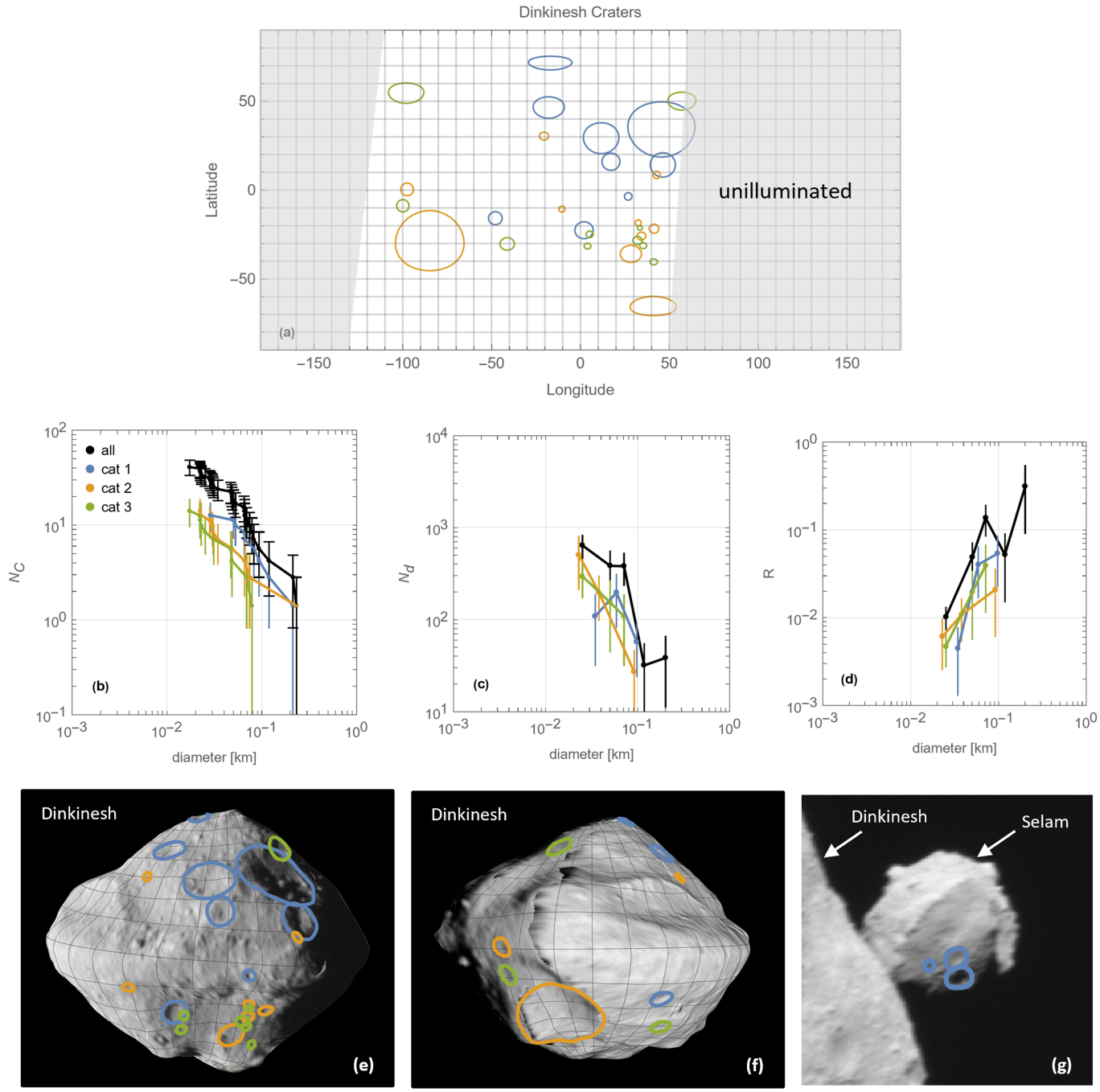

Figure 4. The measured Dinkinesh crater population. (a) The spatial distribution of the craters, colorized by category (see label in panel (b)). The light-gray regions are approximately the unilluminated surfaces not seen during the flyby. The actual dawn and dusk terminators are irregular owing to surface topography and span a range of ∼10°–15° longitude, depending on latitude. Panels (b), (c), and (d) are the cumulative, differential, and relative versions of the crater SFD, respectively. Error bars are Poisson sqrt-N. The black data are for all data, and the individual colors correspond to each category as noted by the figure legend in panel (b). Panels (e) and (f) are the Dinkinesh category 1–3 craters on the approach and departure hemispheres, respectively (compare with panel (a)), and rendered on the shape model. The two LORRI images used for these panels are lor_0752129617_03613 and lor_0752129707_03631. (g) The three category 1 craters on Selam, LORRI image lor_0752129590_03608.

maximum strength value. The minimum bounding case is the "gravity regime," when gravity (rather than target strength) halts the growth of a crater. The gravity regime provides the largest-diameter crater for a given-sized impactor.

With multiple strength values and different populations of craters (Section 3.1), there are many possible outcomes for the derived surface age. We simplify the results by considering two end-member scenarios that provide the oldest and youngest ages. The oldest surface age results from combining the maximum number of craters and highest surface strength, which corresponds to all category 1–3 craters and 10^5 Pa strength. The youngest surface age results from the minimum number of craters and zero strength, which corresponds to only category 1 craters and gravity scaling. In conjunction with these parameters, we use a target density of 2.2 g cm^{-3}; an average diameter of 0.74 and 0.21 km for Dinkinesh and Selam, respectively (H. F. Levison et al. 2024), and an average impactor density of 2.6 g cm^{-3}.

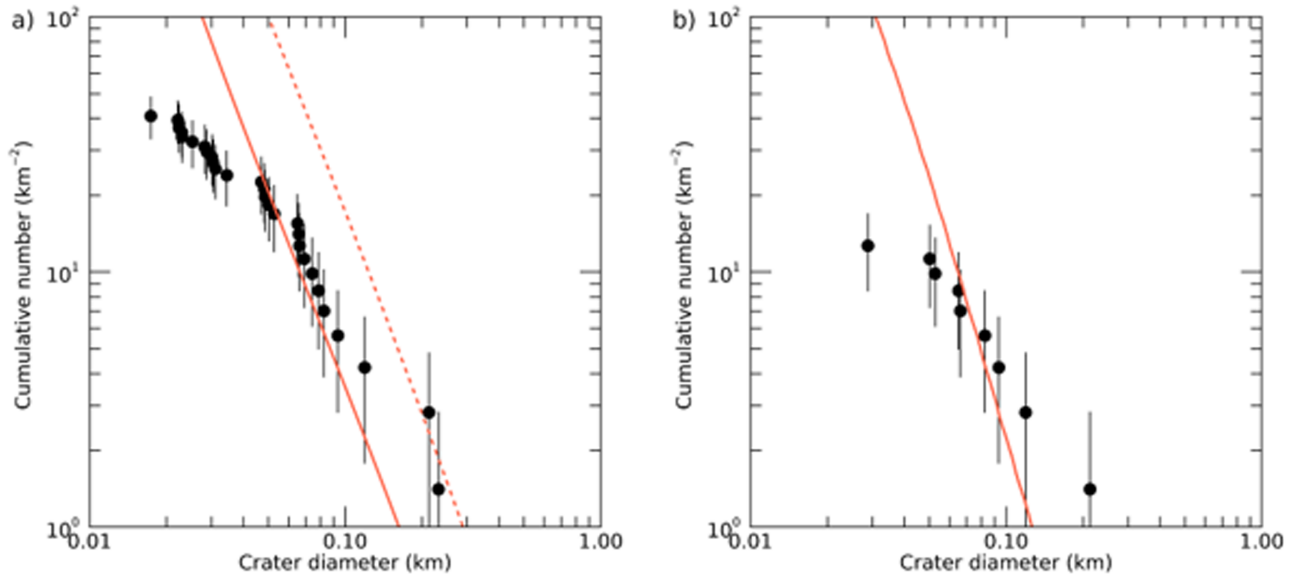

Figure 5. The cumulative crater SFD for (a) all Dinkinesh craters and (b) only category 1 craters, with best-fit production functions that provide model crater ages (red lines). In panel (a), the solid red line is a fit to all craters >45 m diameter, and the dashed red line is a fit to all craters >110 m diameter. In panel (b), the red line is a fit to all craters ⩾60 m diameter.

We start with the oldest age obtained by using a high strength value (10^5 Pa) and all crater confidence levels (Figure 5(a)). The slope of the cumulative SFD is inconsistent over the observed diameter range, with a steeper slope implied by the very largest craters and a shallower slope by smaller craters. We therefore provide two fits to these data: one for craters larger than 45 m, and a second for craters larger than 110 m. The resulting model crater-retention ages are ∼130 and ∼650 Ma, respectively (Figure 5(a)). In contrast, the category 1 craters do not show obvious variations across the (limited) SFD (Figure 5(b)), and thus we calculated a single gravity scaling fit for all craters larger than 45 m. The corresponding age is ∼0.9 Ma. Varying the strength value between the maximum and gravity scaling used here, and/or using different combinations of the crater categories, will result in ages in between 0.9 and 650 Ma. For example, the resulting ages for the category 1 craters in Figure 5(b) are ∼1 Ma for $Y = 10$ Pa and ∼10 Ma for $Y = 10^3$ Pa.

We performed a similar calculation for the craters observed on Selam (Figure 6), using the gravity regime, obtaining a nominal model age of ∼0.16 Ma. Though nominally younger than Dinkinesh, there are so few craters that small number statistics render this value indistinguishable from Dinkinesh.

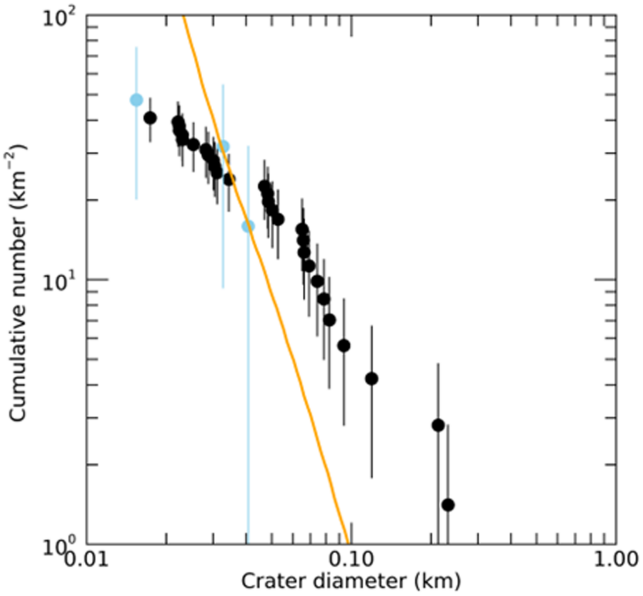

Figure 6. All Dinkinesh craters (black points) with the Selam craters (light-blue points) and the best-fit production function to the Selam data.

3.3. Crater Depth-to-diameter (d/D) Ratios

Two of the category 1 craters reside on the approach terminator (Figure 4), and several others are seen only at high emission angle or at lower resolution. However, three category 1 craters are at mid- or low latitude and visible in the highest-resolution approach images. We made depth-to-diameter measurements of those three craters (Figure 7). We used SBMT to identify the start and end for each profile and then extracted geometric heights and radial errors along each profile. We calculated crater depths by first averaging opposing rim heights on a profile and then finding the distance between the deepest point of the profile and the average rim height. The error on the d/D ratio uses (i) the propagation of errors on the depth measurement (averaging the rim heights and the corresponding height difference with the profile minimum), (ii) an estimated two-facet error on each of the two locations on opposing rims used to define the diameter, and (iii) the propagation of errors on the d/D ratio.

The craters are ∼67, 82, and 134 m (Figures 7(a)–(c)) in diameter, with nominal d/D values of 0.08 ± 0.02, 0.09 ± 0.02, and 0.10 ± 0.01, respectively (Figure 7(d)). All values, including error bars, are less than 0.12. The average d/D for craters on Eros is 0.13 ± 0.03 (M. S. Robinson et al. 2002), and on Bennu it is ∼0.13 ± 0.04 (R. T. Daly et al. 2022); the mean geometric depth-to-diameter ratio on Dimorphos is 0.152 ± 0.04 (O. S. Barnouin et al. 2024). Though our dataset is only three craters, the Dinkinesh values share consistent, low d/D values seen on other asteroids (compared with $d/D \sim 0.2$ for fresh, simple craters on terrestrial planets; e.g., R. J. Pike 1980).

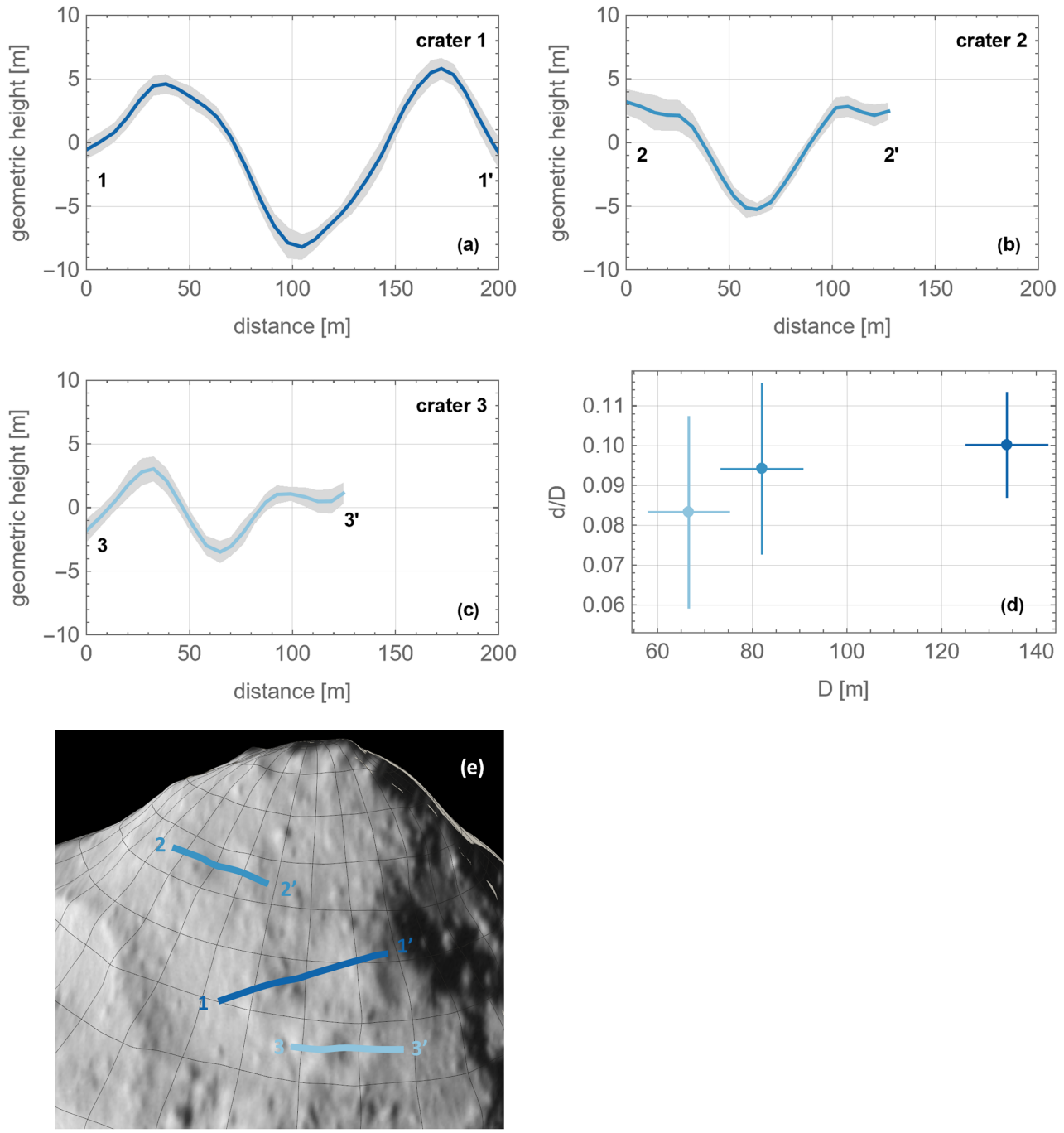

Figure 7. Crater depth-to-diameter (d/D) ratios for three of the best-resolved craters. Panels (a)–(c) are profiles of geometric height; each panel is the same scale to visually preserve the relative differences in diameter and depth between craters. The height is the solid line, which is bounded by a gray band that represents the 1σ radial error for each shape model facet in the profile. (d) The d/D values for the three craters as a function of D. The colors correspond to the profile colors in panels (a)–(c). (e) The location of the profiles on the body. The crater number and the primed number indicate the direction of the profiles in panels (a)–(c).

4. Boulder Population

Boulders are a fundamental component of rubble-pile asteroids. Boulder SFDs provide information regarding the partition of mass across the surface (how much mass exists within a particular diameter range) and fragmentation mechanics, and boulder morphology can contribute to understanding surface properties and characteristics of the parent body. While the image resolution from the Dinkinesh flyby was insufficient to investigate boulder morphology, the images do resolve a population of boulders distributed across the surface. While characteristics of Selam suggest a surface covered in regolith, the images do not unambiguously resolve a boulder population on the moon; we discuss surface characteristics of Selam in Section 5.2.

4.1. Boulder Measurement Process and Derived Boulder SFDs

Our measurement process for boulders was similar to that of craters, except that we did not identify different categories of confidence. Two coauthors, E.B.B. and S.J.R., independently measured the boulder population. The E.B.B. measurements

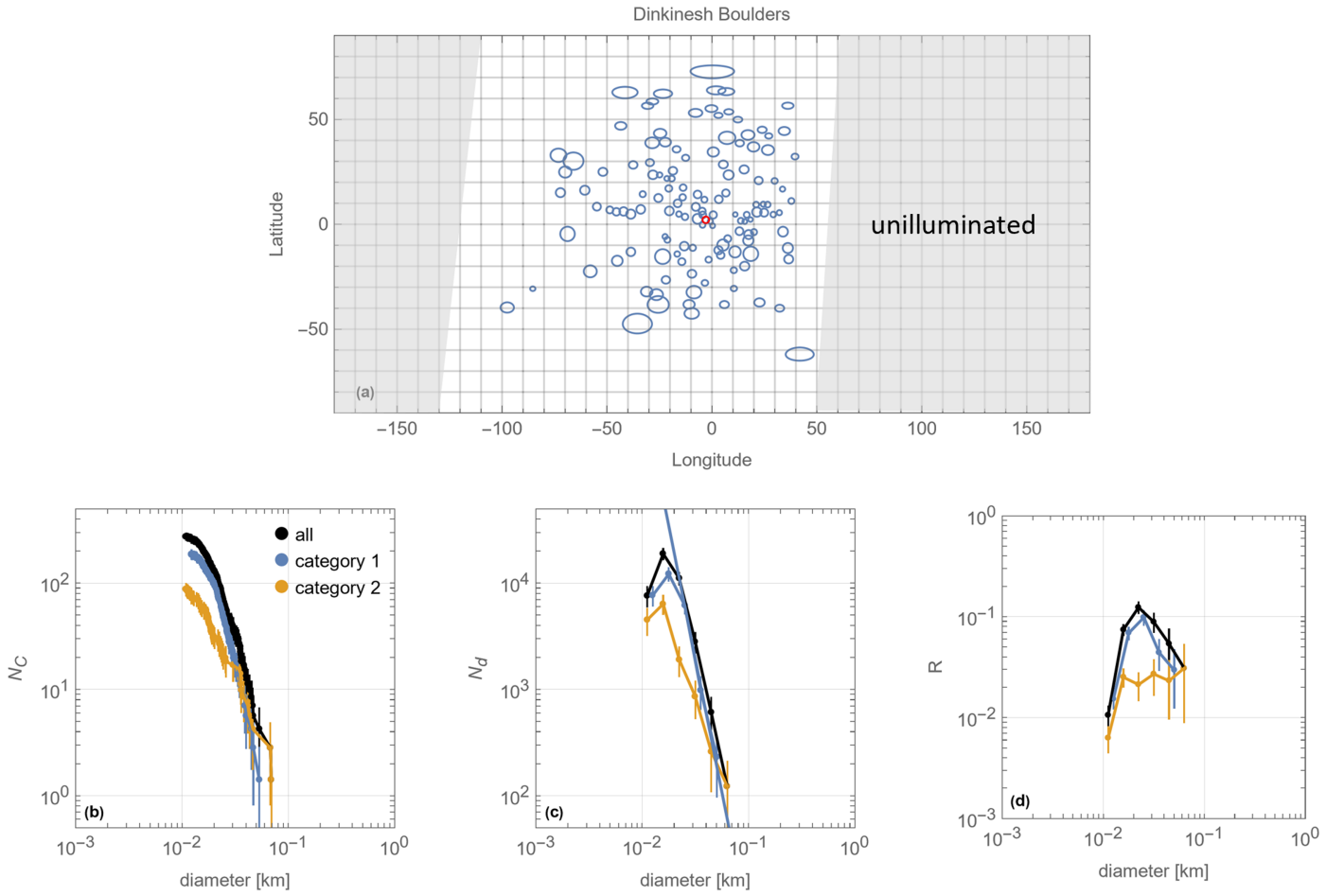

Figure 8. The measured Dinkinesh boulder population. (a) The spatial distribution of the category 1 boulder population. The light-gray regions are approximately the unilluminated surfaces not seen during the flyby. The actual dawn and dusk terminators are irregular owing to surface topography and span a range of ∼10°–15° longitude, depending on latitude. The red boulder is Totoka Saxum, the reference boulder that defines the prime meridian for the Dinkinesh coordinate system. Panels (b), (c), and (d) are the cumulative, differential, and relative versions of the boulder SFD, respectively. Error bars are Poisson sqrt-N. The black data are the unmerged combination of the two different datasets. The blue data are the merged category 1 population (plotted in panel (a)), and the orange data are category 2. The solid line in panel (c) is a weighted, least-squares fit to the category 1 data.

utilized the two unprojected images in Table 2. We used SPICE kernel information from the reconstructed trajectory and pointing (derived from the development of the shape model) to translate the pixel coordinates to body coordinates. We merged the measurements from these two images using the clustering process described in S. J. Robbins et al. (2014). Similar to the S.J.R. crater measurements, S.J.R. boulder measurements utilized images from throughout the flyby, projected onto the Dinkinesh shape model using SBMT. We then merged the E.B.B. and S.J.R. measurements using the process described in S. J. Robbins et al. (2014). Because we did not use a classification scheme for the boulders, the resulting boulder population has just two categories:

1. Merged category 1 boulders = boulders that both researchers identified.
2. Merged category 2 boulders = boulders that only one researcher identified.

The resulting spatial distribution of boulders (Figure 8) shows that while there is not an obvious spatial density contrast between the northern and southern hemispheres, there is a gradient in spatial density between the approach (eastern) and departure (western) hemispheres (Figure 8(a)). This decrease in spatial density correlates with reduced resolution and thus is likely an observational artifact. The resulting SFD from our measurements (Figures 8(b)–(d)) could be considered a shallow end-member of the actual population. We used the long axis of the boulders as the dimension used for the SFD fit, and the same lighting and viewing constraints discussed for the craters (Section 3.1) apply to the boulders. The boulder SFD decrease in spatial density, i.e., the rollover due to the completeness limit (Figure 8(c)), occurs near ∼20 m, which is smaller than the crater rollover, perhaps because the visual cues for a boulder are simplified relative to a crater. (Or, as discussed for the craters, there are several reasons why the actual crater population could have reduced numbers even above the completeness limit.) The weighted, least-squares fit to the differential form of the category 1 data ($N_d = kD^{-b}$, following the same definition as the crater SFD), for diameters larger than ∼20 m, results in $b = 5.02 \pm 0.76$; the best-fit slope to the cumulative form of the data (also for diameters >20 m) is $c = 3.93 \pm 0.15$. There are no boulders larger than 60 m, so we cannot generate a fit for a more conservative estimate of the completeness limit. However, we note that the SFD for the category 1 boulders (features identified by both researchers) is consistently steep for diameters >20 m, increasing confidence that the steep SFD is a true characteristic of the boulder population.

Table 3
Approved Feature Names for Dinkinesh and Selam

Feature Name	Feature Description	Name Description
	Dinkinesh	
Totoka Saxum	Boulder used to define the prime meridian (introduced in Section 4.1)	Fijian word for "beautiful"
Sumak Fossa	Large trough	Kichwa (Ecuadorian Quechua) word for "beautiful"
Fab Dorsum	Prominent equatorial ridge	English word derived from "fabulous"
Bella Dorsum	Elliptical ridge with northern and southern arcs	Italian word for "beautiful"
Indah Fossa	Long, narrow trough that appears to postdate other features	Indonesian word for "beautiful"
	Selam	
Piękna Lobus	Selam lobe closest to Dinkinesh	Polish word meaning "beautiful"
Lewa Lobus	Selam lobe furthest from Dinkinesh	Yoruba word for "beautiful"
Uwoduhi Dorsum	Ridge on Piękna Lobus	Cherokee word for "beautiful"

Though there is insufficient image resolution to assess morphology or otherwise categorize the boulder population, we identify one feature in particular because it defines the prime meridian for Dinkinesh: Totoka Saxum (see Section 5.0 for Dinkinesh feature names), with center location at $2\overset{\circ}{.}3$ latitude and $356\overset{\circ}{.}9$ longitude (Figure 8(a)).

5. Structural Features

The global "top shape" of Dinkinesh—including an equatorial ridge—is reminiscent of Bennu, Ryugu, Didymos, and others. However, the resolved morphology of the ridge and its distinct superposition over a large circumferential trough are (to date) unique to Dinkinesh. Dinkinesh expresses evidence of multiple length scales of regolith mobility and failure, including possible mass wasting and other troughs, which we address in this section.

We also introduce the IAU formally accepted names for key features; see Table 3. The name "Dinkinesh" comes from the Ethiopian (Amharic) name for the Lucy fossil, which translates as "you are wonderful" or "you are marvelous." The nomenclature theme approved by the Working Group for Planetary System Nomenclature reads, "Words for 'wonderful,' 'marvelous,' or 'beautiful' in the languages of the world. Note: For those languages where such words have separate spellings for the different grammatical genders, the feminine form is used to fit the feminine name of the asteroid, Dinkinesh, which defines the theme. This name means 'You are wonderful/marvelous' in Amharic as the local name for Lucy, the fossil remains of the female hominid discovered in Ethiopia in 1974."

5.1. Dinkinesh

Dinkinesh has equatorial dimensions larger than the polar dimension (H. F. Levison et al. 2024; Figure 3). We describe here the prominent features that contribute to large-scale topography across the observed hemisphere, from approximately large to small scale.

Sumak Fossa. A large trough named Sumak Fossa almost circumscribes the body (H. F. Levison et al. 2024; Figure 9). The plane of the trough is tilted relative to the body z-axis, with the northern portion of Sumak Fossa passing through the mid-latitudes, while the southern portion nearly intersects the pole (Figures 9(a) and (b)). The morphology of Sumak Fossa varies across both latitude and longitude. The approach view of Sumak Fossa revealed a significant valley at high southern latitudes (Figures 9(a)–(c)); although the perspective changes as the feature arcs into lower latitudes, it continues to express clear boundaries. The northern component has a less pronounced saddle geometry (Figures 9(a)–(c)), perhaps by virtue of cutting through the body at mid-latitude versus the high latitudes in the south. The departure view (the most western portion) shows that southern Sumak becomes broader (Figures 9(d)–(f), yellow trace and yellow/gold arrows). The western portion of northern Sumak becomes less pronounced (Figures 9(d)–(f), blue trace and light-blue arrow) and may not return to the equatorial ridge. Rather, it appears that another depression may extend down to the ridge.

Measurements of six profiles across different parts of Sumak Fossa quantify the width and depth of the feature (Figure 10). We measured the profiles with the same process used for crater d/D data (Section 3.5). The median depth and width for the six profiles are 20 and 189 m, respectively. The depth profile as a function of width is relatively consistent across the profiles (Figure 10(k)), except for profile 7, which is up to twice as deep as the other profiles. Profile 7 crosses Sumak in the southwest at mid-latitudes—this is the same region of the profile as the light-yellow arrow in Figures 9(d)–(f). This depression within Sumak has suggestions of a nearly complete rim, giving the impression of a crater-like feature. However, profile 7 has a depth/width ratio of 0.2 ± 0.02, which also is approximately twice as deep as the craters on Dinkinesh (Figure 7), and generally deeper than craters on other asteroids (M. S. Robinson et al. 2002; R. T. Daly et al. 2022; O. S. Barnouin et al. 2024).

Because the plane of Sumak Fossa does not pass through the center of the figure, the longitudinal span (from where it crosses the equatorial region at two locations) bounded by the feature is a wedge from ~90° to 120° wide (Figure 11). The southern portion of Sumak encounters the equatorial ridge at longitudes ~10°–30°E (Figure 11(a)), while the northern portion of Sumak encounters the equatorial ridge at longitudes ~0°–15°W (Figure 11(b)). The western and southern portion of Sumak encounters the equatorial ridge at longitudes ~80°–100°W (Figure 11(a)).

Fab Dorsum. Another major structural feature observed on Dinkinesh is an equatorial ridge, named Fab Dorsum. The ridge is present on all parts of the body observed during the encounter (Figure 12) and is superimposed over Sumak Fossa. Within the Lucy images the equatorial ridge is visible from ~45°E, through 0°, to ~150°W. The most western views have lower resolution because the closest approach occurred in view

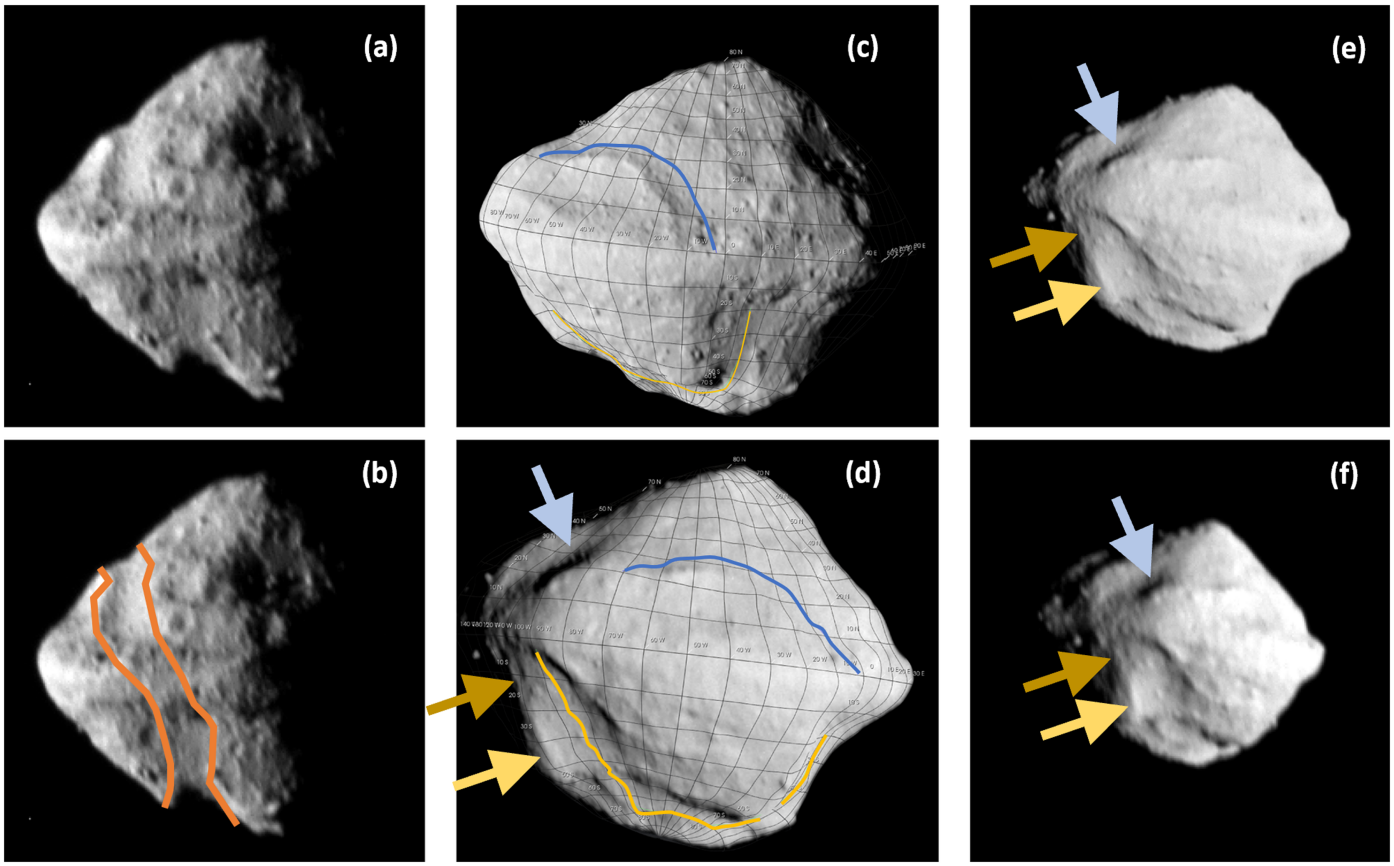

Figure 9. Sumak Fossa, the major trough on Dinkinesh. In all panels, north is approximately up. (a) Image lor_ 0752129497_ 03589, taken during approach at ∼80° phase and 3.3 m pixel^{-1}. This version is unannotated to show all features, including the "valley-like" morphology of Sumak Fossa at high southern latitudes. From this perspective the view looks nearly straight through the deep trough. (b) The same image as panel (a), with orange outlines to demark the boundaries of Sumak Fossa, which crosses the body at mid-latitudes in the north and close to the pole in the south. (c) Image lor_ 0752129617_ 03613, taken during approach at ∼28° phase and 2.1 m pixel^{-1}. The image is rendered on the shape model to illustrate the relative locations of Sumak Fossa seen from the eastern (∼approach) hemisphere. The blue and yellow lines trace the approximate path of Sumak Fossa in the northern and southern hemispheres, respectively. (d) Image lor_ 0752129707_ 03631, taken during departure at ∼15° phase and 2.9 m pixel^{-1}. This view provides among the highest-resolution views of the western side of Sumak Fossa. Here, too, the image is rendered on the shape model. In addition to the blue and yellow lines that trace the feature, the colored arrows point to transitions in the morphology of the feature as it arcs back toward the equator. The light-blue arrow points to the northern boundary of a depression that may be distinct from Sumak Fossa. The gold and light-yellow arrows point to the parts of southern Sumak Fossa that have different widths and depths. Panels (e) and (f) are images lor_ 0752129722_ 03634 and lor_ 0752129827_ 03655, departure images acquired at ∼19° phase and 3.2 m pixel^{-1} and at ∼37° phase and 5.1 m pixel^{-1}, respectively. The arrows point to the same features as in panel (d).

of the eastern hemisphere (Figure 2). While some discrete boulders are visible on the ridge (Figure 8), the vast majority of the ridge consists of textured but generally unresolved surface material (though some mass wasting is visible; see subsequent discussion). Given a best resolution of ∼12.6 m (one L'LORRI resolution element is 3 pixels wide; the best pixel scale is 2.1 m pixel^{-1}), the ridge must be dominated by particle sizes <12.6 m.

The profile of Fab Dorsum evolves across the observed longitudes (Figure 13). The ridge varies from being a local geopotential maximum (e.g., longitudes 0°–40°), to being located on a geopotential slope (e.g., −80° or −20° longitude), to being near the geopotential minimum (e.g., −120° or 100°). Each of the panels in Figure 13 includes a slope value, which is the average geopotential slope between the location of the geometric maximum value and geopotential minimum value (green points and red points, respectively). The slopes range from ∼6° to 18°, all of which are less than the typical angle of repose for granular materials (e.g., F. Elekes & E. J. R. Parteli 2021). Although the variation in geopotential height of the equatorial ridge contrasts with the approximately consistent minimum elevation of the ridge across all longitudes for Bennu (M. D. J. Scheeres et al. 2016; R. T. Daly et al. 2020), the offset of the geopotential minimum relative to the geometric maximum resides on low slope. This configuration suggests that the current long-wavelength topography of the equatorial ridge is generally stable, even if shorter length scales contain evidence for downslope movement (see subsequent discussion).

To calculate the volume of the ridge, we measured width and height values in the geometric height profiles (Figure 14(a)). While the ridge contains the maximum geometric height at all longitudes, the profile of the geometric height is also variable with longitude. Here we define the ridge geometric height as the difference between the maximum value and a line that connects the closest adjacent local minimum value on the northern and southern hemispheres (Figures 14(b)–(f)). To calculate a cross-sectional area for each profile, we first define a base that is a line connecting the two sides of the ridge and then include the area between that base and the profile (Figures 14(b)–(f)). We then applied the following steps to convert the areas to a ridge volume:

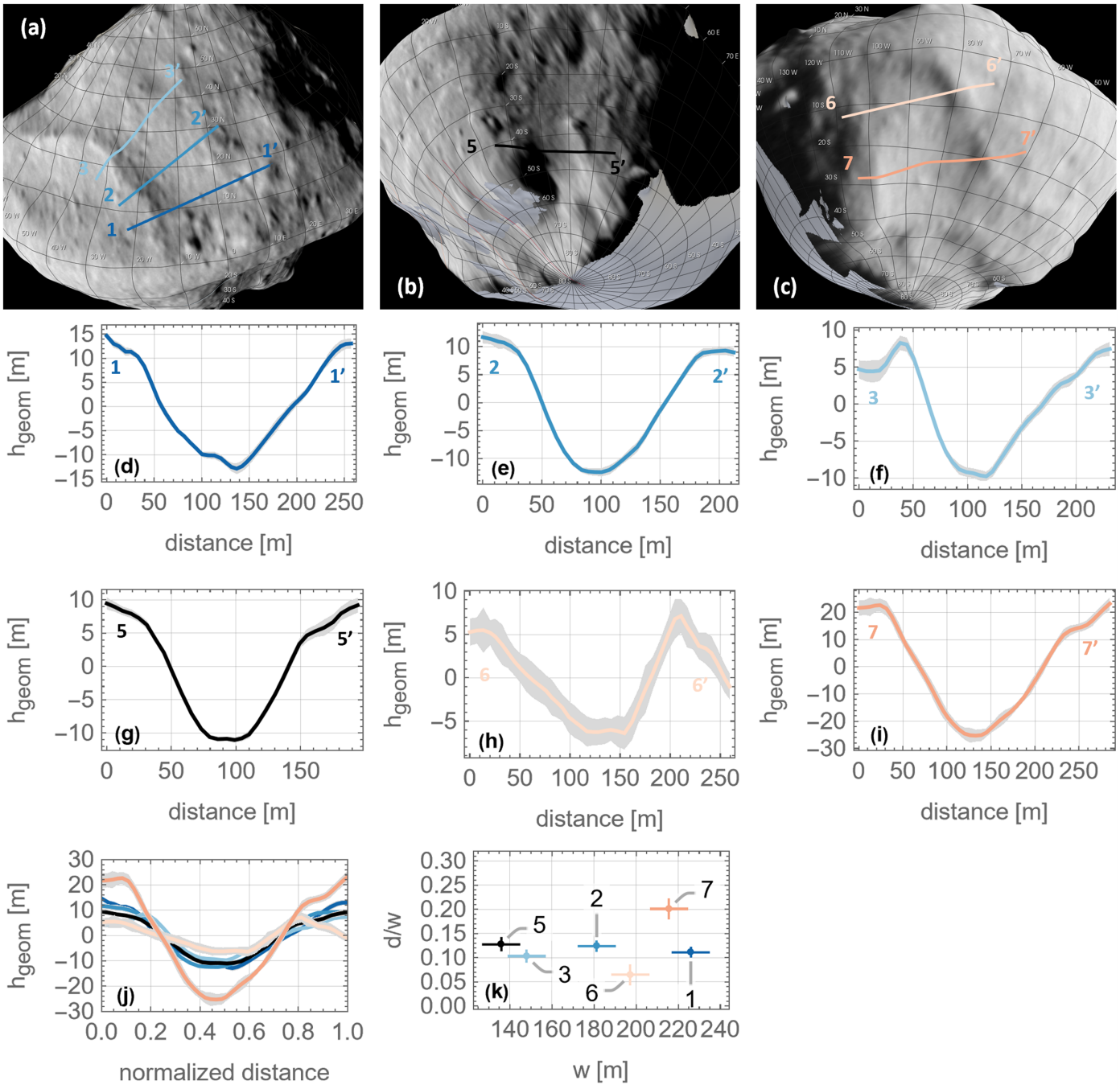

Figure 10. Sumak Fossa width and depth measurements. Panels (a)–(c) illustrate the locations of six profiles across Sumak Fossa. Each profile has a specific color that is consistent across the panels in this figure. The numbers are not sequential because we discarded some profiles owing to larger error. The unprimed and primed versions of the profile number indicate the profile direction (generally left to right) shown in subsequent panels. (a) Profiles 1–3 are in the northeastern hemisphere. (b) Profile 5 is in the southeastern hemisphere. (c) Profiles 6 and 7 are in the southwestern hemisphere. (d–i) The geometric height (h_{geom}) vs. distance for each profile after a linear detrending of the geometric height. The gray bands bounding each profile are the 1σ radial errors of the profile. (j) The profiles in panels (d)–(i) replotted with normalized distances, highlighting the unique depth of profile 7. (f) The depth/width ratio of each profile, labeled by profile number, and with colors consistent with panels (d)–(i). Error bars are derived from the propagation of errors for the depth and width measurements.

1. Calculate the center of figure for each of the cross-sectional areas and derive a radial value (from the center of the body) for that center of figure.
2. For adjacent pairs of profiles, calculate:
   a. the average of the two radii for their center of figures;
   b. the average of their cross-sectional areas.
3. For the values in step 2, calculate a volume for a shape that has the average cross-sectional area and that extends an arc length spanned by 10° (the distance between adjacent profiles) at the average radius.
4. Repeat step 3 for every adjacent pair of profiles and sum the total. The resulting volume is $1.51 \times 10^7\ \mathrm{m}^3$.
5. To derive an error on the volume, we consider both the formal uncertainty, derived from propagation of errors, and systematic errors arising from misalignments between our process to estimate the volume and the true volume.

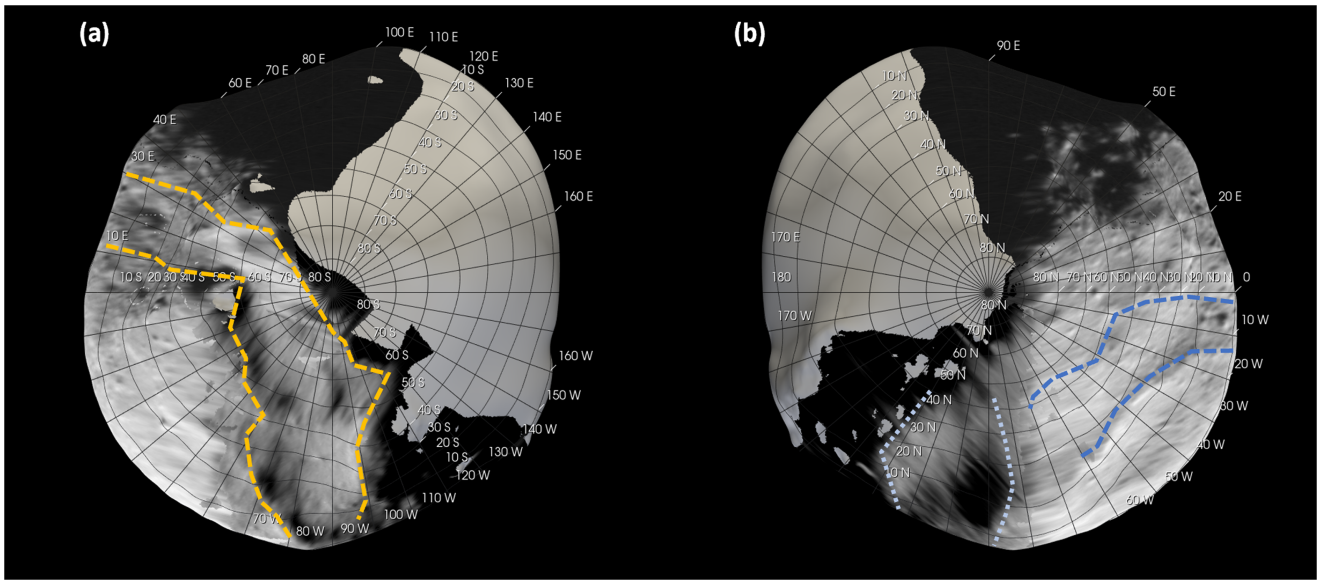

Figure 11. Polar views of Dinkinesh. Two images are projected on the shape model, lor_0752129617_03613 and lor_0752129707_03631. Panels (a) and (b) are the south pole and north pole, respectively. The dashed lines indicate the approximate boundaries of Sumak. In panel (b), the light-blue dotted lines indicate a depression that starts at the mid-latitudes and extends to the equatorial region, and it appears to be distinct from Sumak Fossa.

a. The formal uncertainty includes (i) the shape model radial error propagated into the area derived for each profile and further propagated into the average area of adjacent profiles that are averaged together, (ii) the shape model radial error propagated into the center-of-figure radius, and (iii) the combination of (i) and (ii) when using the areas and center-of-figure radii to calculate the ridge volume. This error is $0.58 \times 10^6\,\mathrm{m}^3$, or 3.9%.
b. The systematic error stems from our choice in the definition of ridge width and the corresponding effect on ridge height. While we do not have a rigorous quantification of the systematic error, we can bound its effect by considering the potential variability of the pre–Fab Dorsum surface. A key simplification we apply is to use a line to define the base of the ridge. The underlying surface prior to ridge formation likely was not linear, and the error in this assumption likely exceeds the magnitude of the radial error on the profile. However, it is also unlikely that the underlying surface is so different that our derived cross-sectional area is wrong by as much as 50% (i.e., it is unlikely that the true area could be half as small, or 1.5 times larger, than the shaded regions in Figure 14). We estimate, then, that the systematic error is greater than 4% and less than 50%. In this case the systematic error clearly dominates the formal error. As a compromise between being overly optimistic and being too conservative, we assign the systematic error to be 25%. The root sum square of the formal and systematic error is ∼25%.

Thus, our resulting volume for Fab Dorsum using the process above is $(1.51 \pm 0.38) \times 10^7\,\mathrm{m}^3$. This is the volume for the observed portion of the ridge. If we assume that the ridge circumscribes Dinkinesh and then scale by the ratio of the observed longitudes to the full body (about half the body was observed), then the total volume for Fab Dorsum is $\sim(3.0 \pm 0.8) \times 10^7\,\mathrm{m}^3$.

Adopting the axial dimensions for Piękna (240 × 200 × 200 m) and Lewa Lobus (280 × 220 × 210 m) from H. F. Levison et al. (2024), Selam's total volume is $1.07 \times 10^7\,\mathrm{m}^3$. This value is about 5% of the volume of Dinkinesh as calculated from our shape model above (i.e., $(2.1 \pm 0.2) \times 10^8\,\mathrm{m}^3$). Within the accuracy of the respective volume estimates, Fab Dorsum could contain between 2 and –3.5 times as much volume as Selam.

Bella Dorsum. Bella Dorsum is an arcuate, narrow ridge that has an approximately elliptical shape and is centered on the equator (Figure 15). Bella Dorsum is the first arcuate ridge (forming almost a complete oval) seen on an asteroid. Using the SBMT ellipse tool, we measure the equatorial dimension as ∼430 m. In the northern hemisphere Bella Dorsum marks the southern boundary of Sumak Fossa (Figures 15(a)–(c)). The maximum northern extent of the ridge is between 25°N and 30°N, which is ∼210 m from the equator. The eastern end of the northern arc intersects Fab Dorsum (Figures 15(a)–(c)). While there may be some morphological signs that Bella Dorsum continues through Fab Dorsa, the morphology is subtle and at the limit of the resolution. The western end of the northern arc, like Sumak Fossa, may not bend entirely back to reach the equator and instead may terminate into a longitudinal ridge structure at ∼20°N (Figures 15(e) and (f)). While the southern arc reaches a comparable maximum poleward latitude to the northern arc, between 25°S and 30°S, a notable difference is that most of the southern arc is a distinct feature from the southern portion of Sumak Fossa. The western end of the southern arc may intersect the low-latitude boundary of Sumak Fossa (Figures 15(e) and (f)). Although the longitudinal topographic profiles are not entirely symmetric (e.g., Figure 13), the maximum southern extent is also ∼210 m from the equator. The eastern side of the southern arc appears to be a topographic step rather than a ridge (Figure 15(a)); however, because this part of the feature is only a few pixels across, an accurate evaluation of the topography is challenging. As the southern arc moves westward, it gains a more ridge-like topography (Figures 15(e) and (f)). The lower resolution of these images limits the accuracy of dimensional comparisons

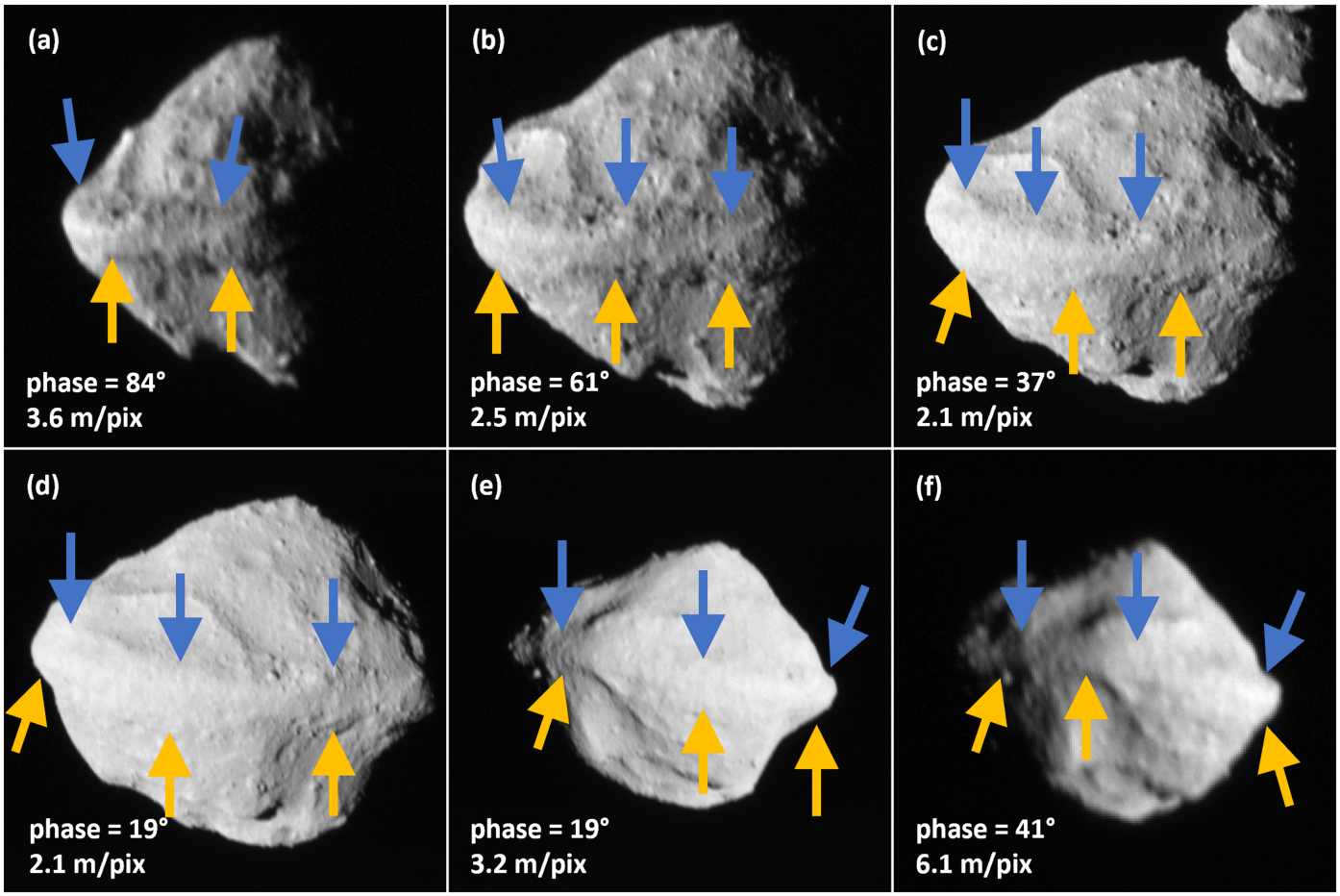

Figure 12. Views of Dinkinesh and Fab Dorsum, the equatorial ridge, throughout the encounter. The images selected are approximately 20° steps in phase angle, with some variation given the availability of images across the phase angles observed during the encounter, and to avoid saturated images. (For example, the images around 0° have significant saturation.) Blue and gold arrows point to the approximate northern and southern boundaries, respectively, of Fab Dorsum. Panels (a)–(d) are from the approach; panels (e) and (f) are from departure. Phase angles and pixel scales are derived from the predicted trajectory. (a) Image lor_ 0752129482_ 03586. (b) Image lor_ 0752129557_ 03601. (c) Image lor_ 0752129602_ 03610; Selam is visible in the upper right corner. (d) Image lor_ 0752129632_ 03616. (e) Image lor_ 0752129722_ 03634. (f) Image lor_ 0752129872_ 03664.

with the northern arc using shape model measurements; however, using image lor_0752129827_03655 to make pixel-based measurements of the peak-to-contact boundary gives consistent values of 4–5 pixels for both the northern and southern arcs.

The better-resolved northern arc enabled profile measurements (Figure 16) over that region of the feature. Adopting the height definition we used for Fab Fossa (from the maximum value to the bounding nearest local minimum) results in the minimum heights at the western and eastern (Figures 16(a) and (g)) contacts of the ridge with other surface features. One exception is profile 3, which passes through a "gap" in the ridge, which is evidence for ridge modification beyond the longitudinal ends. The ridge heights vary from ∼8 to ∼19 m, and the widths vary from ∼80 to ∼140 m.

Indah Fossa. Dinkinesh includes troughs that are significantly smaller than Sumak Fossa, with morphologies reminiscent of narrow features seen on Eros (L. M. Prockter et al. 2002, D. L. Buczkowski et al. 2008). The longest of these smaller troughs is Indah Fossa (Figure 17). Visible from a crater at ∼25°N to the Sumak Fossa "saddle valley" at ∼−45°S, Indah Fossa is ∼500 m long. While visible in multiple images, the width is just above the resolution limit, ∼6–7 pixels (12–15 m), across the whole length. Indah also is visible as it crosses Fab Dorsum, the only structural feature we found for which this is true. Indah's direction is generally north–south, though there is a longitudinal shift at the southern boundary of Fab. While the southern portion of Indah is also superimposed over Sumak, the northern portion of Indah follows a slightly eastward heading versus following the westward arc of Sumak (Figure 17(b)).

Mass wasting. Several examples of possible mass wasting appear on Dinkinesh at regions of elevated geopotential (Figure 18). We note two examples on Fab Dorsum, located near the intersection with the northeastern arc of Bella Dorsum (Figures 18(a)–(c)). These are located on geopotential gradients with directionality consistent with downslope movement (Figure 18(d)), with slope values between 20° and 30°. The terminal boundaries of both cases are discrete and approximately parallel to the shape of the upslope regions. These features show coherence over tens of meters, indicative of a threshold of failure over a regional scale, which is different from the small, local slope movement seen on Bennu (E. R. Jawin et al. 2020).

Though not well resolved and partially in shadow, there is a topographic depression in the northern hemisphere that emerges in the departure view (green arrow in Figures 18(d) and (e)). The southern boundary of this feature is Fab Dorsum,

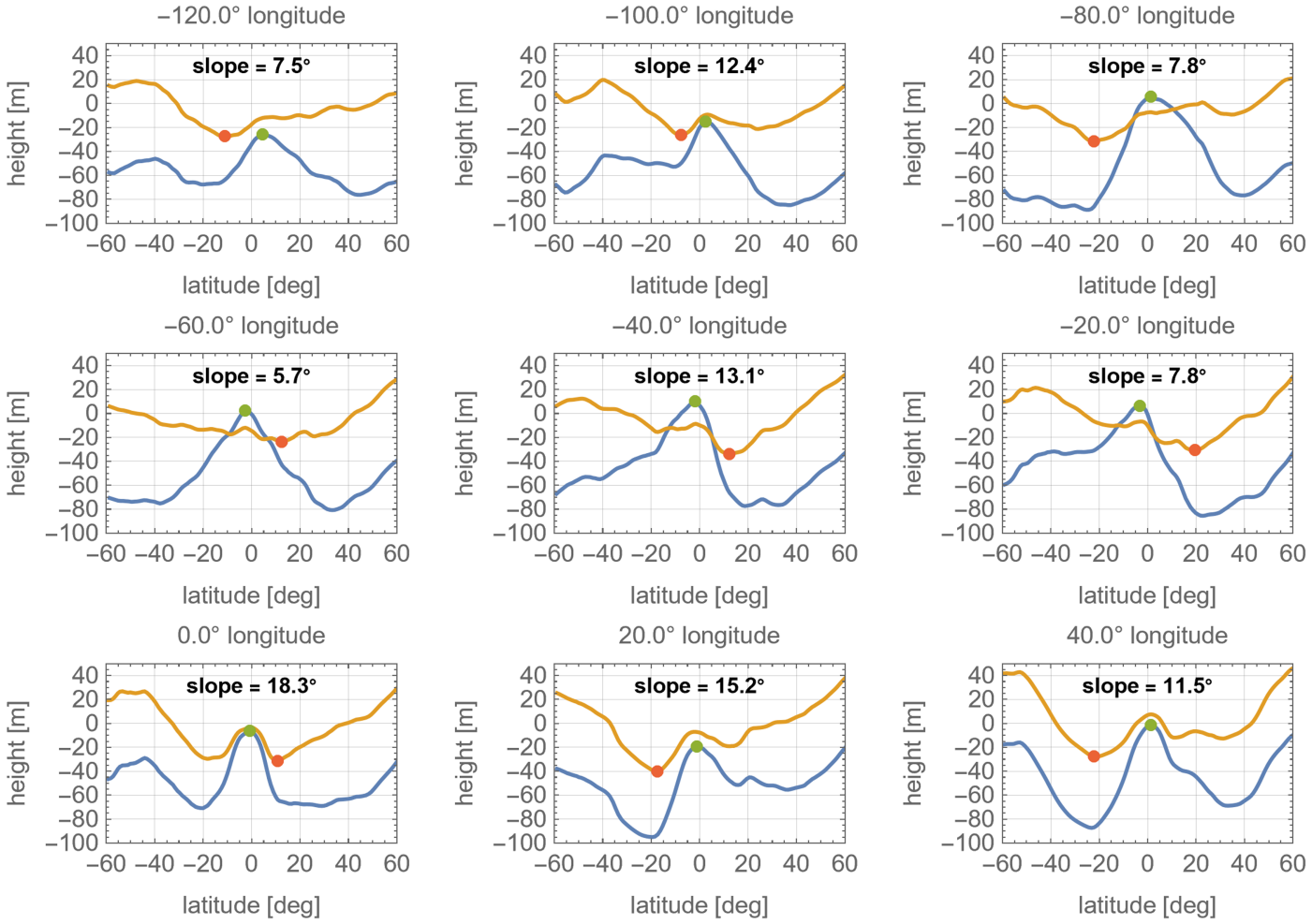

Figure 13. Detrended longitudinal profiles of Fab Dorsum. The blue line is the geometric height; the green circle marks the peak geometric height of the profile. The orange line is the geopotential height; the red circle marks the minimum geopotential height of the profile. Each panel includes the average geopotential slope (i.e., the slope of the orange line) between the latitudes spanned by the green and red circles.

while the northern boundary is occulted by a bounding, longitudinal feature. Though the oblique and low-resolution view prevents detailed assessment, the depression appears primarily longitudinal. In addition, the location appears to be a "mirror flip" of the Sumak Fossa. While we cannot reach a definitive conclusion, one possibility is that this depression is a Sumak-style extensional failure.

5.2. Selam

H. F. Levison et al. (2024) note that Selam was a surprise in two ways: first, the Lucy team did not know in advance that Dinkinesh is a binary system; and second, Selam is the first resolved observation of a secondary (i.e., the moon of a larger asteroid) that itself is a contact binary. They report that the major body axes are parallel to the Dinkinesh vector, with dimensions of 240 × 200 × 200 m for the inner lobe (now named Piękna Lobus) and 280 × 220 × 210 m for the outer lobe (now named Lewa Lobus). H. F. Levison et al. (2024) also note that Selam appears angular and blocky and has a ridge, compared with the oblate spheroid shape of Dimorphos (the ∼150 m secondary of the Didymos asteroid).

Selam has depressions that we interpret as craters (see Section 3), and while there are surface features suggestive of boulders, they are insufficiently resolved to make definitive measurements. We characterize Selam's surface as textured even if individual blocks are not resolved; similar to our evaluation of Dinkinesh, we conclude that the surface of Selam is dominated by particle sizes $<$12.6 m.

The geometry of Lucy's flyby resulted in high-phase observations of the Dinkinesh–Selam system on approach; in conjunction with the body-axis orientation relative to the Sun and the bilobed nature of Selam, there was significant self-shadowing during approach images (Figure 19(a)), especially of Lewa Lobus. Selam's orbital position during encounter meant that the spacecraft view near closest approach was almost parallel to the long axis of Selam, with Piękna Lobus in the foreground, almost completely occulting Lewa Lobus (Figures 19(b) and (c)). Selam left the L'LORRI field of view (FOV) about ∼7 s prior to closest approach and completely returned to the L'LORRI FOV ∼784 s after closest approach (Figure 19(d)). The departure view provided direct views of both lobes, essentially on the opposite side seen from approach. Because of the greater range of the departure views, the resolution is more than three times lower than the views near closest approach. In summary, the L'LORRI coverage of Selam provides (i) the most favorable combination of phase angles and resolution for the Dinkinesh-facing side of Piękna Lobus, (ii) α greater than 40° and low resolution for the western (departure) hemispheres, and (iii) limited coverage of

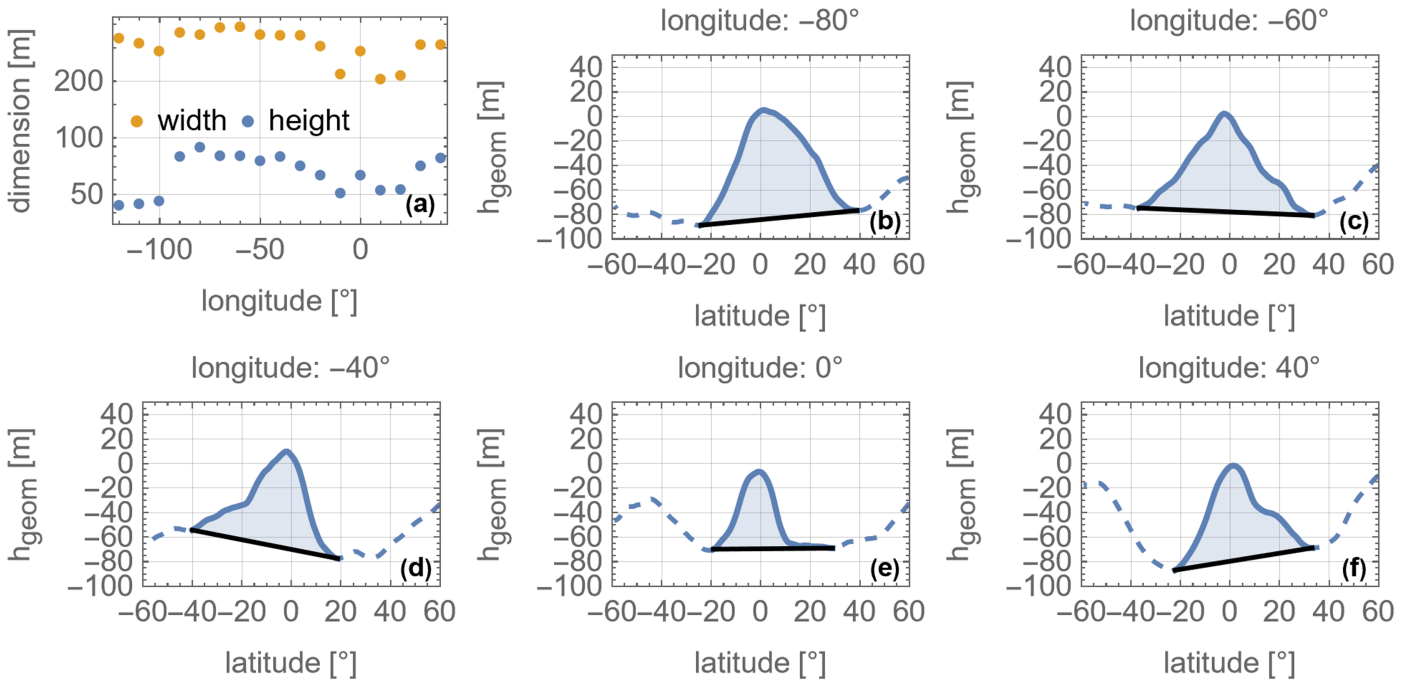

Figure 14. Fab Dorsum height and width measurements, and examples of derived cross-sectional areas for Fab Dorsum. (a) Fab Dorsum height and width values across observed longitudes. (b–f) The profiles are a representative subset of the geometric profiles in Figure 12. The dashed and solid blue lines are the longitudinal profile and the Fab Dorsum portion, respectively. The black line connects the northern and southern boundaries of Fab Dorsum in each profile, and the light-blue shaded region is the cross-sectional area of Fab Dorsum for that profile.

Lewa Lobus. Nevertheless, the existing data permit characterization of the overall shape and size (e.g., H. F. Levison et al. 2024), as well as the largest surface features.

Piękna Lobus. A prominent feature on Piękna Lobus is a ridge, now named Uwoduhi Dorsum. While it is possible to trace the feature to approach images with pixel scales as much as $\sim$3.6 m pixel^{-1}, clarity that the feature is a ridge does not occur until pixel scales $<$2.5 m pixel^{-1}. In the best-resolved images of Piękna Lobus (e.g., Figures 19(b) and (c)) the ridge is $\sim$17 m wide over the most prominent part of the feature. There is a topographically subtle but present widening of the ridge base as it approaches the terminator on the eastern side of Piękna (yellow arrow in Figure 19(c)); the widest portion is $\sim$38 m across. The ridge peak morphology implies that it may be constructed of individual blocks, but no block is clearly resolved as an individual entity. There are nearly linear features that cross the high northern latitude portion of Piękna (Figures 19(b) and (c), and yellow dashed lines in panel (f)). In addition, the departure view (Figure 19(e)) reveals other linear features crossing the visible hemisphere, as well as a nearly planar geometry to the Dinkinesh-facing hemisphere. It is unclear whether these features are in the same plane as (or at least parallel to) the features seen on the Dinkinesh-facing hemisphere. In any case, the presence of multiple linear structures that span essentially the full diameter of Piękna suggests that there have been and/or continue to be stresses acting through the volume of this lobe.

Lewa Lobus. Only small portions of Lewa Lobus are visible during the inbound and near-closest-approach images; the best views of Lewa Lobus occur during departure. Despite this single perspective and low resolution, there are several compelling characteristics. Though the actual physical contact with Piękna Lobus is in shadow, the closest portion of Lewa to Piękna is nearly planar. Roughly the central third of the body has a recessed "notch" that creates a V-shaped depression. The third of the body that is farthest from Piękna appears more rugged, and the last visible portion of this lobe is a thin feature that is offset from the profile of the rest of the lobe. This thin feature is approximately parallel to the plane of Piękna's Dinkinesh-facing hemisphere.

6. YORP Evaluation

The YORP effect (Yarkovsky–O'Keefe–Radzievskii–Paddack, the last names of four people whose work provide important context for the process; D. P. Rubincam 2000) is a solar-flux-driven process that can change the spin state of an asteroid. Briefly, the irregular shape of asteroids, in conjunction with the asymmetric absorption and the thermal reradiation of incident solar photons, creates a small but continuous torque on an asteroid (D. P. Rubincam 2000; T. S. Statler 2009). Though small, the cumulative effect of this process can change the spin period and the spin obliquity. Over time, YORP reorients the spin axis of asteroids smaller than a few tens of kilometers to values near 0° or 180°, values that produce maximum Yarkovsky drift speeds in semimajor axis (e.g., W. F. Bottke et al. 2006; D. Vokrouhlický et al. 2015). Observations of thousands of asteroids by the Gaia spacecraft indicate that most smaller asteroids have such extreme spin obliquity values (J. Ďurech & J. Hanuš 2023). If left uninterrupted (e.g., lack of impact large enough to randomize the spin axis and rate), YORP will continuously decrease or increase the spin rate. In the case of spin-up, the body's fate depends on its strength, both at the surface and within the interior. In the case of a homogenous strength, K. A. Holsapple (2001, 2004, 2010) demonstrated that the body can adjust its shape to retain integrity up to a point; eventually, the stresses caused by the increasing angular momentum exceed a strength threshold, and the body will fail.

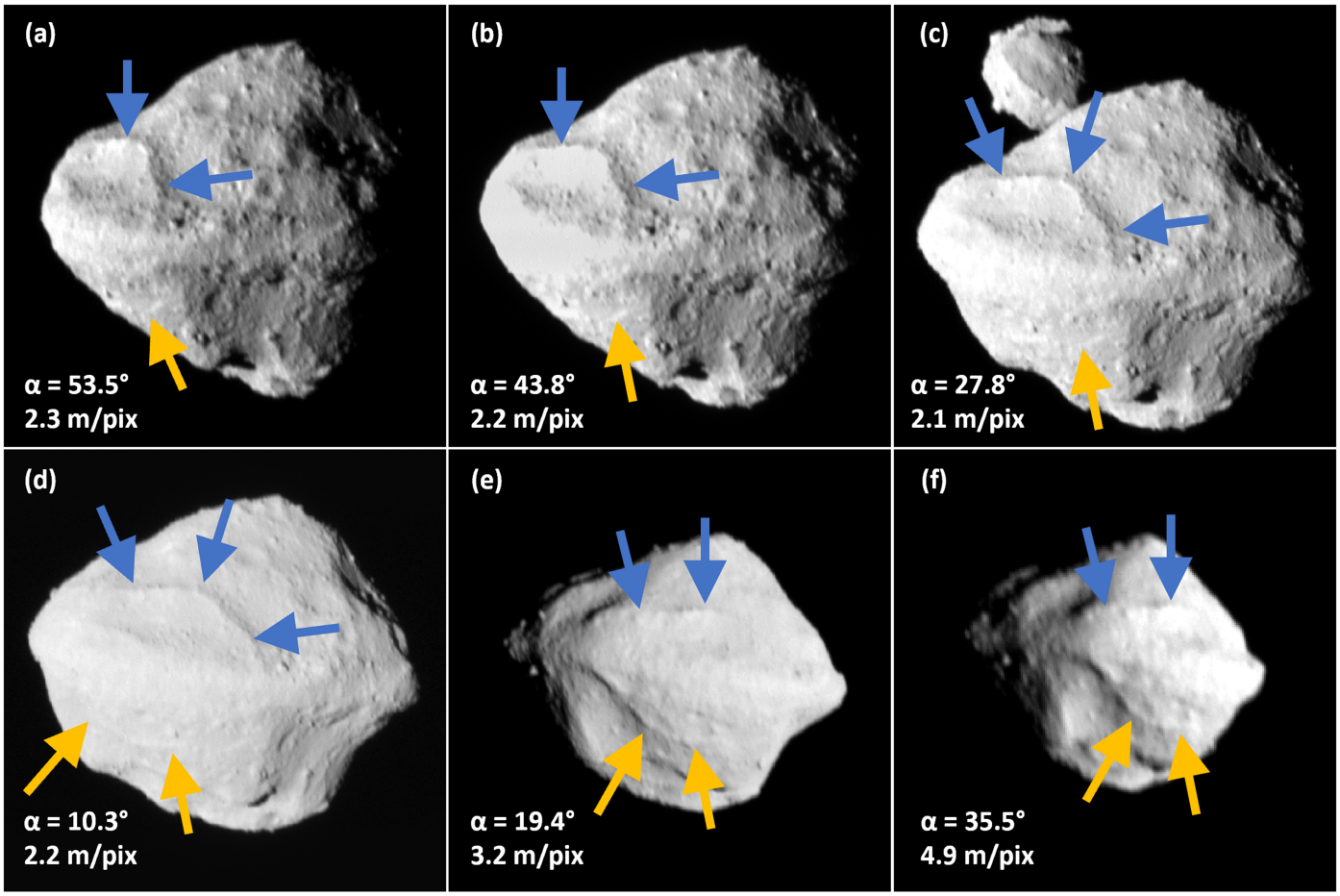

Figure 15. Bella Dorsum from multiple views throughout the flyby; north is approximately up in all panels. The blue and gold arrows point to the northern and southern arcs, respectively. Each panel includes the phase angle and pixel scale of the image shown. The images are (a) lor_0752129572_03604; (b) lor_0752129590_03608; (c) lor_0752129617_03613, with Selam visible behind Dinkinesh; (d) lor_0752129647_03619; (e) lor_0752129722_03634; and (f) lor_0752129827_03655.

Multiple models assess the correlation between asteroid physical properties and the potential YORP evolutionary pathways (e.g., D. J. Scheeres 2007, 2015; K. J. Walsh et al. 2008; S. A. Jacobson & D. J. Scheeres 2011; P. Sánchez & D. J. Scheeres 2014, 2016; M. Hirabayashi et al. 2015, 2020; S. Tardivel et al. 2018; Hirabayashi and Scheeres 2019; R. Hyodo & K. Sugiura 2022; H. F. Agrusa et al. 2024; see also reviews in J.-L. Margot et al. 2015; K. J. Walsh & S. A. Jacobson 2015; K. J. Walsh 2018). Here we summarize a subset of outcomes from these works that are relevant to the Dinkinesh–Selam system:

1. The location and type of failure depend on whether the body has a homogeneous or heterogeneous strength. In the case of heterogeneous strength, further variation is possible depending on whether the surface is weak and the interior is strong, or vice versa.
2. The strength needed to prevent failure, even at relatively fast spin rates, is only a few to tens of Pa. Thus, high strength in the context of YORP still could be orders of magnitude smaller than the tensile strengths of many rock types on Earth.
3. YORP failure can lead to the creation of a moon from a mass-shedding event on the primary body. This process requires a weak surface to provide enough mobilized material to form the moon.
4. The primary in the system can fail more than once, leading to multiple mass-shedding events.
5. After initial formation, the secondary also experiences YORP, and under certain circumstances it can fission into two objects (S. A. Jacobson & D. J. Scheeres 2011, A. B. Davis & D. J. Scheeres 2020). One of the two fissioned pieces can reimpact the primary or be ejected, or the two pieces can reconnect.

6.1. Modeling YORP Stress

To model the YORP stress within Dinkinesh, we use the approach described in M. Hirabayashi et al. (2020) and R. Nakano & M. Hirabayashi (2020). Briefly, their technique calculates the stress within a spinning triaxial ellipsoid assuming that no plastic regimes can hold stresses. The derived stress field, given a linear elasticity constitutive law, aka Hooke's law, provides the minimum necessary strength within the volume that is needed to prevent the object from failure. The strength to resist failure varies volumetrically as a function of the body-axis dimensions, bulk density, and spin period. The model computes the cohesive strength based on the Drucker–Prager yield criterion, assuming a friction angle of 35°, consistent with geological analysis of rubble-pile asteroids (C. Q. Robin et al. 2024). The Dinkinesh shape model and the mutual orbit of the Dinkinesh–Selam system provide a reasonably strong constraint on the bulk

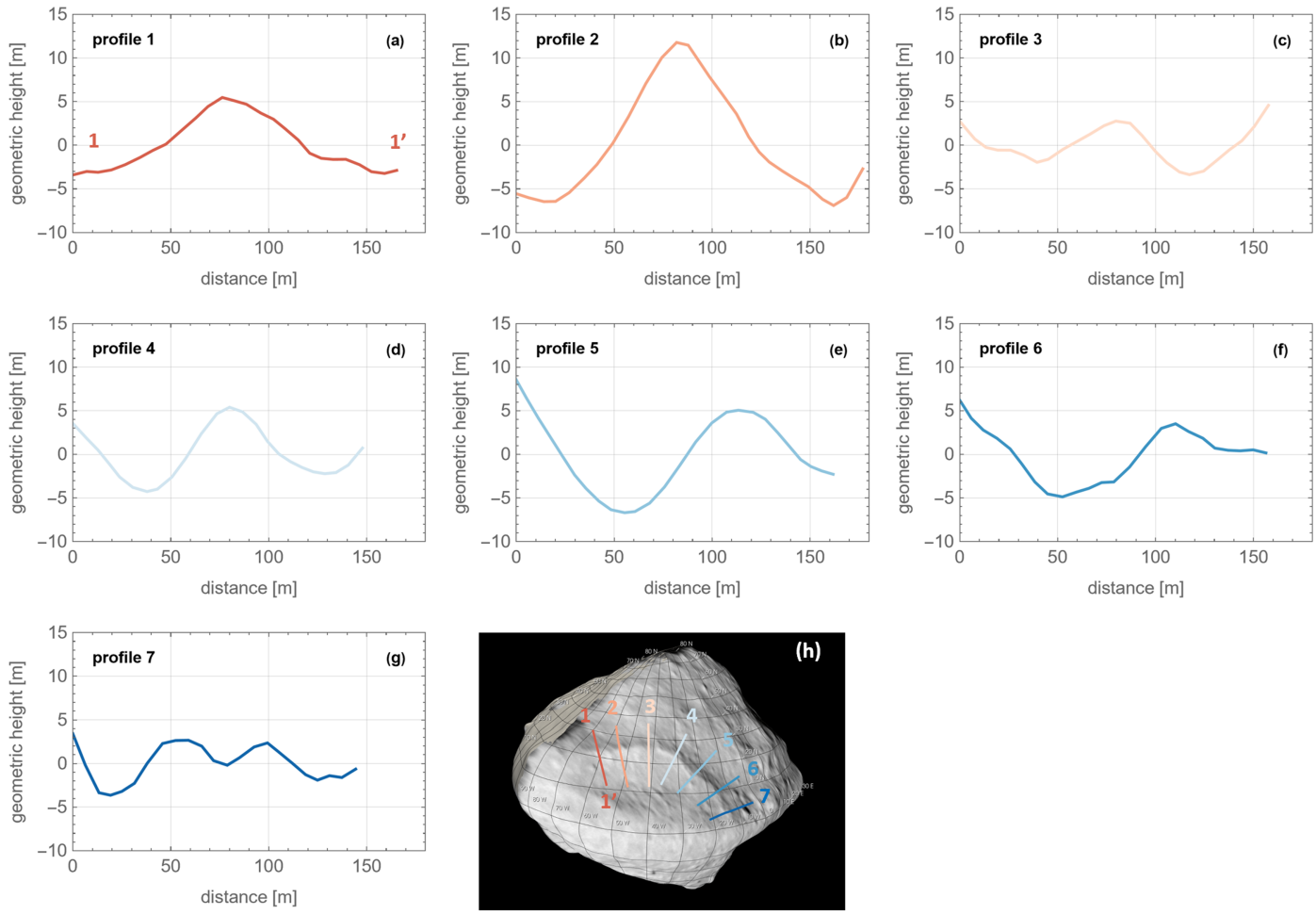

Figure 16. Detrended geometric height profiles of Bella Dorsum. Panels (a)–(g) are profiles across the northern arc. (h) The location of the profiles using image lor_0752129617_03613 projected onto the shape model. Panel (a) notes the direction of the profiles relative to panel (h): all profiles start on the side closest to the limb and move inward.

density of Dinkinesh (2220 ± 350 kg m^{-3}; see Section 2.2). Assuming that the current Dinkinesh shape reflects YORP failure also implies that the body dimensions have changed in response to YORP-driven deformation due to increasing spin rate; thus, we consider combinations of spin rate and body dimensions (Figure 20). For the spin period we consider (i) the current 3.7387 hr value (H. F. Levison et al. 2024), (ii) the 2.3 hr spin barrier limit (e.g., P. Pravec & A. W. Harris 2000), (iii) a series of spin rates that bracket rapid evolution of body interior stresses, and (iv) a longer 5 hr value to examine the effect of a lower spin rate. For a pre-failure shape, we assume that (1) all of Selam's volume was originally a part of Dinkinesh and (2) that the Dinkinesh shape change from mass shedding was elongation in the equatorial dimensions (the *a*- and *b*-axes) and a reduction in *c*-axis. The corresponding full-body dimensions are 811, 791, and 788 m.

As explained by M. Hirabayashi et al. (2020), the region of peak rotationally induced stress evolves from the surface at slow spin rates to the interior at fast spin rates. As one would intuitively expect, the fastest-spinning case requires the most strength, with values reaching ∼50 Pa at the center (Figures 20(a) and (i)). As rotation rate slows, the strength needed to prevent failure decreases, and the contours of stability with zero strength evolve from two distinct regions at the poles to a single region that encompasses increasing volume. At the current spin rate, both shapes considered (Figures 20(g) and (k)) are consistent with a strengthless interior. Though these results indicate that the bulk of the interior volume could be strengthless, note that these results are just maps of the strength needed to resist failure and are not predictive of the interior strength for a specific rotation rate—i.e., the plots show predicted stresses caused by spin and not the strength distribution in the body.

We address several observations that emerge from comparing the outcomes across Figure 20. In the following discussion we use the 0 Pa contour (red curves in Figure 20) as a useful marker for the evolving stress across rotation rates; the same behavior will be true for small positive strength values.

1. For the parameters used in this simulation the two distinct polar volumes bounded by the 0 Pa contour expand and connect at a rotation period of ∼3.19 hr (Figure 20(c)). As the spin rate changes by just 0.05 hr (only 180 s), the contour expands rapidly to occupy a larger fraction of the equatorial volume.
2. The 0 Pa contour passes through an "hourglass shape" that is wider at high latitudes and narrower at lower latitudes. The equatorial region of the contour expands with incremental increases in the spin period, which both pushes the contour to higher radial values at the equator and increases the latitude at which the zero contour approaches the surface.

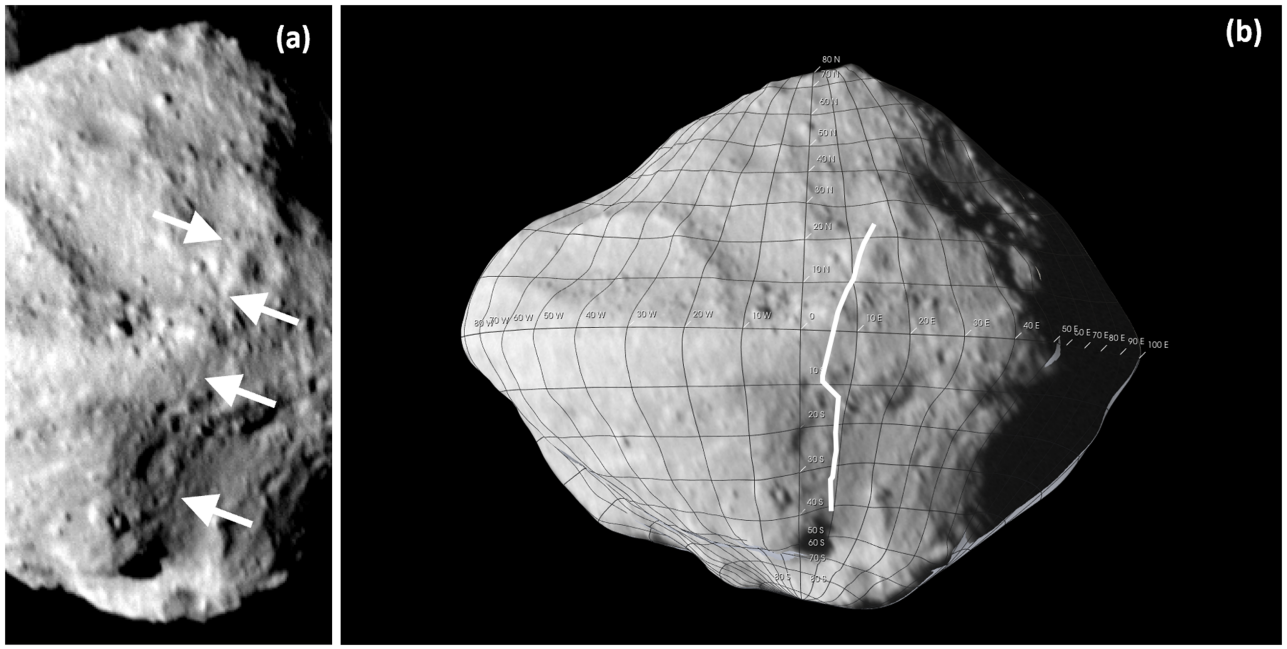

Figure 17. The largest of the most recent troughs, Indah Fossa. Dinkinesh north is approximately up in both panels. (a) Multiple white arrows indicate the feature as seen in the unprojected L'LORRI image lor_0752129617_03613. (b) The same L'LORRI image projected onto the shape model; the thick white line is a mapping of the feature on the shape model using SBMT.

3. The two shapes we considered have similar results; thus, the modest change in body dimensions resulting from redistributing the mass of Fab Dorsum to higher latitudes also would evolve similarly.

We discuss the relevance of these results to the Dinkinesh–Selam system in Section 7.

6.2. Modeling YORP Timescales

As noted above, the precise nature of mass-shedding events on small asteroids by YORP spin-up depends on several asteroid parameters: shape, strength, surface structure, etc. It is also possible that some of these events mobilize enough material to reset the surface, making this mechanism a potential rival with collisions in the generation of surface reset events. While the flyby data provide estimates for a partial shape model, a bulk density, and constraints on interior strength, at this time we do not have accurate global-scale properties at the resolution needed to calculate a Dinkinesh-specific timescale. Instead, we estimate the process using a zeroth-order scaling relationship for YORP spin-up timescales.

Using the work in D. Čapek & D. Vokrouhlický (2004), who estimated YORP spin-up on a large sample of Gaussian spheres (i.e., mathematical potato-shaped objects), we estimate that the timescale of spin for a generic asteroid up to the mass-shedding limit is given by the following equation from W. Bottke et al. (2025):

$$T \sim [25 \text{ to } 50 \text{ Myr}](D/(1 \text{ km}))^2 (a/(2.5 \text{ au}))^2(\rho/(2.5 \text{ g cm}^{-3})),$$

where D is the diameter of the target asteroid, a is the semimajor axis, and ρ is the bulk density of the asteroid. This scaling law attempts to fold in conditions where small shape changes produced by impacts, minor landslides, boulder movement, etc., can lead to changes in the direction of the spin rate (e.g., T. S. Statler 2009; W. F. Bottke et al. 2015). Objects may also reconfigure themselves in response to an increase in rotational angular momentum from YORP, which can in turn lengthen the time needed to reach mass-shedding spin speeds. The roughly symmetrical top-like shape of Dinkinesh is less susceptible to strong YORP spin-up than potato-like shapes (e.g., D. P. Rubincam 2000; W. F. Bottke et al. 2006; D. Vokrouhlický et al. 2015).

The minimum and maximum values of T above are the two blue curves in Figure 21(a). These values are shown over a range of diameters, using the bulk density (2.2 g cm^{-3}) and a semimajor-axis value (a = 2.19 au) for Dinkinesh. We find that the timescale for Dinkinesh spinning up to disruption (i.e., the 2.3 hr spin barrier; P. Pravec & A. W. Harris 2000) is on the order of 10–20 Myr. This timescale is less than the estimated collisional disruption timescales of both Dinkinesh and Selam (Figure 21(b)). In Section 7 we discuss this range in the context of the crater-derived surface age.

7. Discussion

The measurements in the previous sections enable us to make comparisons with other asteroids, as well as frame a basic history for the Dinkinesh–Selam system. We first focus on crater and boulder populations because of the greater availability of these datasets from other asteroids. We then consider the long-term and near-term history of the system. Finally, we synthesize these evaluations into possible physical trends across comparisons of asteroid size, spectral class, and dynamical residence (i.e., MBA vs. NEA).

7.1. Crater SFD Comparison with Other Asteroids

Comparing crater SFDs between asteroids depends, in part, on understanding how the SFDs were derived. Reported SFDs are often in cumulative format (despite the drawbacks of that format, C. R. Chapman & R. R. Haefner 1967), and thus we

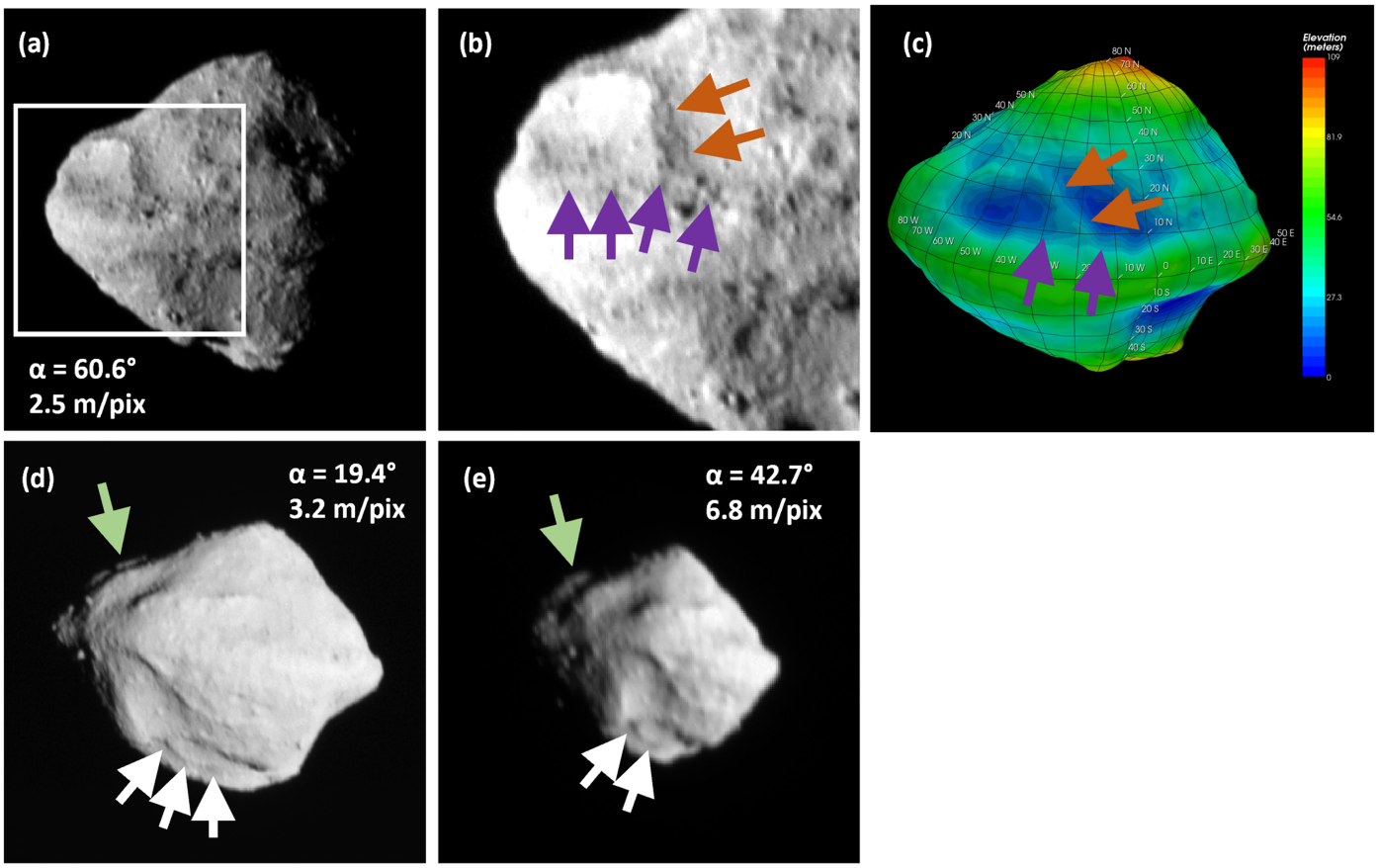

Figure 18. Examples of downslope movement on Dinkinesh. (a) Context view from lor_0752129557_03601; the white square outlines the region shown in panel (b). (b) A contrast stretch that enhances the visibility of two regions of downslope movement. The purple arrows point to a curvilinear feature on the flank of Fab Dorsum; the rust-colored arrows point to material that appears to be slumping from Bella Dorsum. (c) The Dinkinesh shape model colorized by geopotential elevation, with purple and rust-colored arrows pointing to approximately the same locations as in panel (b), illustrating that the location and apparent direction of material are consistent with moving in the local downhill direction. (d) Image lor_0752129722_03634. The white arrows point to apparent downslope movement inside Sumak Fossa. The light-green arrow points to a portion of the body that is just emerging into view during departure. (e) Image lor_0752129905_03671. The white and green arrows point to the same features as in panel (d). Though lower resolution, the feature identified by the green arrow is clearly separated from the foreground of the body by a depression.

use cumulative fits for this discussion. In addition, researcher decisions regarding the minimum diameter to use (due to the completeness limit or other factors), as well as over what diameter range to make the fit (due to variations in the data), affect the outcome. Not all of these factors are reported in published papers. As a result, a rigorous comparison with a common set of decisions for the SFD fit is challenging. Here we use our Dinkinesh data, in conjunction with available measurements for Ryugu, Bennu, and Itokawa, to make common decisions regarding the diameter range over which to calculate the SFD. This analysis provides a more standardized comparison of the crater SFDs of rubble-pile asteroids $\leqslant$1 km in diameter.

Even though we compare the cumulative fits, we use the differential form of the data to make decisions regarding minimum and maximum diameters for the fit; see Figure 4(b) for Dinkinesh differential data and E. B. Bierhaus et al. (2022), Extended Data Figure 8(c) for the differential forms of Ryugu, Bennu, and Itokawa. Advantages of the differential form of the crater SFD include (1) increased clarity into the rollover diameter, which is the diameter at which crater abundance no longer increases as crater diameter decreases, and (2) changes in slope across the SFD.

Caveated by small number statistics, we find two behaviors in the crater SFDs for these four asteroids. In the first case, demonstrated by Dinkinesh and the reported Ryugu population, there is not a strong peak in the differential crater SFD, though there are clear changes in slope. In the second case, demonstrated by Bennu and Itokawa, there is a strong peak in the differential crater SFD that is meaningfully above the completeness limit. Based on the location of the rollover and change in slope, we make multiple fits to each dataset (Table 4).

Our crater SFD slope values for Dinkinesh are shallow, though within the range of crater SFDs observed on similarly sized asteroids of Itokawa, Ryugu, and Bennu (P. Michel et al. 2009; N. Hirata et al. 2020; E. B. Bierhaus et al. 2022). We do not find a systematic trend for two types of SFDs described in the previous paragraph, nor do we find systematic values for the NEAs that would be a basis to evaluate whether the singular small MBA crater SFD from Dinkinesh is distinctive. The derived slope on a given body varies depending on the diameter range of the fit and, in the case of Dinkinesh, which crater categories are included in the fit. The cumulative SFD for Dinkinesh for all craters from all categories is almost identical to the Itokawa cumulative SFD for craters larger than

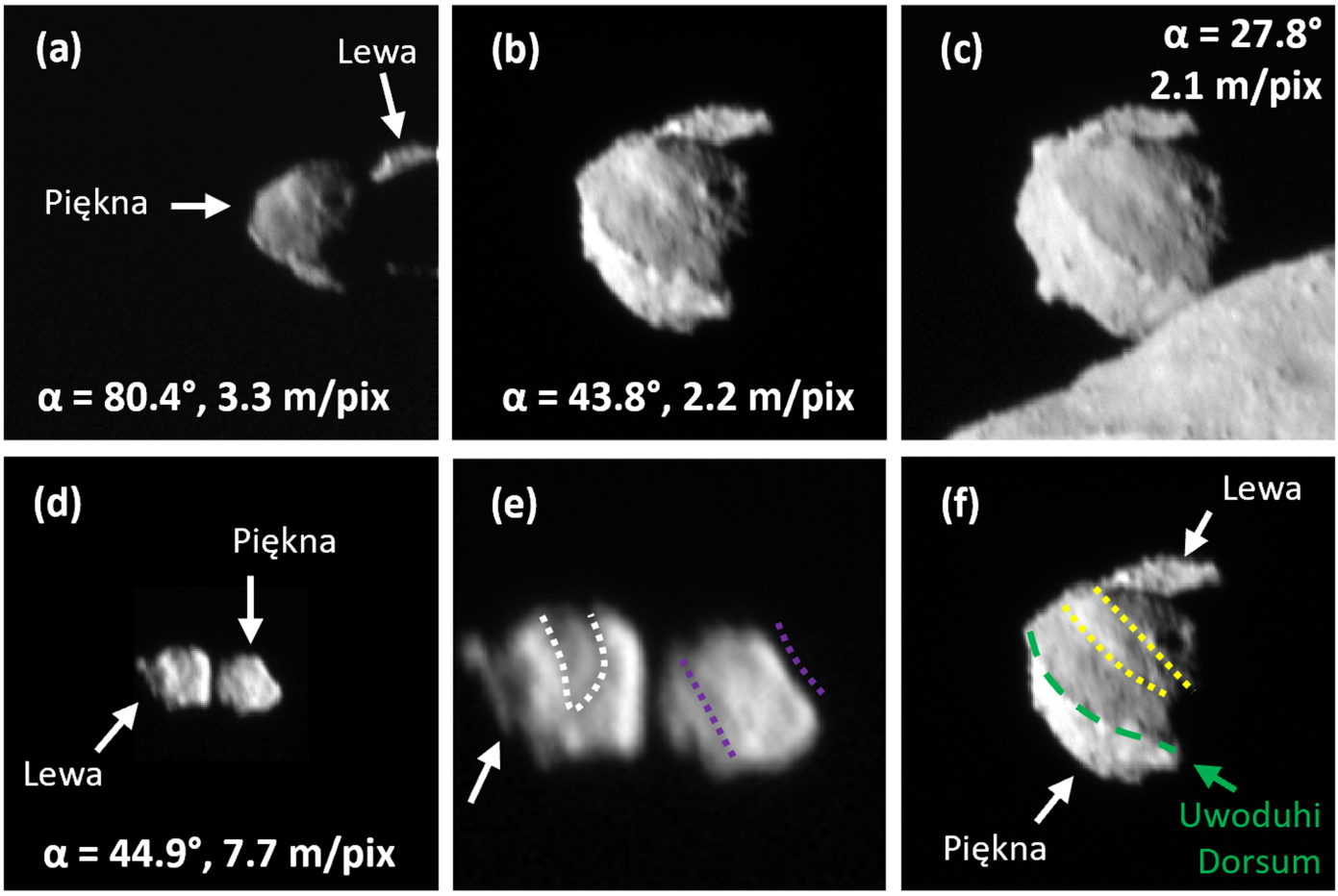

Figure 19. Images of Selam and resolved surface features; north is approximately up in all images. (a) Image lor_0752129497_03589, taken during approach. Arrows identify Piękna Lobus and Lewa Lobus. Piękna Lobus is closest to Dinkinesh, which is to the left in this view. Lewa Lobus is almost completely shadowed by Piękna. (b) Portion of image lor_0752129590_03608. In this view Piękna Lobus is in the foreground and Lewa Lobus is in the background. (c) Portion of image lor_0752129617_03613, which is one of the last views of Selam before Selam leaves the L'LORRI FOV for a time around closest approach. The yellow arrows point to a broadening of the base of Uwoduhi Dorsum. The object in the lower right corner of this panel is Dinkinesh. (d) Portion of image lor_0752129947_03679, which is the first image after closest approach that fully contains Selam. (A short series of earlier images contain partial views of Selam.) Arrows identify Piękna Lobus and Lewa Lobus to clarify that the viewing geometry is "from the other side" compared with panel (a); in this view Dinkinesh is to the right. (e) A zoom-in of Selam from panel (d). Dotted purple lines note aspects of Piękna Lobus: the right-hand profile of Piękna is nearly planar, though slightly concave; near the contact with Lewa there is a linear feature. A white dotted "V"-shaped depression occupies roughly the middle third of Lewa Lobus. The white arrow points to a thin, approximately linear feature that marks the end of Lewa Lobus. This feature is approximately parallel to the Dinkinesh-facing edge of Piękna. (f) The same as panel (b), but with additional annotation. The green dashed line marks Uwoduhi Dorsum. The yellow dotted lines identify linear features on Piękna.

the rollover diameter. However, restricting the Dinkinesh craters to a more conservative subset increases the slope.

Ultimately, we can make one robust conclusion for Dinkinesh, which is consistent with crater SFDs on other asteroids: regardless of the fit selected, the crater SFD is shallower than what would be predicted given that the small impactors follow a Dohnanyi-like power law with cumulative slope ~ -2.6 (e.g., W. F. Bottke et al. 2020). We consider possible explanations for a shallow crater SFD that are relevant to the specifics of the Lucy data for Dinkinesh, as well as additional processes that should apply to both NEAs and MBAs.

The first effect is specific to the flyby nature of Lucy, namely, the changing phase angle and resolution across the illuminated surface of Dinkinesh (Figure 2) is such that craters near the completeness limit were not observed as well on the departure hemisphere as on the approach hemisphere. All but one of the category 1 craters is visible in the approach hemisphere, and all of the smallest craters and most of the craters in general appear in the approach hemisphere (Figure 4(a)). Only six craters across all categories are visible in the departure hemisphere.

Second is the potential for impact armoring (E. Tatsumi & S. Sugita 2018; E. B. Bierhaus et al. 2022), which can either prevent a crater from forming or reduce the crater size relative to a traditional strength scaling law. If the projectile impact energy is less than the target disruption energy of the surface boulder(s), no crater will form in the bulk surface, although a small crater may form on a boulder (e.g., R. L. Ballouz et al. 2020). If the impact energy exceeds the target boulder disruption energy, a crater may form, though its diameter will be smaller than predicted by a strength scaling law. In addition, this reduction is size dependent, meaning that smaller sizes experience a greater effect. This results in a shallowing of the SFD even at diameters larger than the "rollover" diameter that corresponds to a rapid decrease in crater density due to armoring. The SFD shallowing is sensitive to details related to the impactor SFD, boulder SFD, and material properties and thus will change between asteroids. Thus, even if the Lucy data are insufficient to observe the rollover diameter, the smallest sizes may still be affected by impact armoring.

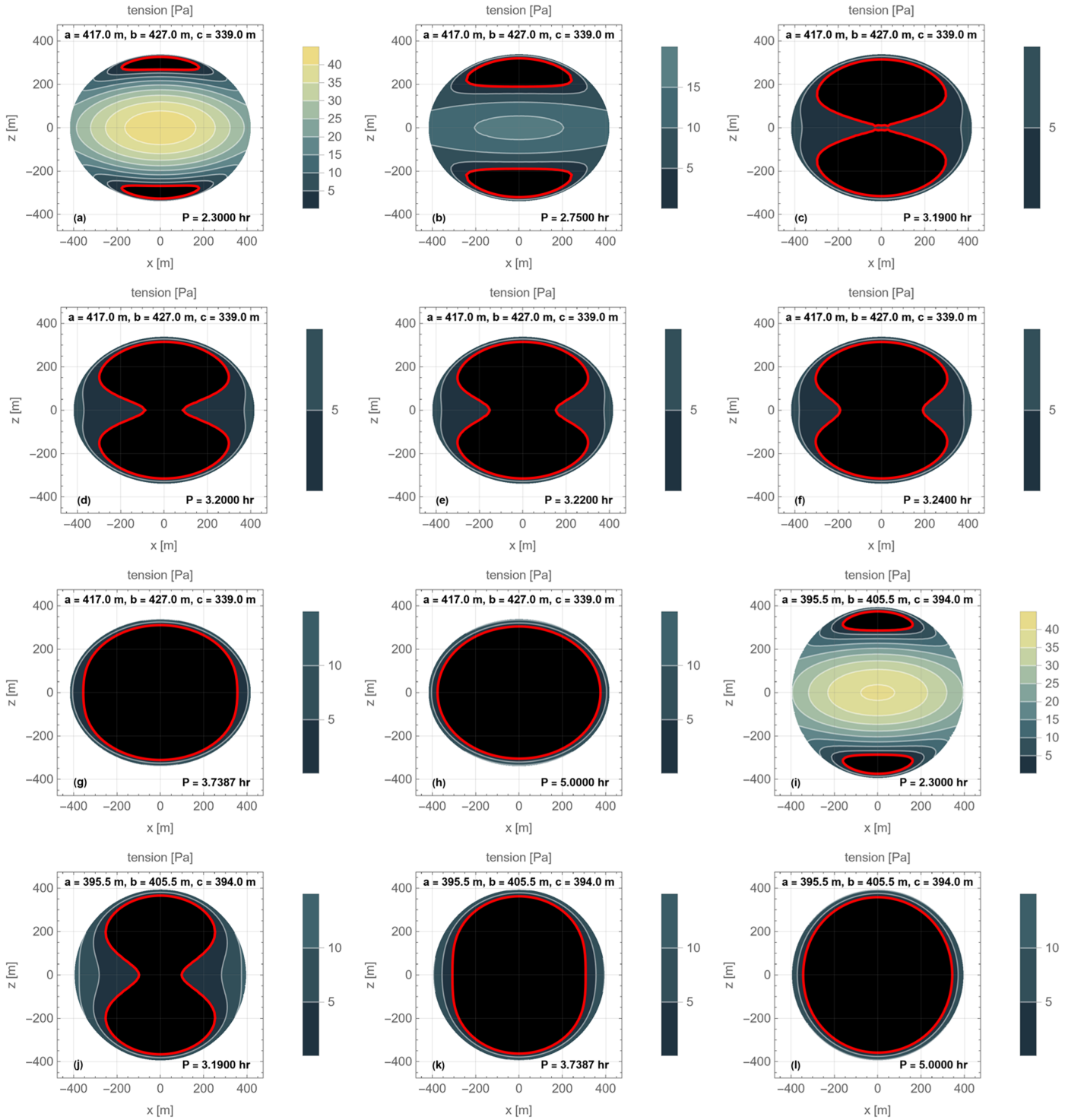

Figure 20. Dinkinesh interior strengths needed to prevent rotational failure for different rotation periods and body dimensions. The plot legends are in Pa. Note that these values reflect stresses created by rotation and are not the interior strength distribution. Panel labels are in the lower left corner. Panels (a)–(h) use the current body dimensions for Dinkinesh. Panels (i)–(l) use a hypothetical shape that has smaller equatorial dimensions and a larger vertical dimension, which simulates a potential configuration prior to mass shedding and flattening from YORP failure. The current Dinkinesh spin period is 3.7387 hr, panels (g) and (k). The red contour represents the 0 Pa boundary; inside the red contour, though, the body does not require any strength to maintain its shape at that spin rate.

Third is the effect of processes that could preferentially remove small craters. For example, downslope movement of surficial regolith could preferentially remove small craters on each of the asteroids. Dinkinesh has a satellite, and a likely formation mechanism for the satellite is mass wasting from Dinkinesh itself. Similarly, models of seismic shaking from impacts (e.g., J. Richardson et al. 2020) suggest that later impacts can erode earlier generations of craters because of the seismic waves that propagate through the asteroid. However, observations from the Hayabusa2 impact experiment (G. Nishiyama et al. 2021) suggest that seismic shaking is a local effect and may not be sufficiently effective at global scales to suppress the crater SFD.

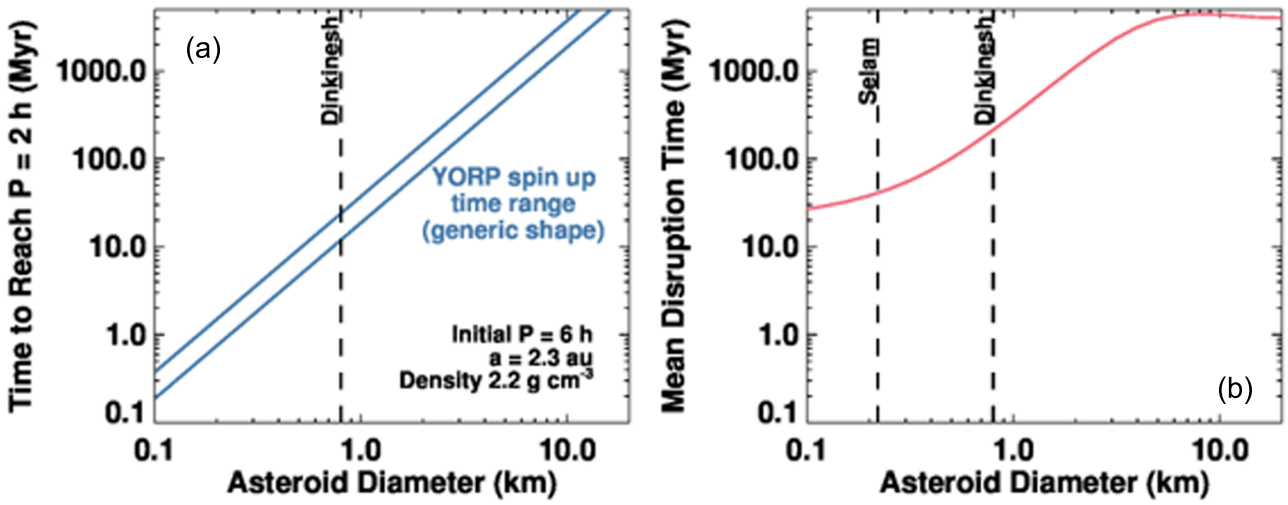

Figure 21. YORP spin-up and collisional timescales. (a) The two blue curves correspond to the minimum and maximum YORP spin-up time for asteroids with the same bulk density and semimajor axis as Dinkinesh. (b) The red curve is the estimated asteroid collisional lifetime in the main belt, as a function of diameter. The collisional lifetime for Dinkinesh is ∼10 times greater than the YORP spin-up time, consistent with the expectation that Dinkinesh has had time to spin up to failure at least once, and potentially several times.

Alternatively, some combination of all of these processes interact to produce the measured SFD. While the values we report for Dinkinesh are not necessarily unexpected (because of shallow crater SFDs observed on other asteroids) and may be consistent with a value derived from a higher-resolution dataset, we caution that asymmetric viewing geometry between the hemispheres results in different quality of surface evaluation.

7.2. Boulder SFD Comparison with Other Asteroids

We briefly consider the Dinkinesh boulder population in the context of other asteroids (Table 5), including multiple S-class asteroids (Itokawa, Eros, Toutatis, Dimorphos) and two in the C complex (Bennu and Ryugu). Because we do not have boulder datasets available for multiple bodies, we do not repeat a recalculation of SFDs for boulders in the way that we did for craters. The asteroid size scale spans from Dimorphos at ∼175 m to Eros at ∼34 km (longest dimension). There is no systematic trend in SFD exponent as a function of size; however, there is evidence for a difference between the S-class and C-complex asteroids. With the exception of Dimorphos, the S-class asteroids have exponents steeper than (i.e., less than) −3, whereas the two C-complex asteroids have an exponent around −2.5. (The difference remains even after applying error bars.)

We compare the maximum boulder size relative to body dimensions (Table 6; Figure 22). Because there are only eight objects, we cannot draw definitive conclusions; however, based on the data that exist, we note two trends: (1) for all asteroids the maximum boulder size is proportionally smaller as asteroid size increases, and (2) for asteroids less than 1 km the maximum boulder size on Dinkinesh has the smallest value relative to the host body dimension.

7.3. Long-term History

First, we consider collisional evolution. From the end of the instability that changed the orbital configuration of the giant planets (e.g., see review in D. Nesvorný et al. 2018), presumably a few tens of Myr or so after the formation of the first solids (D. Nesvorný et al. 2018; W. Bottke et al. 2023) onward, the main-belt evolution has been dominated by impacts from other MBAs and the consequences of non-gravitational forces, the latter of which mainly affect the evolution of asteroids smaller than a few tens of kilometers. These impacts can cause cratering events or, in some cases, disruption events (e.g., W. F. Bottke et al. 2015). Using the collisional evolution model of W. F. Bottke et al. (2020), we find that a typical asteroid with the same diameter as Dinkinesh (i.e., 738 m in diameter) can be catastrophically disrupted (when the largest remnant after the collision is less than half the mass of the pre-impact mass) by an impacting asteroid that is 14 m in diameter striking at 5 km s^{-1}. Using the main-belt SFD from by W. F. Bottke et al. (2020), we find that the cumulative number of these objects in the main belt is 9.4×10^9. Next, using the collision probability code and methods discussed in W. F. Bottke et al. (1994), we find that the intrinsic collision probability of Dinkinesh against main-belt objects on its current orbit is 2.6×10^{-18} km^{-2} yr^{-1}. Taken together, we estimate a mean collisional lifetime for Dinkinesh of 270 Myr. This age is considerably shorter than the age of the solar system. This could mean that Dinkinesh is a first-generation rubble-pile by-product of the catastrophic disruption of a larger body that occurred less than one Dinkinesh collisional lifetime in the past. Alternatively, Dinkinesh might be a second- or later-generation remnant of an even larger body that experienced one or more disruption events within the inner main belt (K. J. Walsh et al. 2024).

Dinkinesh more frequently experiences global resurfacing events from subcatastrophic impacts (which is based on the expectation that global resurfacing events from impacts that do not disrupt the asteroid are caused by smaller, and therefore more frequent, impactors than objects that disrupt Dinkinesh). The projectile size needed to produce a surface reset event has yet to be quantified with models or observational data, but the projectile size needed to produce global resurfacing is probably smaller than 14 m. This implies that the craters on the surface of Dinkinesh may not go back in time to the last disruption event or initial formation, but instead to the last resurfacing event.

Table 4
Crater SFDs for Dinkinesh and Similarly Sized Asteroids

Crater Population for SFD Fit	Asteroid	NEA or MBA	Crater Population in Fit	Minimum Diameter (m)	Maximum Diameter (m)	No. of Craters in Fit	Cumulative SFD Exponent	Notes
Crater SFDs with real rollovers	Itokawa	NEA	All craters	2	163	38	0.55 ± 0.03	Data from N. Hirata et al. (2009); we calculated the fit
			Diameters larger than the rollover	21	163	23	1.09 ± 0.11	Data from N. Hirata et al. (2009); we calculated the fit
	Bennu	NEA	Diameters larger than the rollover and smaller than the slope change	3	20	904	1.35 ± 0.01	Data from E. B. Bierhaus et al. (2022); we calculated the fit
			Diameters larger than the rollover	3	215	984	1.34 ± 0.01	Data from E. B. Bierhaus et al. (2022); we calculated the fit. The most abundant small craters dominate the fit, which is why the resulting value is similar to the one derived for craters between 3 and 20 m.
			Diameters larger than the rollover and slope change	20	215	80	1.24 ± 0.03	Data from E. B. Bierhaus et al. (2022); we calculated the fit
Crater SFDs with a change in slope	Ryugu	NEA	All craters	10	290	86	0.84 ± 0.02	Data from N. Hirata et al. (2020); we calculated the fit
			Diameters smaller than the slope change	10	40	39	0.39 ± 0.05	Data from N. Hirata et al. (2020); we calculated the fit
			Diameters larger than the slope change	40	290	47	1.46 ± 0.08	Data from N. Hirata et al. (2020); we calculated the fit
	Dinkinesh	MBA	All craters from all categories	17	232	29	1.09 ± 0.09	This paper
			Diameters smaller than the slope change from all categories	17	60	19	0.78 ± 0.15	This paper
			Diameters larger than the slope change from all categories	60	232	10	1.85 ± 0.57	This paper
			Category 1 craters above the completeness limit	60	213	4	1.60 ± 2.60	This paper
Comparison of the most similar subsets from each asteroid, selected from the entries above. In the case of asteroids with a real rollover (Itokawa, Bennu), these are diameters larger than the rollover. In the cases of asteroids with a slope change (Ryugu, Dinkinesh), these are diameters larger than the slope change.								
Crater SFDs with real rollovers	Itokawa	NEA	Diameters larger than the rollover	21	163	23	1.09 ± 0.11	As above
	Bennu		Diameters larger than the rollover	3	215	984	1.34 ± 0.01	
	Bennu		Diameters larger than the rollover and slope change	20	215	80	1.24 ± 0.03	
Crater SFDs with a change in slope	Ryugu	NEA	Diameters larger than the slope change	40	290	47	1.46 ± 0.08	
	Dinkinesh	MBA	Diameters larger than the slope change from all categories	60	232	10	1.85 ± 0.57	
			Category 1 craters above the completeness limit	60	213	4	1.60 ± 2.60	

Note. The first section lists fits for different selections of crater diameters. The second section selects from that list to provide a comparison of a subset of the fits that are SFDs derived from using consistent decisions for the selected diameter range of the fit.

Table 5
Boulder Populations on Asteroids

Asteroid	Spectral Class	Dimensions	Cumulative SFD Exponent	SFD Reference
Bennu	B	∼500 m diameter	−2.5 ± 0.1	K. N. Burke et al. (2021)
Ryugu	C	∼900 m diameter	−2.65 ± 0.05	T. Michikami et al. (2019)
Itokawa	S	∼535 × 294 m	−3.6 ± 0.3	I. DeSouza et al. (2015)
Itokawa	S	∼535 × 294 m	−3.52 ± 0.20	S. Mazrouei et al. (2014)
Itokawa	S	∼535 × 294 m	−3.34 ± 0.19	T. Michikami et al. (2008)
Itokawa	S	∼535 × 294 m	−3.05 ± 0.14	T. Michikami & A. Hagermann (2021)
Eros	S	∼34 × 11 km	−3.28 ± 0.15	A. J. Dombard et al. (2010)
Eros	S	∼34 × 11 km	−3.25 ± 0.14	T. Michikami & A. Hagermann (2021)
Toutatis	S	∼4.6 × 2.3 km	−4.4 ± 0.1	Y. Jiang et al. (2015)
Dimorphos	S	∼177 × 174 × 116 m	−2.5 ± 0.2	M. Pajola et al. (2024)
Didymos	S	∼850 × 620 m	−3.6 ± 0.7	M. Pajola et al. (2024)
Dinkinesh	S	910 × 870 × 716 m	−3.93 ± 0.15	This paper

Table 6
Asteroid and Maximum Boulder Sizes for Spacecraft Encounters Whose Data Have Sufficient Resolution to Identify Surface Boulders

Asteroid	Geometric Mean Diameter (m)	Maximum Boulder Size (m)	Boulder Size, % of Geometric Mean
Ryugu	959[c]	140[d]	14.6
Bennu	485[a]	95[b]	19.6
Eros	16,280[e]	100[f]	0.6
Toutatis	2710[g]	61[h]	2.2
Dinkinesh	828	53	6.5
Didymos	736[i]	93[j]	12.6
Itokawa	320[k]	50[l]	15.6
Dimorphos	153[m]	16[j]	10.5

Note. The footnotes for each entry indicate the source reference for the data; in all cases the references report three dimensions for an asteroid ($a > b > c$); here we use the geometric mean: $(a\ b\ c)^{1/3}$. The Dinkinesh data are from our work reported in this paper. Bennu and Ryugu are C-complex asteroids; the remaining objects are S-class asteroids. The entries are sorted first by spectral type and then by size. Note that, like Dinkinesh, the maximum boulder sizes for Toutatis, Didymos, and Dimorphos are from the hemisphere observed during the encounter and thus might be underestimates.
[a] M. G. Daly et al. (2020).
[b] K. N. Burke et al. (2021).
[c] S. Watanabe et al. (2019).
[d] T. Michikami et al. (2019).
[e] A. J. Dombard et al. (2010).
[f] A. J. Dombard et al. (2010).
[g] J. Huang et al. (2013).
[h] Y. Jiang et al. (2015).
[i] O. S. Barnouin et al. (2024).
[j] M. Pajola et al. (2024).
[k] T. Michikami et al. (2019).
[l] T. Michikami et al. (2019).
[m] R. T. Daly et al. (2023).

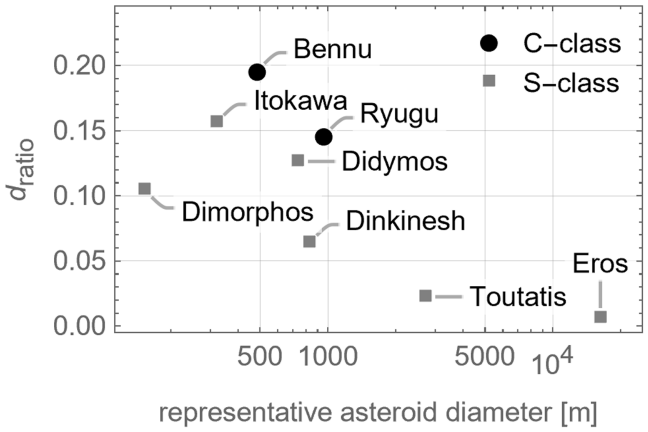

Figure 22. Maximum boulder sizes vs. representative asteroid diameter: d_{ratio} is the maximum boulder size on an asteroid normalized by a representative asteroid diameter. This plot uses the values from Table 6.

Given that the current obliquity of Dinkinesh is near 180°, we can assume that it has been strongly affected by YORP thermal torques over its recent history. Moreover, this obliquity implies that Dinkinesh has been drifting inward (due to retrograde spin) toward the Sun over its recent history. For a 738 m average diameter of Dinkinesh, we use Figure 2 in W. F. Bottke et al. (2006) to predict that its Yarkovsky semimajor axis drift rate is $da/dt \sim (1\text{–}2) \times 10^{-4}$ au Myr^{-1}. Assuming that its collisional lifetime is on the order of 270 Myr, we estimate that Dinkinesh has moved 0.027–0.054 au toward the Sun by the Yarkovsky effect since its last disruption event, or initial formation.

Dinkinesh's proper semimajor axis, eccentricity, and inclination (a, e, i) are (2.°191, 0.°1479, 1.°23), which places it in the innermost region of the inner main belt, typically defined as asteroids having <2.5 au. The closest prominent S-type asteroid families that could have conceivably produced Dinkinesh are Euterpe and Flora (D. Nesvorný et al. 2015). The Euterpe family can probably be ruled out as a candidate family: while its family members have a low proper inclination like Dinkinesh, the closest Dinkinesh-sized bodies are near 2.3 au, nearly 0.11 au away.

The Flora family is modestly more promising. The starting locations of the Flora family fragments had proper (a, e, i) of approximately (2.2 au, 0.°15, and 5.°7) but have spread over the past billion years or so throughout the inner main-belt region (D. Vokrouhlický et al. 2017). An examination of the runs from D. Vokrouhlický et al. (2017) indicates that none of their kilometer-sized test Flora family members reached the current orbit of Dinkinesh over the age of the family. With that said, some did come close enough to suggest a possible link to the Flora family (see Figures 8 and 10 in D. Vokrouhlický et al. 2017). Until a more in-depth, higher-resolution investigation of possible sources for Dinkinesh occurs, we cannot argue for a preferred source asteroid family.

7.4. Recent History

As noted in Section 6, the material characteristics of an asteroid (or other small body) affect the response to YORP

Table 7
YORP Failure Model Outcomes for Rubble-pile Asteroids Compared with Dinkinesh Observations

Volumetric Strength	Response to YORP Stresses	Consistent with Dinkinesh–Selam?
Homogeneous, weak	Increased flattening of primary (lower c/a axis ratio, P. Sánchez & D. J. Scheeres 2016, 2017).	No. Dinkinesh axis ratio c/a 0.79.
Homogeneous, strong	Initial failure occurs in body interior (M. Hirabayashi 2015, 2020; Y. Zhang et al. 2022). Failure results in multiple components (M. Hirabayashi 2015).	Possibly. Fragment sizes after failure for strong object may be inconsistent with Dinkinesh–Selam mass ratio.
Strong interior, weak surface	Initial failure occurs in surface; if spin rate continues to increase, then interior will fail (e.g., strong interior case above). Core is 3–4 times stronger than surface (P. Sánchez & D. J. Scheeres 2017).	Yes. Weak surface failure provides mass for Selam and Fab, and consistent with more recent mass wasting. (If Selam and Fab are formed from the same initial disk, Selam must also be largely <12 m blocks.) Strong interior could explain Sumak Fossa.
Weak interior, strong surface	Internal failure causes body to deform into oblong and potentially irregular shape; also, strong surface can prevent significant fissioning.	No. Bulk shape of Dinkinesh inconsistent with this structure.
Small core, weak or strong	increased flattening of primary (lower c/a axis ratio; P. Sánchez & D. J. Scheeres 2017).	No. The Dinkinesh c/a axis ratio of ∼0.79 likely is too high to be consistent with this structure.
Large, weak core	Oblate spheroid, no obvious volumetric failure (P. Sánchez & D. J. Scheeres 2017)	No. Sumak Fossa likely is diagnostic of volumetric failure.
Large, intermediate or strong core	Asymmetric volumetric failure (intermediate strength) or more symmetric volumetric failure (strong)	Yes. Sumak Fossa bounds volumetric extensional failure. Additional volumetric failure on opposite hemisphere is a possibility.

Note. The models with a "strong" core and "weaker" overlying shell are the most consistent with Dinkinesh. Note that a "strong" core still has a low absolute strength value, typically less than a few hundred Pa.

spin-up. Different model types (e.g., K. A. Holsapple 2010; M. Hirabayashi & D. J. Scheeres 2015; D. J. Scheeres 2015; P. Sánchez & D. J. Scheeres 2016, 2017; R. Nakano & M. Hirabayashi 2020; Y. Zhang et al. 2022) have converged on consistent predictions of the bulk shape response for an approximately homogeneous body. For a weak body experiencing increasing spin rates the shape first deforms by a decrease in the polar axis and expansion in the equatorial regions. The initial failure mode in response to faster spin rates is surface failure; this surface failure can range from local slope collapse, to material buildup at the equator, to mass shedding. For a stronger body the interior is most sensitive to failure, with a decrease in the polar axis and an expansion of the equatorial regions; here, too, the details affect the magnitude of this shape change and whether there is material shedding. Although both the weak and strong bodies cause polar flattening, a potentially distinguishing characteristic between the two is that the weak body experiences more polar flattening (e.g., K. A. Holsapple 2010; P. Sánchez & D. J. Scheeres 2016). More complex behavior arises when considering a layered body, either a weak surface (shell) overlying a stronger interior or vice versa (M. Hirabayashi 2015; P. Sánchez & D. J. Scheeres 2017; M. Hirabayashi et al. 2020).

Though the complete parameter space of strength values, layering, friction angles, porosity, particle shapes, and SFD spans far beyond the analysis regime of existing models, there nevertheless are some key diagnostic features from the existing models that we use to constrain the structure of Dinkinesh and Selam (Table 7). We first rule out the strengthless or weak homogeneous bodies, as well as the case of a stronger shell over a weaker interior. These shapes are either too flattened (like Dimorphos; O. S. Barnouin et al. 2024) or too irregular. The case of a strengthless body in particular is further ruled out by the global shape of Dinkinesh: in the limit of a truly strengthless body in rotation, the body shape will deform into Maclaurin or Jacobi shapes (see, e.g., K. A. Holsapple 2001, 2004, and 2010, for discussion), which is not the case for Dinkinesh.

For the multilayer cases we consider the results of P. Sánchez & D. J. Scheeres (2017): their Figure 10 shows cross sections of simulations that vary with the size and strength of the central volume and the corresponding size of the outer shell. We use "core" here for the interior volume to be consistent with their terminology, though we note that this use of "core" is different from a traditional planetary core. The cases that are most consistent with Dinkinesh are the large core, with either an intermediate or high (in a relative sense) strength. They considered two core sizes: a small core that is half the body radius, and a large core that is 0.7 the body radius. The small cores, for the range of strengths considered, result in flattened bulk shapes, which is inconsistent with Dinkinesh. The weakest large core results in an approximately oblate spheroid without a distinct volumetric extension resulting from failure, which is also inconsistent with Dinkinesh. The intermediate-strength and strong large-core cases prevent excessive flattening of the body shape and result in volumetric failures that are similar to the volumetric wedge bounded by Sumak Fossa. The intermediate-strength case results in a single failure, whereas the strongest core case results in more symmetric shape with failures on either side of the body. Although Lucy did not observe the entire body of Dinkinesh, the depression observed during departure, which might be part of a Sumak-style feature, suggests that approximately symmetrical extensional failure is a possible outcome for Dinkinesh (Figures 18(d) and (e)). A similar feature set is Ryugu's Tokoyo and Horai Fossae (M. Hirabayashi et al. 2019).

To evaluate the structural features on Dinkinesh relative to YORP, we compared the 3D locations of Sumak Fossa, Bella Dorsum, and Indah Fossa relative to the body axes. For each feature we made point measurements in SBMT to trace the feature along its visible extent. For each set of points we used singular value decomposition to derive a best-fit plane, which we plot against the shape model (Figure 23).

In the case of Sumak Fossa, we divided our measurements into north and south. The planar fits to north and south Sumak

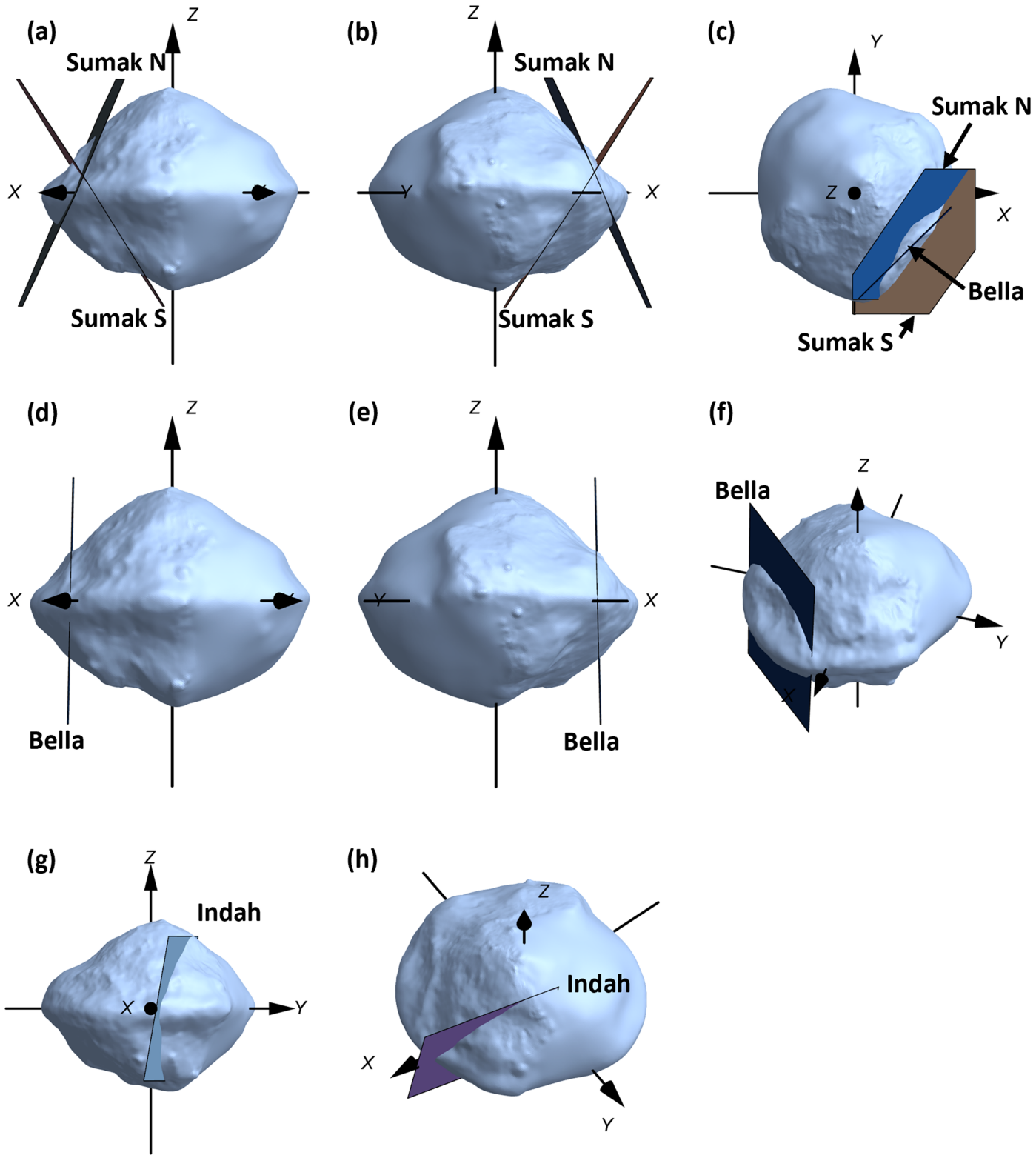

Figure 23. Plane fits to Dinkinesh structural features. (a) Separate fits to the northern and southern portions of Sumak Fossa, with Dinkinesh rendered at $+45°$ in the (x, y)-plane, a view seen during approach. (b) The same as in panel (a), except rendered at $-45°$ in the (x, y)-plane, a view seen during departure. (c) A view from above the north pole showing the plane fits for Sumak north and south, as well as the plane fit for Bella Dorsum. From this perspective the Bella Dorsum plane essentially appears as a line. The planes for north and south Sumak are cropped to keep all elements visible. (d) The Bella Dorsum plane fit alone, rendered at $+45°$ in the (x, y)-plane. This illustrates that the plane of the feature is aligned at 45° to the (x, y) axes and is nearly parallel to the z-axis. (e) The Bella Dorsum plane fit, rendered at $-45°$ in the (x, y)-plane. (f) Perspective view of Bella Dorsum illustrating the planar north–south symmetry of the feature. (g) View of the plane fit to Indah Fossa from the $+x$-axis. (h) Perspective view of the fit in panel (g).

form an "X" shape (Figures 23(a)–(c)), similar to the shape of internal deformations predicted by YORP failure models when the equatorial regions extend outward and polar regions push inward (Figure 20). We specifically compare the location of the best-fit Sumak planes where they cross the equator and the mid-/high-latitude exit points at the surface. This is consistent with the hourglass contours in Figure 20 that occur for rotation periods >3.2 hr, especially those with a broader equatorial waist and where the 0 Pa contour approaches the surface at a higher latitude. (Recall that we use the 0 Pa contour as a useful tracer; the same behavior occurs for small positive contours.) Failure at higher rotation rates is constrained to the deep interior and would not form a volumetric wedge like the region bounded by Sumak Fossa. From this comparison we conclude that the geometry of the failed region bounded by Sumak Fossa constrains the rotation rate at which failure occurred. While the idealized stress model does not provide a precise constraint (and because there is a rapid evolution of the stress contours starting around 3.2 hr), the consistency between two shapes examined (Figure 20) indicates that the evolution of the hourglass stress contours is a general result for plausible pre-failure Dinkinesh body dimensions. This is similar to the Hirabayashi et al. conclusion that Ryugu's Tokoyo and Horai Fossae are structural failures, creating relaxed regions.

Bella Fossa is nearly parallel with the Dinkinesh z-axis and nearly 45° from the x- and y-axes. This direction is aligned with the longest body dimension, consistent with the failure driving an increase in body dimension that increases the moment of inertia, while decreasing spin rate (e.g., K. A. Holsapple 2010), thereby transitioning the body—at least temporarily—to a relaxed state. There is a slight rotation in the (x, y)-plane orientation between Sumak and Bella, with Sumak rotated counterclockwise, i.e., in the spin direction, relative to Bella Fossa. While we cannot identify the relative age of Sumak relative to Bella—indeed, they may be contemporaneous—an offset in their orientations relative to the (x, y)-plane is a constraint that future models should consider.

As noted earlier, the southern portion of Indah Fossa is superimposed over Sumak Fossa; however, when Indah crosses over Fab Dorsum into the northern hemisphere, it follows a path separate from Sumak Fossa. Because the geometry prevents us from assessing whether the feature continues to the other side of the body, the plane fit is less constrained than the other features (i.e., the fit is to a single trace on one hemisphere vs. over a full-body cross section). The plane fit to the observed feature crosses the body at an angle to the x-axis, which we extrapolate to the hemisphere not seen during the Lucy flyby (though the hemisphere is dimensionally constrained via light curves; see the Dinkinesh shape model description in F. Preusker et al. 2024, with brief discussion in Section 2 of this paper). Given that the region bounded by (interior to) Sumak Fossa is relaxed, stress buildup in response to the relentless YORP acceleration would be concentrated in other parts of the body (e.g., M. Hirabayashi et al. 2020), which is consistent with the location of Indah Fossa.

The collective evidence of (i) the Dinkinesh global top shape, (ii) the major geologic features of Sumak Fossa and Fab Dorsum, and (iii) the contact binary nature of Selam supports the conclusion of H. F. Levison et al. (2024) that Dinkinesh suffered one or more YORP failures that caused adjustment of the Dinkinesh shape, created Sumak Fossa and Fab Dorsum, and created Selam. In this hypothesis Sumak Fossa is a structural failure of Dinkinesh in response to YORP spin-up, and the disk of shed material was the source material for both Selam and Fab Dorsum. Although the spin rate of Dinkinesh slowed during those events, the presence of Indah Fossa and other mass-wasting events suggests that the surface and near-surface regions continue to respond to rotationally caused stress. This is consistent with the location of stress as a function of spin rate: as seen in Figure 20, at longer spin periods, the surface and near-surface regions are the only volumes that require positive cohesive strengths to resist failure.

Support for satellite formation from mass shedding also comes from recent simulations. R. Hyodo & K. Sugiura (2022) simulated a hypothetical asteroid shedding material from YORP spin-up and tracked the evolution of the shed material. They found that the disk mass can be sufficient to generate spiral-arm structures, which simultaneously move material outside the Roche limit and spread the inner edge of the disk toward the primary. The disk mass transported beyond the Roche lobe accumulated to form one or more moons, and material from the inner edge of the disk preferentially reaccreted in the primary equatorial region, resulting in an equatorial ridge. Their simulations can form multiple moons.

We tie together the YORP-driven nature of the system and system timescales first by comparing between the volumes in Selam and Fab Dorsum and the equivalent regolith depth on Dinkinesh. Adopting the volumes for Fab Dorsum and Selam derived earlier, their cumulative volume is $\sim 4.1 \times 10^7$ m^3. If that volume were spread uniformly over the 1.83 km^2 surface area of Dinkinesh, the material would form a layer ~22 m thick, which is sufficient to cover all existing craters. Additional volume from mass lost from the system during a mass-shedding event, redistributed over the surface, further blankets existing surface features. While the lost mass was not a regolith layer of uniform thickness over Dinkinesh, only ~10 m of regolith is sufficient to cover the current Dinkinesh craters (Figure 7). Thus, we postulate that most, or perhaps even all, craters seen in the Lucy images postdate the YORP failure that formed Sumak Fossa.

Combining the observations of surface features and their superposition relations with estimates of impact cratering and solar-radiation-driven Yarkovsky and YORP, we develop a relative chronology for the Dinkinesh–Selam system (Figure 24). We define T_0 as the time of most recent YORP-driven failure of the body. Prior to that time and since that time, both impact cratering and YORP have been ongoing processes that modify the surface and the spin rate. Intriguing features that may also be coincident, or happen at different times, include the large depression seen during Lucy departure (Figures 18(d) and (e)) and Bella Fossa. If the result of YORP-driven failure, the depression could be part of a Sumak-like feature on the opposite hemisphere that represents a symmetrical failure, or it could represent a distinct YORP failure event. If Bella Fossa is structurally intertwined with Sumak Fossa, then Bella also occurred during the same failure event. (Because we interpret Bella as a class of feature not yet seen on an asteroid, we caution that there could be other explanations for this feature; we provide brief, additional discussion below.) We adopt the disk formed by mass shedding as the explanation for Fab Dorsum and the formation of Selam. The R. Hyodo & K. Sugiura (2022) simulations find that moons and the equatorial ridge can form from the disk in

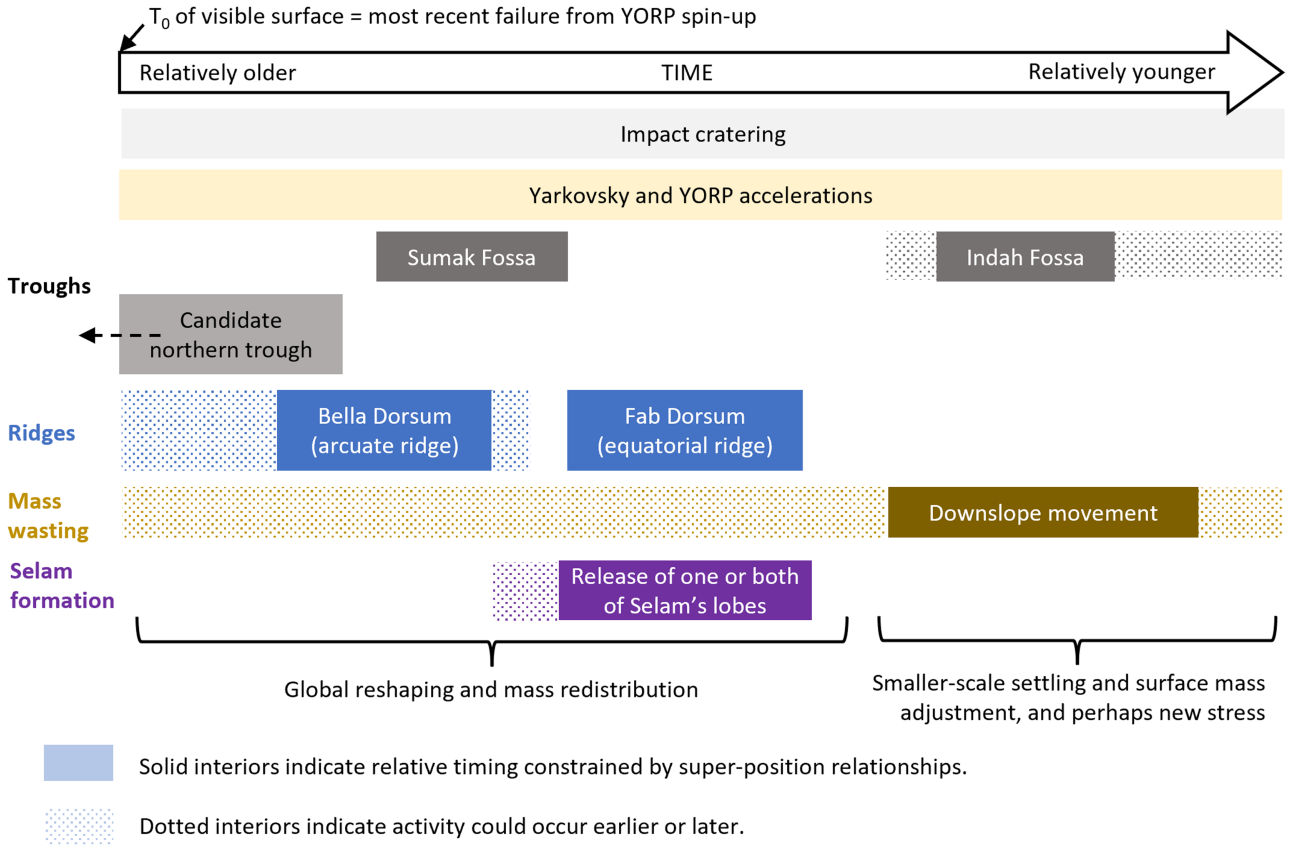

Figure 24. The time history of processes on Dinkinesh. We define T_0 as the last major resetting event of the surface, likely YORP-driven failure that created Sumak Fossa and Fab Dorsum (and one or both lobes of Selam). Since that time, both Yarkovsky and YORP have acted continuously, affecting the semimajor axis evolution and body rotation. Though not continuous, impact cratering also spans from T_0 to the current day. Bella Dorsum may be concurrent with the most recent YORP failure that created Sumak and Fab, or it may predate that time. Fab Dorsum superimposes Sumak Fossa, though it may have formed from the same YORP failure; thus, we tie the start of Fab to the end of Sumak. After the global restructuring from YORP failure, the surface includes evidence for more recent but smaller-scale activity: Indah Fossa, and possible cases of mass wasting from geopotential highs.

Table 8
Estimated Timescales for the Dinkinesh–Selam System

Process	Age/Duration (Myr)	Notes
Dinkinesh crater-based age, maximum	650	10^5 Pa cratering strength, craters $>$ 45 m
Dinkinesh crater-based age, intermediate	10	10^3 Pa cratering strength, craters $>$ 45 m
Dinkinesh crater-based age, intermediate	1	10 Pa cratering strength, craters $>$ 45 m
Dinkinesh crater-based age, minimum	0.9	Gravity scaling, craters $>$ 45 m
Selam crater-based age, minimum	0.16	Gravity scaling
Dinkinesh collisional lifetime	270	738 m avg diameter MBA
YORP spin-up to disruption	10–20	Derived from D. Čapek & D. Vokrouhlický (2004)
Yarkovsky-driven semimajor axis drift	(1–2) $\times$ 10^{-4} au Myr^{-1}	

~700 hr, or only ~29 days; H. F. Agrusa et al. (2024) simulations form asteroid satellites from a debris disk in just a few days. Even if there are large uncertainties and/or variation possible from different input parameters, these timescales are very short compared to geologic timescales. Since T_0, ongoing YORP acceleration likely built up additional body stress that created Indah Fossa. In addition, rotational acceleration alone, or perhaps in conjunction with impact-induced accelerations, has created ongoing downslope movement from regions with elevated geopotential highs.

Table 8 summarizes the estimated timescales we derived using crater-based surface ages, collisional lifetimes, and YORP spin-up. The maximum crater-based surface age of 650 Myr is more than two times greater than the mean collisional lifetime of 270 Myr; thus, we conclude that the 10^5 Pa strength associated with that value is likely too high. The 10–20 Myr YORP spin-up time is consistent with cratering strengths $<10^3$ Pa.

7.5. The Curious Case of Bella Dorsum

Bella Dorsum is, to our knowledge, the first observation of an arcuate and equatorially symmetric ridge on an asteroid. The morphology of the feature is distinct between the northern and southern hemispheres (e.g., Figure 15). While the northern arc of Bella Dorsum is coincident with one side of Sumak Fossa and thus could be interpreted simply as part of Sumak,

the southern arc of Bella follows a separate path from Sumak Fossa. Thus, we conclude that while the features may be related, they may not have emerged from the same event.

We present two potential hypotheses for Bella's formation: (1) a remnant feature from a previous YORP failure, and (2) a remnant contact binary interface with an object that separated from and eventually escaped Dinkinesh. These hypothetical scenarios are first attempts to provide a framework to connect Bella Dorsum with existing models of binary systems; we encourage future work to consider the viability of these scenarios or propose other origins.

In the first case, S. Tardivel et al. (2018) describe a process that could generate an equatorial cavity from YORP spin-up. Essentially, the irregular dimensions of a rubble pile mean that YORP stresses are asymmetric inside the body, i.e., the symmetric hourglass contours in Figure 20 in reality are asymmetric, with one side of the waist reaching deeper than the other. The equatorial-centered wedge bounded by the deeper contour could fail, and an equatorial cavity will form if material leaves the body. Though Bella Dorsum currently does not bound an equatorial cavity, Bella's location and geometry are consistent with the process described in S. Tardivel et al. (2018).

The second case stems from the potential of multigenerational satellites, or repeated separations and reconnections of a binary pair (e.g., D. J. Scheeres 2007; S. A. Jacobson & D. J. Scheeres 2011). Given that Selam is young relative to Dinkinesh (Selam has a shorter collisional lifetime), Dinkinesh may have had one or more satellites prior to Selam. Binary systems can evolve from separated binaries to contact binaries, or vice versa. Bella Dorsum may be a remnant interface with a contact binary object that separated and ultimately escaped Dinkinesh. In this case Bella Dorsum existed prior to the failure that caused Sumak Fossa. This interface may have introduced mechanical weakening inside Dinkinesh (in addition to making it the location of largest radial extent, and thus the first intersection point between the balance of gravity and centrifugal accelerations), setting up the conditions for mechanical failure. On the other hand, Bella Dorsum would have to survive what otherwise appears to be a resurfacing of Dinkinesh that occurred during the most recent YORP failure.

7.6. Possible Formation Mechanisms for Selam

Selam is the first observed contact binary satellite of an asteroid binary system. Because the Lucy mission selected the Dinkinesh–Selam system owing to accessibility rather than a prior knowledge of system configuration, the law of averages suggests that contact binary satellites are common rather than rare. A complete evaluation of Selam formation models is beyond the scope of this paper; however, because formation and surface geology are inextricably linked, we note some observational constraints that are relevant to any future analysis evaluating Selam's formation, and we briefly note intriguing—though not definitive—similarities with existing published work.

The observational constraints for the formation of Selam include the following: (i) the approximately equal sizes of Piękna Lobus and Lewa Lobus; (ii) the Selam–Dinkinesh mass ratio of $\sim$0.05; (iii) the orbital separation of the bodies of $\sim$8.4 Dinkinesh radii; and (iv) though not well resolved, the potential layering in Selam (Figure 19) is a weak constraint.

While we cannot definitively conclude that Selam formed from the same disk of material (from mass shedding due to YORP failure; e.g., H. F. Agrusa et al. 2024) as Fab Dorsum, adopting that formation model provides the additional constraint that Selam largely consists of individual particles $<$12 m rather than large blocks. This last point follows the same logic for constraining particle sizes in Fab Dorsum (Section 5.1). In addition, if both lobes of Selam are volumetrically dominated by a small number of blocks, that would imply an unusually high number of proportionally large surface blocks on Dinkinesh. Table 6 summarizes the maximum boulder sizes relative to host body size for multiple asteroids. Bennu has the largest boulder proportional to the body diameter at 20%, compared with the 6.7% for the observed surface of Dinkinesh. If the largest surface boulder on Dinkinesh, prior to YORP failure, was 150 m (roughly 20% the size of Dinkinesh), we use the observed boulder SFD to estimate that there would be about four 100 m scale boulders. Collectively, these five boulders would be $\sim$22% of Selam's total volume. To account for a majority of Selam's volume, the pre-failed Dinkinesh would need roughly three times the large surface-boulder density of Bennu. While a high spatial density of large boulders is not impossible, such a configuration has not been observed on any small body to date. Based on comparisons with other rubble piles, and given the assumed origin that Selam formed from the same disk of material that formed Fab, we conclude that the most likely interior structure of Selam consists mostly of particles much smaller than the dimensions of the two lobes.

There are several possible formation mechanisms to make a contact binary, including the following: (i) multiple YORP failures separated in time release individual satellites, two of which merge and remain; (ii) a single, nearly symmetric YORP failure (i.e., on opposite ends of the primary body) releases two satellites that merge; (iii) multiple moons form from a disk of material (R. Hyodo & K. Sugiura 2022; H. F. Agrusa et al. 2024); or (iv) rotational fission of a single secondary breaks a single object into two objects, which then merge (S. A. Jacobson & D. J. Scheeres 2011).

No single model best matches the existing constraints, and additional pathways are possible by combining various scenarios. Currently, our preferred Selam formation model ultimately stems from observations of Dinkinesh: Fab Dorsum clearly is a feature that postdates other major structures on the body (e.g., Sumak Fossa) and appears to be material deposited on the surface rather than forming via internal extension, or mass wasting from higher latitudes. Our preferred explanation is that Fab Dorsum formed from an accumulating disk. There is sufficient dynamical history of disk evolution in many systems (the Earth–Moon system, Saturn's rings, the Pluto–Charon system) to motivate the conclusion that the disk also can form one or more satellites. In the case of a single satellite, Selam could have formed by fission of the original satellite, the components of which reconnected; in the case of a multiple-satellite system, two satellites could have experienced a slow-speed merger to form Selam.

7.7. Summary Comparison of Geologic Properties with Other Asteroids

Dinkinesh provides perhaps the clearest example of YORP failure yet seen. Similarly, Selam is the first resolved contact binary satellite. Clearly, the dataset of binary systems

Table 9
Comparison of Physical Parameters between Asteroids Observed by Spacecraft

Parameters	Comparison
Crater SFDs	Size: similar shallow SFDs on small NEAs and Dinkinesh, steeper SFDs on larger MBAs (Ida, Gaspra)
Crater d/D	Consistent: crater d/D can vary on the same body, but generally low average value across asteroids, with typical $d/D \sim 0.1$
Boulder SFDs	S vs. C: S-class asteroids generally have steeper SFDs than C-complex asteroids
Relative maximum crater diameter	S vs. C: C-complex asteroids generally express a maximum crater dimension that is a larger fraction of the host body dimension. (Here we are considering a crater as a circular feature.)
Relative maximum boulder dimensions	Size: generally the ratio of the maximum boulder size to host body dimension decreases with increasing body size NEA vs. MBA: the two spacecraft observed that MBAs with diameters less than a few kilometers have proportionally smaller maximum boulder sizes than NEAs.
Surface regolith	Size: increasing size (and thus increasing surface gravity) appears to correlate with increasing fine-grained abundance at the surface. This conclusion is supported by direct observation at Itokawa, Ryugu, and Bennu (smaller objects) and direct observation at Eros (intermediate scale) and inferred by the photometric properties and presence of crater rays on Ida (larger scale).
Surface age of primary vs. secondary	Insufficient data. O. S. Barnouin et al. (2024) estimate that Dimorphos is from 60 to 130 times younger than Didymos. We conclude that the ages of Dinkinesh and Selam are indistinguishable. J. Veverka et al. (1996) conclude that the ages of Ida and Dactyl are indistinguishable, though with only nine craters observed on Dactyl, the comparison is not rigorous. With only three binary systems, we cannot reach a conclusion.

Note. The comparison column includes the following options: "NEA vs. MBA" suggests differences between the two dynamical populations; "S vs. C" suggests differences between the two spectral classes; "size" suggests differences as a function of scale; "consistent" means that there are no trends between the categories; "insufficient data" means that we cannot make a comparison because there are an insufficient number of cases to compare.

encountered by spacecraft suffers from small number statistics; not including contact binaries (e.g., perhaps Itokawa; A. J. Meyer & D. J. Scheeres 2024), spacecraft have observed only three systems so far (Ida–Dactyl, Didymos–Dimorphos, Dinkinesh–Selam). At a minimum, the Dinkinesh–Selam system highlights the numerous pathways that can emerge from a small number of interacting processes. Table 9 is a summary comparison of some physical parameters on asteroids observed by spacecraft (Table 1). One parameter that appears consistent, at least for a typical value, is crater depth-to-diameter ratio. Other parameters may show trends as a function of asteroid size, spectral class, or dynamical location.

8. Conclusions

The Lucy flyby of the Dinkinesh–Selam system enabled evaluation of major surface features, the crater and boulder distributions, and evaluation of a YORP-driven failure. We summarize our results as follows:

Impact craters. We found 29 total craters; to be included in this dataset, at least one researcher classified the feature as having an intermediate confidence that it is an impact crater (Figure 4). Nine of these craters were identified with high confidence by two researchers. The slope of the total population is shallow, with a cumulative power-law exponent of $c = 1.09 \pm 0.05$ and a differential power-law exponent of $b = 1.66 \pm 0.39$ (Figure 5). Limiting the fit to only the nine features with high confidence (category 1), the cumulative exponent is $c = 1.60 \pm 0.17$. (There are too few craters to derive a differential fit for category 1 craters.) For the most likely surface strength of <10 Pa the crater-based surface age is $\sim$1 Ma. M. Arakawa et al. (2020) find that Ryugu is 8.9 ± 2.5 Ma, E. B. Bierhaus et al. (2022) derive 1.6–2.2 Ma for the youngest craters on Bennu, O. S. Barnouin et al. (2024) estimate $\sim$12.5 Ma for Didymos, and E. Tatsumi & S. Sugita (2018) estimate a 3–33 Ma surface age for Itokawa. In all cases, the surfaces are young on geologic timescales.

The depth-to-diameter measurements for three craters are 0.08 ± 0.02, 0.09 ± 0.02, and 0.1 ± 0.01 for crater diameters $\sim$67, 82, and 134 m (Figure 7), respectively. These values are consistent with d/D values on other asteroids. We identified only three craters on Selam; small number statistics prevent accurate assessment of an SFD, though the crater spatial density is broadly consistent with that of Dinkinesh.

Boulders. In contrast to the craters, the boulders on Dinkinesh have a steep SFD, with a cumulative power-law exponent of $c = 3.93 \pm 0.03$ and a differential power-law exponent of $b = 5.02 \pm 0.33$ (Figure 8). Comparison of Dinkinesh with the other small (less than a few kilometers) asteroids visited by spacecraft suggests a trend of steeper boulder SFD on S-class asteroids relative to C-complex asteroids.

Shape and geology. Two major features, Sumak Fossa (Figures 9 and 10) and Fab Dorsum (Figures 12–14), are likely related to YORP-driven failure. The geometry and morphology of Sumak are consistent with model results for asteroids with a surface that is weaker than the interior. Fab Dorsum (the equatorial ridge) shows greater variation than Bennu in the location of the geopotential minimum; however, the geopotential slopes of Fab at length scales of tens of meters are all less than the typical 30°–40° angle of repose for granular material, indicating that the feature is stable at these length scales. The volume of Fab Dorsum is between 2 and 3.5 times that of Selam. Bella Dorsum (Figures 15 and 16), to our knowledge, is the first approximately oval-shaped ridge seen on an asteroid. Though we cannot derive Bella's origin, the roughly symmetrical shape centered on the equator suggests that it is related to a spin-driven process: perhaps a fossil interface with an object that previously rendered Dinkinesh a contact binary, or an infilled cavity from mass loss. Mass wasting and troughs that are superimposed over other features provide evidence for recent, and probably ongoing, surface evolution from rotational stress. Both lobes of Selam show evidence for structural features that span most of the lobe dimensions.

YORP. The geometry and morphology of Sumak Fossa are consistent with YORP-driven failure. Modeling the distribution of stresses for different rotation rates and two different body dimensions provides constraints on the interior strength and thus a lower limit on the spin rate of failure. Sumak Fossa spans from mid-latitudes in the northern hemisphere to high latitudes in the southern hemisphere. This geometry is more consistent with failure originating at a radial distance—in the plane of the equator—that is roughly midway between the surface and body center, which then extends to the corresponding latitudinal bounds of Sumak (Figure 20). YORP-driven stresses that approximate this geometry occur at spin rates near the 3.2 hr spin limit, but not at faster rates. The timescale to spin up an asteroid like Dinkinesh to YORP failure is 10–20 Myr. The presence of mass wasting and young troughs indicates that stress accumulation and release continue on Dinkinesh to the present day.

Binary system synthesis. A self-consistent structure for Dinkinesh that complies with the global shape, feature morphologies, plausible crater-based ages, and estimated YORP spin-up timescale is a rubble-pile object with a nearly strengthless surface and an interior that is less than tens of Pa. The Fab Dorsum morphology, especially its contacts with Sumak Fossa, suggests that it is a depositional feature, which implies that it formed by accretion of a disk versus the accumulation of mass movement that was always constrained to the surface of Dinkinesh. This motivates a YORP-driven mass-shedding origin for Fab Dorsum. The presence of a debris disk to form Fab Dorsum opens the possibility that Selam also formed from the debris disk, though that is not the only possible origin. If Selam formed from the debris disk, then Selam is also a rubble pile.

The dominant processes acting on the system, since Dinkinesh first emerged from the debris of the catastrophic disruption of a larger body, have been impact cratering and the combined solar radiation processes of YORP and Yarkovsky. Impacts are a random process, meaning that each asteroid will have its own specific history of cratering events depositing varying amounts of energy at different locations, over different time intervals. Though an asteroid's collisional lifetime—i.e., the average time until an impact catastrophically disrupts the body—is a key metric, there can be only one catastrophic impact. Prior to that event, there are an increasing number of subcatastrophic events as impact energy decreases. While YORP and Yarkovsky are steady state in the sense that asteroids always are exposed to the Sun, details affect how these processes evolve an asteroid. Internal heterogeneity is specific to each asteroid, which contributes to the size and location of YORP failure. Previous work (W. F. Bottke et al. 2015) has shown stochastic interplay between impacts, which can change the spin state, and YORP torques, which respond to spin and shape changes. For the latter, changes can cause the asteroid to spin up, spin down, or perhaps even change spin direction. The obliquity of the asteroid determines whether it drifts inward toward the Sun via Yarkovsky accelerations (retrograde spins) or outward away from the Sun (prograde spins). In addition to the significant effects on orbital evolution, the superposition of just these three processes evidently can combine to generate objects as distinct as Itokawa, Bennu, Ryugu, Didymos and Dimorphos, and Dinkinesh and Selam.

Our derived ∼1 Ma surface age for Dinkinesh is quite young on geologic timescales and comparable to the minimum ages estimated for Bennu (E. B. Bierhaus et al. 2022). These young ages highlight that impact cratering, YORP, satellite formation, and Yarkovsky are current, modern phenomena, driving present-day evolution of asteroids. More broadly, the ongoing, diverse evolution of these "geologically dead" objects is an example of the expanding appreciation that our solar system continues to evolve and that the superposition of just a few processes (cratering, Yarkovksy, YORP) can lead to diverse outcomes. Spacecraft exploration of our solar system illuminates the ancient and the current, providing fundamental information on the pathways to the present day and the processes that drive a dynamic future. The Dinkinesh encounter demonstrates the scientific capability of the Lucy mission and provides important technical experience to support successful encounters with the Jupiter Trojans, starting in 2027.

Acknowledgments

We thank the entire Lucy team for making the Dinkinesh encounter possible. The Lucy data are publicly available via NASA's Planetary Data System Small Bodies Node. The Lucy mission is funded through the NASA Discovery program via contract Nos. NNM16AA08C and NNG17FD73C.

ORCID iDs

E. B. Bierhaus https://orcid.org/0000-0001-5890-9821
S. Marchi https://orcid.org/0000-0003-2548-3291
S. J. Robbins https://orcid.org/0000-0002-8585-2549
S. Mottola https://orcid.org/0000-0002-0457-3872
W. F. Bottke https://orcid.org/0000-0002-1804-7814
K. Noll https://orcid.org/0000-0002-6013-9384
J. F. Bell III https://orcid.org/0000-0002-2006-4074
J. M. Sunshine https://orcid.org/0000-0002-9413-8785
J. Spencer https://orcid.org/0000-0003-4452-8109
F. Preusker https://orcid.org/0000-0001-9005-4202
C. Howett https://orcid.org/0000-0003-1869-4947
M. Hirabayshi https://orcid.org/0000-0002-1821-5689

References

Arakawa, M., Saiki, T., Wada, K., et al. 2020, An Artificial Impact on the Asteroid (162173) Ryugu Formed a Crater in the Gravity-Dominated Regime, Sci, 368, 67
Agrusa, H. F., Zhang, Y., Richardson, D. C., et al. 2024, Direct N-body Simulations of Satellite Formation around Small Asteroids: Insights from DART's Encounter with the Didymos System., PSJ, 5, 54
Ballouz, R. L., Ernst, C. M., Barnouin, O. S., et al. 2025, Seismic Resurfacing of 433 Eros Indicative of Highly Dissipative Interior for Large Near-Earth Asteroids, NatAs, 9, 347
Ballouz, R. L., Walsh, K. J., Barnouin, O. S., et al. 2020, Bennu's Near-Earth Lifetime of 1.75 Million Years Inferred from Craters on Its Boulders, Natur, 587, 205
Barnouin, O. S., Daly, M. G., Palmer, E. E., et al. 2019, Shape of (101955) Bennu Indicative of a Rubble Pile with Internal Stiffness, NatGe, 12, 247
Barnouin, O. S., Ballouz, R.-L., Marchi, S., et al. 2024, The Geology and Evolution of the Near-Earth Binary Asteroid System (65803) Didymos, NatCo, 15, 6202
Belton, M. J. S., Veverka, J., Thomas, P., et al. 1992, Galileo Encounter with 951 Gaspra: First Pictures of An Asteroid, Sci, 257, 1647
Belton, M. J. S., Chapman, C. R., Klaasen, K. P., et al. 1996, Galileo's Encounter with 243 Gaspra: An Overview of the Imaging Experiment, Icar, 120, 1

Bierhaus, E. B., Trang, D., Daly, R. T., et al. 2022, Crater Population on Asteroid (101955) Bennu Indicates Impact Armouring and a Young Surface, NatGe, 15, 440
Bierhaus, E. B., Rossmann, F., Johnson, C., et al. 2023, A Subsurface Layer on Asteroid (101955) Bennu and Implications for Rubble Pile Asteroid Evolution, Icar, 406, 115736
Bolin, B. T., Noll, K. S., Caiazzo, I., Fremling, C., & Binzel, R. P. 2023, Keck and Gemini Spectral Characterization of Lucy Mission Fly-By Target (152830) Dinkinesh, Icar, 400, 115562
Bottke, W. F., Broz, M., O'Brien, D. P., et al. 2015, The Collisional Evolution of the Asteroid Belt, in Asteroids IV, ed. P. Michel, F. DeMeo, & W. F. Bottke (Univ. Arizona Press), 701
Bottke, W. F., Moorehead, A., Connolly, H. C., et al. 2020, Meteoroid Impacts as a Source of Bennu's Particle Ejection Events, JGRE, 125, e2019JE006282
Bottke, W. F., Nolan, M. C., Greenberg, R., & Kolvoord, R. A. 1994, Velocity Distributions among Colliding Asteroids, Icar, 107, 255
Bottke, W., Vokrouhlický, D., Marschall, R., et al. 2023, The Collisional Evolution of the Primordial Kuiper Belt, Its Destabilized Population, and the Trojan Asteroids, PSJ, 4, 42
Bottke, W. F., Vokrouhlický, D., Rubincam, D. P., & Nesvorný, D. 2006, The Yarkovsky and Yorp Effects: Implications for Asteroid Dynamics, AREPS, 34, 157
Bottke, W. F., Vokrouhlický, D., Walsh, K. J., et al. 2015, In Search of the Source of Asteroid (101955) Bennu: Applications of the Stochastic YORP Model, Icar, 247, 191
Bottke, W., Meyer, A., Vokrouhlický, D., et al. 2025, Surface Ages for the Sample Return Asteroids Bennu, Ryugu, and Itokawa, PSJ, 6, 33
Buczkowski, D. L., Barnouin-Jha, O. S., & Prockter, L. M. 2008, 433 Eros Lineaments: Global Mapping and Analysis, Icar, 193, 39
Burke, K. N., DellaGiustina, D. N., Bennet, C. A., et al. 2021, Particle Size-Frequency Distributions of the OSIRIS-REx Candidate Sample Sites on Asteroid (101955) Bennu, RemS, 13, 1315
Čapek, D., & Vokrouhlický, D. 2004, The YORP Effect with Finite Thermal Conductivity, Icar, 172, 526
Chapman, C. R., & Haefner, R. R. 1967, A Critique of Methods for Analysis of the Diameter-Frequency Relation for Craters with Special Application to the Moon, JGR, 72, 549
Daly, M. G., Barnouin, O. S., Seabrook, J. A., et al. 2020, Hemispherical Differences in the Shape and Topography of Asteroid (101955) Bennu, SciA, 6, eabd3649
Daly, R. T., Bierhaus, E. B., Barnouin, O. S., et al. 2020, The Morphometry of Impact Craters on Bennu, GeoRL, 47, e2020GL089672
Daly, R. T., Barnoui, O. S., Bierhaus, E. B., et al. 2022, The Morphometry of Small Impact Craters on Bennu: Relationships to Geologic Units, Boulders, and Impact Armoring, Icar, 384, 115058
Daly, R. T., Ernst, C. M., Barnouin, O. S., et al. 2023, Successful Kinetic Impact into an Asteroid for Planetary Defence, Natur, 616, 443
Davis, A. B., & Scheeres, D. J. 2020, High-fidelity Modeling of Rotationally Fissioned Asteroids, PSJ, 1, 17
Davis, D. R., & Farinella, P. 1997, Collisional Evolution of Edgeworth-Kuiper Belt Objects, Icar, 125, 50
DeSouza, I., Daly, M. G., Barnouin, O. S., Ernst, C. M., & Bierhaus, E. B. 2015, Improved Techniques for Size-Frequency Distribution Analysis in the Planetary Sciences: Application to Blocks on 25143 Itokawa, Icar, 247, 77
Dombard, A. J., Barnouin, O. S., Prockter, L. M., & Thomas, P. C. 2010, Boulders and Ponds on the Asteroid 433 Eros, Icar, 210, 713
Ďurech, J., & Hanuš, J. 2023, Reconstruction of Asteroid Spin States from Gaia DR3 Photometry, A&A, 675, A24
Duxbury, T. C., Newburn, R. L., Acton, C. H., et al. 2004, Asteroid 5535 Annefrank Size, Shape, and Orientation: Stardust First Results, JGRE, 109, E02002
Elekes, F., & Parteli, E. J. R. 2021, An Expression for the Angle of Repose of Dry Cohesive Granular Materials on Earth and in Planetary Environments, PNAS, 118, 38
Ernst, C. M., Barnouin, O. S., Daly, R. T. & the Small Body Mapping Tool Team 2018, The Small Body Mapping Tool (SBMT) for Accessing, Visualizing, and Analyzing Spacecraft Data in Three Dimensions, LPSC, 49, 1043
Fujiwara, A., Kawaguchi, J., Yeomans, D. K., et al. 2006, The Rubble-Pile Asteroid Itokawa as Observed by Hayabusa, Sci, 312, 1330
Good, P. G., Faiks, P., & Pisano, W. J. 2022, Terminal Tracking for the Lucy Trojan Asteroid Mission, in 44th Annual AAS Guidance, Navigation, and Control Conf., AAS 22-131
Hirabayashi, M. 2015, Failure Modes and Conditions of a Cohesive, Spherical Body Due to YORP Spin-Up, MNRAS, 454, 2249
Hirabayashi, M., Tatsumi, E., Miyamoto, H., et al. 2019, The Western Bulge of 162173 Ryugu Formed as a Result of a Rotationally Driven Deformation Process, ApJL, 874, L10
Hirabayashi, M., Nakano, R., Tatsumi, E., et al. 2020, Spin-Driven Evolution of Asteroids' Top-Shapes at Fast and Slow Spins Seen from (101955) Bennu and (162173) Ryugu, Icar, 352, 113946
Hirabayashi, M., Sánchez, D. P., & Scheeres, D. J. 2015, Internal Structure of Asteroids Having Surface Shedding due to Rotational Instability, ApJ, 808, 12
Hirabayashi, M., & Scheeres, D. J. 2015, Stress and Failure Analysis of Rapidly Rotating Asteroid (29075) 1950 DA, ApJL, 798, L8
Hirata, N., Barnouin-Jha, O., Honda, C., et al. 2009, A Survey of Possible Impact Structures on 25143 Itokawa, Icarus, 200, 486
Hirata, N., Morota, T., Yuichiro, C., et al. 2020, The Spatial Distribution of Impact Craters on Ryugu, Icar, 338, 113527
Holsapple, K. A. 2001, Equilibrium Configurations of Solid Cohesionless Bodies, Icar, 154, 432
Holsapple, K. A. 2004, Equilibrium Figures of Spinning Bodies with Self-Gravity, Icar, 172, 272
Holsapple, K. A. 2010, On YORP-Induced Spin Deformations of Asteroids, Icar, 205, 430
Holsapple, K. A., & Housen, K. R. 2007, A Crater and Its Ejecta: An Interpretation of Deep Impact, Icar, 187, 345
Huang, J., Ji, J., Ye, P., et al. 2013, The Ginger-Shaped Asteroid 4179 Toutatis: New Observations from a Successful Flyby of Chang'e-2, NatSR, 3, 3411
Hudson, R. S., Ostro, S., & Scheeres, D. J. 2003, High-Resolution Model of Asteroid 4179 Toutatis, Icar, 161, 346
Hyodo, R., & Sugiura, K. 2022, Formation of Moons and Equatorial Ridge around Top-Shaped Asteroids after Surface Landslide, ApJL, 937, L36
Jacobson, S. A., & Scheeres, D. J. 2011, Dynamics of Rotationally Fissioned Asteroids: Source of Observed Small Asteroid Systems, Icar, 214, 161
Jawin, E. R., Walsh, K. J., Barnouin, O. S., et al. 2020, Global Patterns of Recent Mass Movement on Asteroid (1011955) Bennu, JGRE, 125, E06475
Jiang, Y., Ji, J., Huang, J., et al. 2015, Boulders on Asteroid Toutatis as Observed by Chang'e-2, NatSR, 5, 16029
Jorda, L., Lamy, P. L., Gaskell, R. W., et al. 2012, Asteroid (2867) Steins: Shape, Topography and Global Physical Properties from OSIRIS Observations, Icar, 221, 1089
Levison, H., Olkin, C. B., Noll, K. S., et al. 2021, Lucy Mission to the Trojan Asteroids: Science Goals, PSJ, 2, 171
Levison, H. F., Marchi, S., Noll, K. S., et al. 2024, A Contact Binary Satellite of the Asteroid (152830) Dinkinesh, Natur, 629, 1015
Marchi, S., Chapman, C. R., Barnouin, O. S., Richardson, J. E., & Vincent, J.-B. 2015, Cratering on Asteroids, in Asteroids IV, ed. P. Michel, F. E. DeMeo, & W. F. Bottke (Univ. of Arizona Press), 725
Marchi, S., Mottola, S., Cremonese, G., Massironi, M., & Martellato, E. 2009, A New Chronology for the Moon and Mercury, AJ, 137, 4936
Margot, J.-L., Pravec, P., Taylor, P., Carry, B., & Jacobson, S. 2015, Asteroid Systems: Binaries, Triples, and Pairs, in Asteroids IV, ed. P. Michel, F. E. DeMeo, & W. F. Bottke (Univ. Arizona Press), 895
Mazrouei, S., Daly, M. G., Barnouin, O. S., Ernst, C. M., & DeSouza, I. 2014, Block Distributions on Itokawa, Icar, 229, 181
Meyer, A. J., & Scheeres, D. J. 2024, The Strength and Shapes of Contact Binary Objects, ApJL, 963, 9
Michel, P., O'Brien, D. P., Abe, S., & Hirata, N. 2009, Itokawa's Cratering Record as Observed by Hayabusa: Implications for Its Age and Collisional History, Icar, 200, 503
Michikami, T., Honda, C., Miyamoto, H., et al. 2019, Boulder Size and Shape Distributions on Asteroid Ryugu, Icar, 331, 179
Michikami, T., & Hagermann, A. 2021, Boulder Sizes and Shapes on Asteroids: A Comparative Study of Eros, Itokawa and Ryugu, Icar, 357, 114282
Michikami, T., Nakamura, A. M., Hirata, N., et al. 2008, Size-Frequency Statistics of Boulders on Global Surface of Asteroid 25143 Itokawa, EP&S, 60, 13
Miyamoto, H., Yano, H., Scheeres, D. J., et al. 2007, Regolith Migration and Sorting on Asteroid Itokawa, Sci, 316, 1011
Mottola, S., Preusker, F., Weaver, H. A., et al. 2024, Photometric Properties of (152830) Dinkinesh from Disk-Resolved Imaging, LPSC, 56, 2119
Naidu, S. P., Benner, L. A. M., Brozovic, M., et al. 2020, Radar Observations and a Physical Model of Binary Near-Earth Asteroid 65803 Didymos, Target of the DART Mission, Icar, 348, 113777
Nakano, R., & Hirabayashi, M. 2020, Mass-Shedding Activities of Asteroid (3200) Phaethon Enhanced by Its Rotation, ApJL, 892, L22

Nesvorný, D., Brož, M., & Carruba, V. 2015, Identification and Dynamical Properties of Asteroid Families, in Asteroids IV, ed. P. Michel, F. E. DeMeo, & W. F. Bottke (Univ. of Arizona Press), 895
Nesvorný, D., Vokrouhlický, D., Bottke, W. F., & Levison, H. F. 2018, Evidence for Very Early Migration of the Solar System Planets from the Patroclus-Menoetius Binary Jupiter Trojan, NatAs, 2, 878
Ni, B., Elishakoff, I., Jiang, C., et al. 2016, Generalization of the Super Ellipsoid Concept and Its Application in Mechanics, Appl. Math. Model., 40, 9427
Nishiyama, G., Kawamura, T., Namiki, N., et al. 2021, Simulation of Seismic Wave Propagation on Asteroid Ryugu Induced by the Impact Experiment of the Hayabusa2 Mission: Limited Mass Transport by Low Yield Strength of Porous Regolith, JGRE, 126, e06594
Olkin, C., Vincent, M., Adam, C., et al. 2024, Mission Design and Concept of Operations for the Lucy Mission, SSRv, 220, 47
Pajola, M., Tusberti, F., Lucchetti, A., et al. 2024, Evidence for Multi-fragmentation and Mass Shedding of Boulders on Rubble-Pile Binary Asteroid System (65803) Didymos, NatCo, 15, 6205
Pike, R. J. 1980, Control of Crater Morphology by Gravity and Target Type: Mars, Earth, Moon, LPSC, 11, 2159
Pravec, P., & Harris, A. W. 2000, Fast and Slow Rotation of Asteroids, Icar, 148, 12
Preusker, F., Mottola, S., Matz, K.-D., et al. 2024, Shape Model of Asteroid (152830) Dinkinesh from LUCY Imagery, in Europlanet Science Congress 2024, Berlin, Germany, EPSC2024–963
Prockter, L. M., Thomas, P., Robinson, M., et al. 2002, Surface Expressions of Structural Features on Eros, Icar, 155, 75
Richardson, J., Steckloff, J. A., & Minton, D. A. 2020, Impact-Produced Seismic Shaking and Regolith Growth on Asteroids 433 Eros, 2867 Šteins, and 25143 Itokawa, Icar, 347, 113811
Robbins, S. J., Antonenko, I., Kirchoff, M. R., et al. 2014, The Variability of Crater Identification among Expert and Community Crater Analysts, Icar, 234, 109
Robbins, S. J., Bierhaus, E. B., Barnouin, O., et al. 2023, Imaging Lunar Craters with the Lucy Long Range Reconnaissance Imager (L'LORRI): A Resolution Test for NASA's Lucy Mission, PSJ, 4, 234
Robbins, S. J., Kirchoff, M. R., & Ostrach, L. R. 2025, Crater Detection Dependence on Resolution, Incidence Angle, Emission Angle, and Phase Angle, GeoRL, 52, EPSC–DPS2025-855
Robin, C. Q., Duchene, A., Murdoch, N., et al. 2024, Mechanical Properties of Rubble Pile Asteroids (Dinorphos, Itokawa, Ryugu, and Bennu) through Surface Boulder Morphological Analysis), NatCo, 15, 6203
Robinson, M. S., Thomas, P. C., Veverka, J., Murchie, S. L., & Wilcox, B. B. 2002, The Geology of 433 Eros, M&PS, 37, 1651
Rubincam, D. P. 2000, Radiative Spin-Up and Spin-Down of Small Asteroids, Icar, 148, 2
Sánchez, P., & Scheeres, D. J. 2014, The Strength of Regolith and Rubble Pile Asteroids, M&PS, 49, 788
Sánchez, P., & Scheeres, D. J. 2016, Disruption Patterns of Rotating Self-Gravitating Aggregates: A Survey on Angle of Friction and Tensile Strength, Icar, 271, 453
Sánchez, P., & Scheeres, D. J. 2017, Rotational Evolution of Self-Gravitating Aggregates with Cores of Variable Strength, P&SS, 157, 39
Scheeres, D. J. 2007, The Dynamical Evolution of Uniformly Rotating Asteroids Subject to YORP, Icar, 188, 430
Scheeres, D. J. 2015, Landslides and Mass Shedding on Spinning Spherical Asteroids, Icar, 247, 1
Scheeres, D. J., Hartzell, C. M., Sánchez, P., & Swift, M. 2010, Scaling Forces to Asteroid Surfaces: The Role of Cohesion, Icar, 210, 968
Scheeres, D. J., Hesar, S. G., Tardivel, S., et al. 2016, The Geophysical Environment of Bennu, Icar, 276, 116
Shepard, M. K. 2017, Introduction to Planetary Photometry (Cambridge Univ. Press.), 258
Sierks, H., Lamy, P., Barbieri, C., et al. 2011, Images of Asteroid 21 Lutetia: A Remnant Planetesimal from the Early Solar System, Sci, 334, 487
Spencer, J. R., Bell III, J. F., Christensen, P. R., et al. 2024, The First Earth Flyby (EGA1), SSRv, 220, 3
Statler, T. S. 2009, Extreme Sensitivity of the YORP Effect to Small-Scale Topography, Icar, 202, 502
Tardivel, S., Sánchez, P., & Scheeres, D. J. 2018, Equatorial Cavities on Asteroids, an Evidence of Fission Events, Icar, 304, 192
Tatsumi, E., & Sugita, S. 2018, Cratering Efficiency on Coarse-Grained Targets: Implications for the Dynamical Evolution of Asteroid 25143 Itokawa, Icar, 300, 227
Veverka, J., Robinson, M., Thomas, P., et al. 2000, NEAR at Eros: Imaging and Spectral Results, Sci, 289, 2088
Veverka, J., Thomas, P., Harch, A,, et al. 1999, NEAR Encounter with Asteroid 253 Mathilde: Overview, Icar, 140, 3
Veverka, J., Thomas, P. C., Helfenstein, P., et al. 1996, Dactyl: Galileo Observations of Ida's Satellite, Icar, 120, 200
Vokrouhlický, D., Bottke, W. F., Chesley, S. R., Scheeres, D. J., & Statler, T. S. 2015, The Yarkovsky and YORP Effects, in Asteroids IV, ed. P. Michel, F. E. DeMeo, & W. F. Bottke (Univ. of Arizona Press), 509
Vokrouhlický, D., Bottke, W. F., & Nesvornýf, D. 2017, Forming the Flora Family: Implications for the Near-Earth Asteroid Population and Large Terrestrial Planet Impactors, AJ, 153, 172
Walsh, K. J., Ballouz, R.-L., Bottke, W. F., et al. 2024, Numerical Simulations Suggest Asteroids (101955) Bennu and (162173) Ryugu Are Likely Second or Later Generation Rubble Piles, NatCo, 15, 5653
Walsh, K. J. 2018, Rubble Pile Asteroids, ARA&A, 56, 593
Walsh, K. J., & Jacobson, S. A. 2015, Formation and Evolution of Binary Asteroids, in Asteroids IV, ed. P. Michel, F. E. DeMeo, & W. F. Bottke (Univ. Arizona Press), 895
Walsh, K. J., Richardson, D. C., & Michel, P. 2008, Rotational Breakup as the Origin of Small Binary Asteroids, Natur, 454, 188
Watanabe, S., Hirabayashi, M., Hirata, N., et al. 2019, Hayabusa2 Arrives at the Carbonaceous Asteroid 162173 Ryugu—a Spinning Top–Shaped Rubble Pile, Sci, 364, 268
Weaver, H. A., Wilson, J. P., Conard, S. J., et al. 2023, The Lucy Long Range Reconnaissance Imager (L'LORRI), SSRv, 219, 82
Yuichi, T., Takanao, S., Terui, F., et al. 2020, Hayabusa2 Mission Status: Landing, Roving and Cratering on Asteroid Ryugu, AcAau, 171, 42
Zhang, Y., Michel, P., Barnouin, O. S., et al. 2022, Inferring Interiors and Structural History of Top-Shaped Asteroids from External Properties of Asteroid (101955) Bennu, NatCo, 13, 4589